CERN/LHCC 2002-029
LHCb TDR 8
8 November 2002

TDR

LHCb Inner Tracker

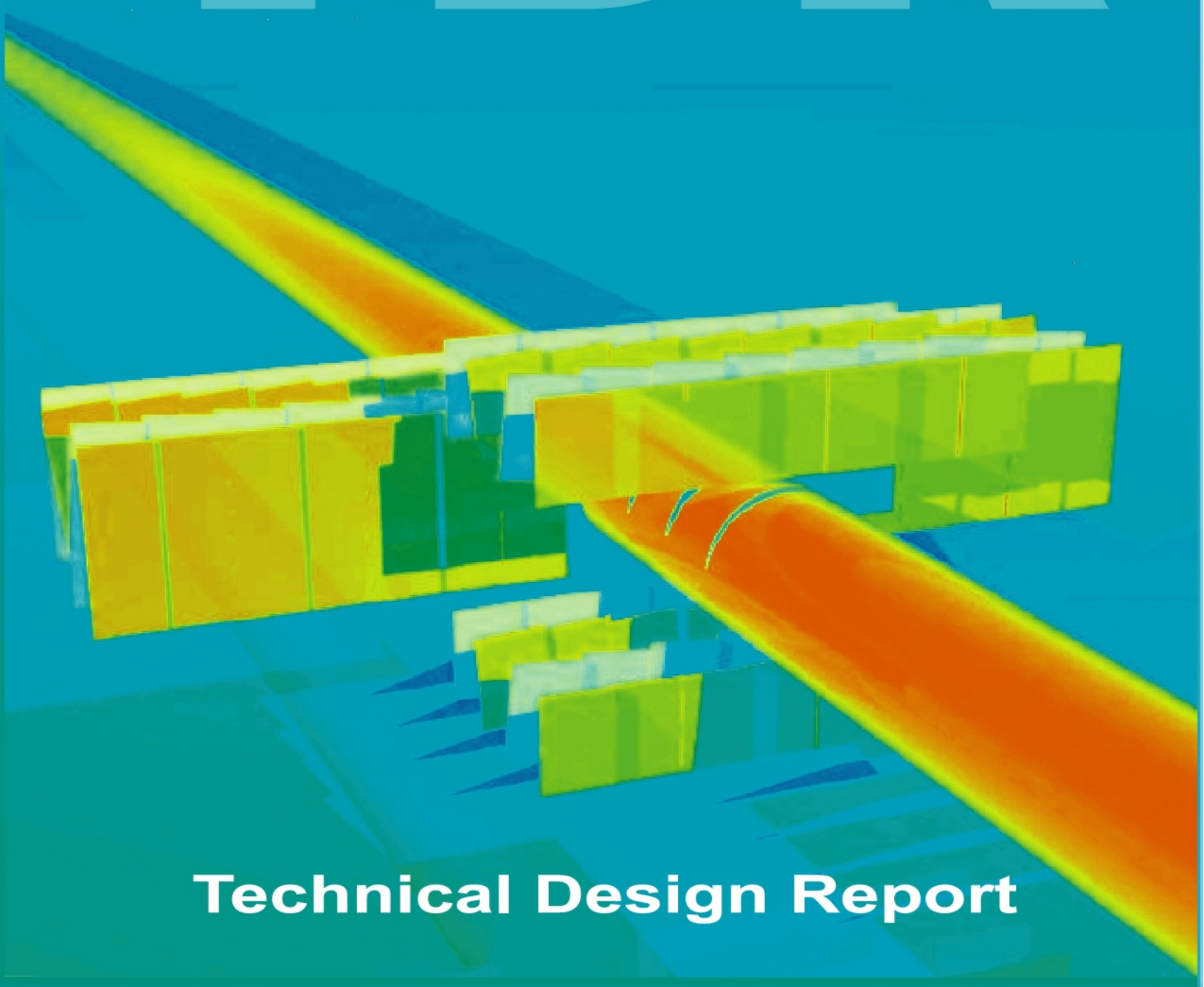

Technical Design Report

CERN/LHCC 2002-029
LHCb TDR 008
November 8, 2002

LHCb

Inner Tracker Technical Design Report

Printed at CERN
Geneva, 2002
ISBN 92-9083-201-X

The LHCb Collaboration[1]

Brasilian Center for Research in Physics, CBPF, Rio de Janeiro, Brasil
A.Franca Barbosa, I.Bediaga, G.Cernicchiaro, E.Correa de Oliveira, J.Magnin, J.Marques de Miranda, A.Massafferri, E.Polycarpo, A.Reis

University of Rio de Janeiro, UFRJ, Rio de Janeiro, Brasil
S.Amato, T.da Silva, J.R.T.de Mello Neto, B. de Paula, L.de Paula, M.Gandelman, J.H.Lopes, B.Marechal, D.Moraes, N. Pelloux, C. Perreira Nunes

LAPP Annecy, Annecy-Le-Vieux, France
D.Boget, I.de Bonis, D.Decamp, N.Dumont Dayot, M.-N.Minard, B.Pietrzyk, H. Terrier

University of Clermont-Ferrand II, Clermont-Ferrand, France
Z.Ajaltouni, G.Bohner, V.Breton, C.Carloganu, R.Cornat, O.Deschamps, P.Henrard, J.Lecoq, R. Lefevre, S.Monteil, P.Perret, C.Rimbault

CPPM Marseille, Aix University-Marseille II, Marseille, France
E.Aslanides, J.P.Cachemiche, F.Derue, B.Dinkespiler, P.Y.Duval, R.Le Gac, O.Leroy, P.L.Liotard, M.Menouni, A.Tsaregorodtsev, B.Viaud

University of Paris-Sud, LAL Orsay, Orsay, France
G.Barrand, C.Beigbeder-Beau, R.Beneyton, D.Breton, O.Callot, D.Charlet, B.D'Almagne, B.Delcourt, F.Fulda Quenzer, B.Jean-Marie, J.Lefrançois, F.Machefert, M.-H.Schune, V.Tocut, K.Truong

Technical University of Dresden, Dresden, Germany
R.Schwierz, B.Spaan

Max-Planck-Institute for Nuclear Physics, Heidelberg, Germany
M. Agari, C.Bauer, D.Baumeister, N.Bulian, H.P.Fuchs, T.Glebe[1)], W.Hofmann, K.T.Knöpfle, S.Löchner, A.Ludwig, F.Sanchez Nieto[2)], M.Schmelling, B.Schwingenheuer

Physics Institute, University of Heidelberg, Heidelberg, Germany
S.Bachmann, P.Bock, H.Deppe, F.Eisele, S.Henneberger, P.Igo-Kemenes(1), R.Rusnyak, U.Stange, U.Trunk, M.Walter, D.Wiedner, U.Uwer
(1) also at CERN

Kirchhoff Institute for Physics, University of Heidelberg, Heidelberg, Germany
I. Kisel, V.Lindenstruth, M.W.Schulz, F.Vinci dos Santos, A.Walsch

Laboratori Nazionali dell' INFN, Frascati, Italy
G.Bencivenni, C.Bloise, F.Bossi, P.Campana, G.Capon, P.DeSimone, C.Forti, M.A.Franceschi, F.Murtas, L.Passalacqua, V.Patera(1), A. Sciubba(1)
(1)also at Dipartimento di Energetica, University of Rome, "La Sapienza"

[1]This list includes additional colleagues who made particular contributions to the work presented in this TDR

University of Bologna and INFN, Bologna, Italy
M.Bargiotti, A.Bertin, M.Bruschi, M.Capponi, I.D'Antone, S.de Castro, P.Faccioli, L.Fabbri, D.Galli, B.Giacobbe, I.Lax, U.Marconi, I.Massa, M.Piccinini, M.Poli, N.Semprini-Cesari, R.Spighi, V.Vagnoni, S.Vecchi, M.Villa, A.Vitale, A.Zoccoli

University of Cagliari and INFN, Cagliari, Italy
W. Bonivento, S.Cadeddu, A.Cardini, A.Lai, D.Pinci, B.Saitta

University of Ferrara and INFN, Ferrara, Italy
W.Baldini, V.Carassiti, A.Cotta Ramusino, P.Dalpiaz, A.Gianoli, M.Martini, F.Petrucci, M.Savrié

University of Florence and INFN, Florence, Italy
A.Bizzeti, G.Collazuol, E.Iacopini, M.Lenti, G.Passaleva, M.Veltri

University of Genoa and INFN, Genoa, Italy
S.Cuneo, F.Fontanelli, V.Gracco, G.Mini, P.Musico, A.Petrolini, M.Sannino

University of Milano-Bicocca and INFN, Milano, Italy
T.Bellunato(1), M.Calvi, C.Matteuzzi(1), M.Musy, P.Negri
(1) also at CERN

University of Rome, "La Sapienza" and INFN, Rome, Italy
G.Auriemma(1), V.Bocci, C.Bosio, D.Fidanza(1), A.Frenkel, G.Martellotti, S.Martinez, G.Penso, S.Petraca, G.Pirozzi, W. Rinaldi, R.Santacesaria, C.Satriano(1), A.Satta
(1) also at University of Basilicata, Potenza

University of Rome, "Tor Vergata" and INFN, Rome, Italy
G.Carboni(1), S. De Capua, D.Domenici, R.Messi, L.Pacciani, E.Santovetti
(1) also at CERN

NIKHEF, The Netherlands
G.van Apeldoorn(1,3), N.van Bakel(1,2), T.S.Bauer(1,4), J.F.J. van den Brand(1,2), H.J.Bulten(1,2), M.Doets(1), R.van der Eijk(1), D.Groep(1), V.Gromov(1), R.Hierck(1), L.Hommels(1), J. van Hunen(1), E.Jans(1), T.Ketel(1,2), S.Klous (1,2), M.Merk(1), F.Mul(2), A. Pellegrino(1), G.Raven(1,2), H.Schuijlenburg(1), T.Sluijk(1), J.van Tilburg(1), H.de Vries(1),L.Wiggers(1), E.Zupan(1)
(1) Foundation of Fundamental Research of Matter in the Netherlands,
(2) Free University Amsterdam,
(3) University of Amsterdam,
(4) University of Utrecht,

Institute of High Energy Physics, Beijing, P.R.C.
C.Gao, C.Jiang, H.Sun, Z.Zhu

Research Centre of High Energy Physics, Tsinghua University, Beijing, P.R.C.
M.Bisset, J.P.Cheng, Y.G.Cui, Y.Dai, Y.Gao, H.J.He, C.Huang, Y.P.Kuang, Q.Li, Y.J.Li, Y.Liao, J.P.Ni, B.B.Shao,J.J.Su, Y.R.Tian, Q.Wang, Q.S.Yan

Institute for Nuclear Physics and University of Mining and Metalurgy, Krakow, Poland
K. Ciba, K.Galuszka, L.Hajduk, P.Kapusta, J.Michalowski, B.Muryn, Z.Natkaniec, G.Polok, M.Stodulski, M.Witek(1)
(1) also at CERN

Soltan Institute for Nuclear Physics, Warsaw, Poland
M.Adamus, A.Chlopik, Z.Guzik, A.Nawrot, K. Syryczynski, M.Szczekowski

Horia Hulubei-National Institute for Physics and Nuclear Engineering (IFIN-HH), Bucharest-Magurele, Romania
C.Coca, G.Giolu, C.Magureanu, M. Orlandea, S.Popescu(1), T.Preda, A.M.Rosca(2), P.D.Tarta
(1) also at CERN
(2) also at Humbolt University, Berlin

Institute for Nuclear Research (INR), Moscow, Russia
S.Filippov, J.Gavrilov, E.Guschin, V.Kloubov, L.Kravchuk, S.Laptev, V.Laptev, V.Postoev, G. Rybkine, A.Sadovski, I.Semeniouk, V. Strigin

Institute of Theoretical and Experimental Physics (ITEP), Moscow, Russia
S.Barsuk, I.Belyaev (1), A.Golutvin, O.Gouchtchine, V.Kiritchenko, V.Kochetkov, I.Korolko, G.Pakhlova, E. Melnikov, A.Morozov, P.Pakhlov, D.Roussinov, V.Rusinov, S.Semenov, A.Soldatov, E.Tarkovski
(1) also at CERN

Budker Institute for Nuclear Physics (INP), Novosibirsk, Russia
K.Beloborodov, A. Berdiouguine, A.Bondar, A.Bozhenok, A.Buzulutskov, S.Eidelman, V.Golubev, P.Krokovnyi, S.Oreshkin, A.Poluektov, S.Serednyakov, L.Shekhtman, B.Shwartz, Z.Silagadze, A.Sokolov, A.Vasiljev

Institute for High Energy Physics (IHEP-Serpukhov),Protvino, Russia
L.A.Afanassieva, I.V.Ajinenko, K.Beloous, V.Brekhovskikh, S.Denissov, A.V.Dorokhov, R.I.Dzhelyadin, A.Kobelev, A.K.Konoplyannikov, A.K.Likhoded, V.D.Matveev, V.Novikov, V.F.Obraztsov, A.P.Ostankov, V.I.Rykalin, V.K.Semenov, M.M.Shapkin, N.Smirnov, A.Sokolov, M.M.Soldatov, V.V.Talanov, O.P.Yushchenko

Petersburg Nuclear Physics Institute, Gatchina, St.Petersburg, Russia
B.Botchine, V. Ganja, S.Guetz, A.Kashchuk, V.Lazarev, O, Maev, N.Saguidova, V.Souvorov(1), E.Spiridenkov, A.Vorobyov, An.Vorobyov, N. Voropaev
(1) also at CERN

University of Barcelona, Barcelona, Spain
E.Aguilo, R.Ballabriga(1), M.Calvo, S.Ferragut, Ll.Garrido, D.Gascon, R.Graciani Diaz, S.Luengo(1), D.Peralta, M.Rosello(1), X.Vilasis(1)
(1) also at departament d'Engineria Electronica La Salle, Universitat Ramon Llull, Barcelona

University of Santiago de Compostela, Santiago de Compostela, Spain
B.Adeva, P.Conde, M.V.Gallas Torreira, A.Iglesias, C.Lois Gomez, A.Pazos, M.Plo, J.M.Rodriguez, J.J.Saborido, M.J.Tobar, P.Vazquez Regueiro

University of Lausanne, Lausanne, Switzerland
P.Bartalini[3)], A.Bay, B.Carron, C.Currat[4)], O.Dormond, Y.Ermoline, L.Fernandez, R.Frei, G.Gagliardi[5)], G.Haefeli, J.P.Hertig, P.Jalocha, S.Jimenez-Otero, P.Koppenburg[6)], F.Legger, L.Locatelli, A.M.Massone[7)], J.P.Perroud, F.Ronga, O.Schneider, L.Studer, M.T.Tran, H.Voss

University of Zürich , Zürich, Switzerland
R.Bernet, K.Bösiger, F.Lehner, M.Needham, P.Sievers, S.Steiner, O.Steinkamp, U.Straumann, A.Vollhardt, D.Wyler, M.Ziegler[8)]

Institute of Physics and Technologies, Kharkiv, Ukraine
A.Dovbnya, Yu.Ranyuk

Institute for Nuclear Research, Kiev, Ukraine
V.Aushev, V.Kiva, I.Kolomiets, Yu.Pavlenko, V.Pugatch, Yu.Vasiliev

University of Bristol, Bristol, U.K.
N.H.Brook, R.D.Head, A.Phillips, A.Presland, F.F.Wilson

University of Cambridge, Cambridge, U.K.
A.Buckley, K.George, V.Gibson, K.Harrison, C.R.Jones, S.G.Katvars, C.Shepherd-Themistocleous, C.P.Ward, S.A.Wotton

Rutherford Appleton Laboratory, Chilton, U.K.
C.J.Densham, S.Easo, B.Franek, J.G.V.Guy, R.N.J.Halsall, G. Kuznetsov, J.A.Lidbury, D.Morrow, J.V.Morris, A.Papanestis, G.N.Patrick, F.J.P.Soler, S.A.Temple, M.L.Woodward

University of Edinburgh, Edinburgh, U.K.
A.Barczyk, R.Chamonal, S.Eisenhardt, A.Khan, J.Lawrence, F.Muheim, S.Playfer, A.Walker

University of Glasgow, Glasgow, U.K.
A.J.Flavell, V.O'Shea, A.MacGregor, C.Parkes, A.Pickford, F.J.P.Soler

University of Liverpool, Liverpool, U.K.
S.Biagi, T.Bowcock, G.Casse, R.Gamet, M.George, D.Hutchcroft, M.McCubbin, J.Palacios, G.Patel, I.Stavitskiy, V.Wright[9)]

Imperial College, London, U.K.
L.Allebone, G.J.Barber, D.Clark, P.Dauncey, P.Dornan, A.Duane, U.Egede, M.Girone[10)], R.Hill, S.Jolly, D.R.Price, T.Savidge, D.Websdale, R.White

University of Oxford, Oxford, U.K
M.Adinolfi, J.H.Bibby, M.J.Charles, C.Cioffi, G.Damerell, N.Harnew, F.Harris, I.A.McArthur, C.Newby, J.Rademacker, A.Soroko, N.J.Smale, S.Topp-Jorgensen, G.Wilkinson

CERN, Geneva, Switzerland
D. Altmann, G. Anelli, F.Anghinolfi, F.Bal, M.Benayoun(1), A.Braem, J.Buytaert, M.Campbell, A.Cass, M.Cattaneo, Ph.Charpentier, J.Christiansen, J.Closier, P.Collins, G.Corti, C.D'Ambrosio, H.Dijkstra, J.P.Dufey, D.Eckstein, M.Ferro-Luzzi, F.Fiedler[11)], W.Flegel, F.Formenti, R.Forty, M.Frank, C.Frei, C.Gaspar, P.Gavillet, A. Guirao Elias, T.Gys, F.Hahn, S.Haider, J.Harvey, J.A.Hernando Morata, E.van Herwijnen, H.J.Hilke, G.von Holtey, R.Jacobsson, P.Jarron, C.Joram, B.Jost, D.Lacarrère, M.Letheren, J.F.Libby[12)], C.Lippmann, R.Lindner, M.Losasso, P.Mato Vila, M.Moritz, H.Müller, T.Nakada(2), N.Neufeld, C.Padilla, U.Parzefall, W.Pokorski, S.Ponce, F.Ranjard, W.Riegler, E,M.Rodrigues Figueiredo, D.Rodriguez de Llera Gonza, S.Roiser, T.Ruf, D.Ruffinoni, T.Schietinger, S.Schmeling, B.Schmidt, T.Schneider, A.Schopper, A.Smith, W.Tejessy, F.Teubert, N.Tuning, O.Ullaland, A.Valassi, P.Vannerem, I.Videau, P.Wertelaers, W.Witzeling, K.Wyllie, Y.Xie
(1) on leave from Université de Paris VI et VII (LPNHE), Paris
(2) also at Lausanne, on leave from PSI, Villigen

[1)] now at SAP AG, Walldorf, Germany
[2)] now at Universitat Autonoma de Barcelona/IFAE, Barcelona, Spain
[3)] now at CERN, Geneva, Switzerland
[4)] now at LBNL, Berkeley, USA
[5)] now at University of Genoa and INFN, Genoa, Italy
[6)] now at KEK, Tsukuba, Japan
[7)] now at Genoa INFM, Genoa, Italy
[8)] now at University of California, Santa Cruz, USA
[9)] now at University of Glasgow, Glasgow, UK
[10)] now at CERN, Geneva, Switzerland
[11)] now at Ludwigs-Maximilians University, Munich, Germany
[12)] now at SLAC, Stanford, USA

Technical Associates
Centro Federal de Educacao Technologica (CEFET), Rio de Janeiro, Brasil
Espoo Vantaa Institute of Technology, Espoo, Finland
Ecole d' ingénieurs, Geneva, Switzerland

Acknowledgments

The LHCb Inner Tracker group would like to thank the HERA-B VDS group for their support during the test-beam activities at CERN. Their contribution of both sensors for the beam telescope and hardware and software for the data acquisition system were a key ingredient in making the detailed performance studies of the prototype silicon ladders a success.

The Zürich group would also like to thank Matt Siegler for his valuable contribution to material studies, especially to the measurement of the thermal conductivity of prototype balconies.

Contents

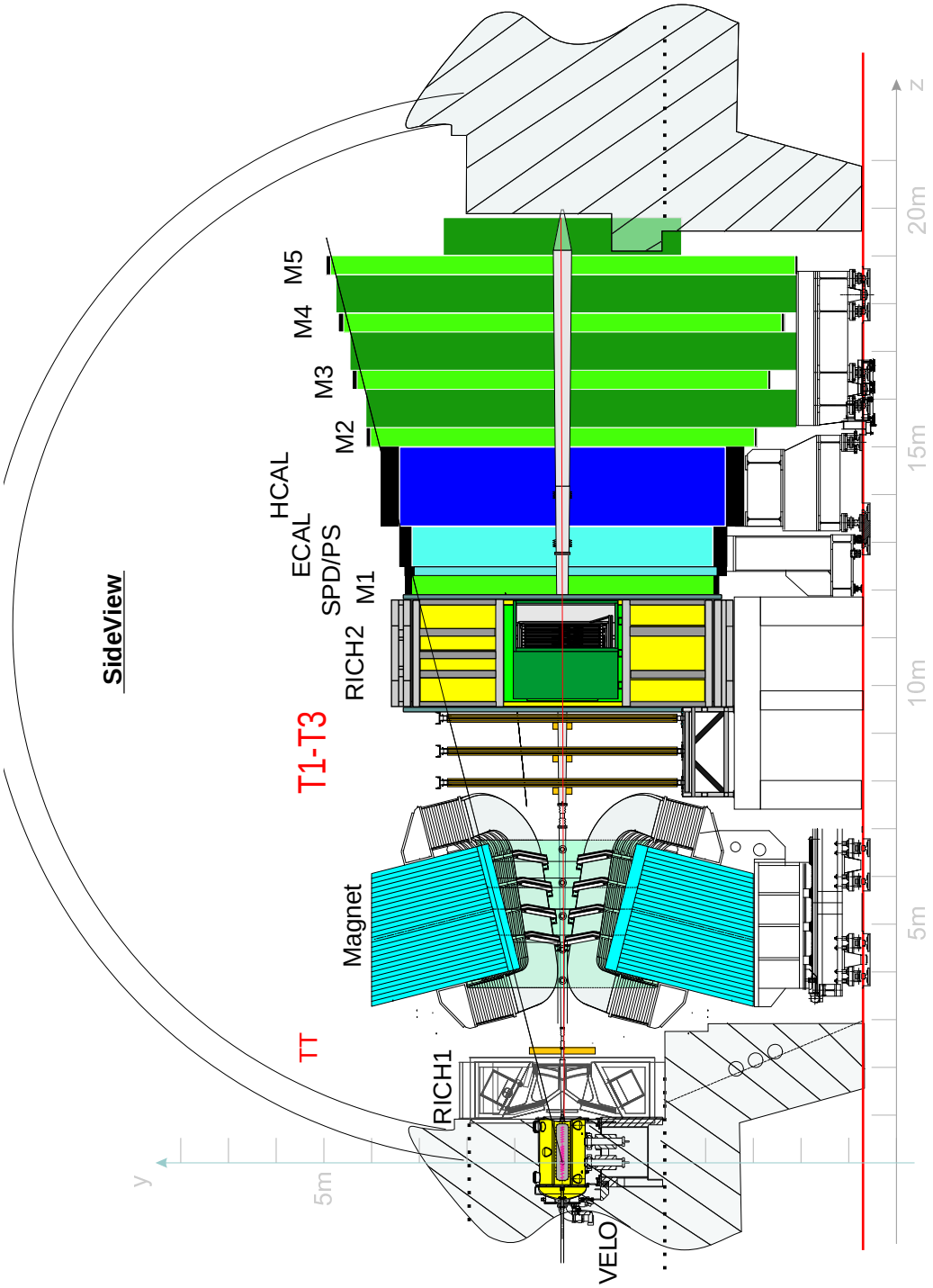

Figure 1: Sideview of the LHCb spectrometer, showing the location of the tracking stations ("TT" and "T1-T3"). The standard LHCb coordinate system is also indicated in the figure. It is a right-handed Cartesian system with the origin at the centre of the nominal pp-interaction region.

Chapter 1

Introduction

The LHCb experiment [1] is designed to exploit the large $b\overline{b}$ production cross section at the LHC in order to perform a wide range of precision studies of CP violating phenomena. The copious production of B_d, B_s and B_c mesons and b-baryons, together with the unique particle-identification capabilities of the LHCb detector, will allow the experiment to perform sensitive measurements of CP violating asymmetries in a variety of channels that are beyond the reach of the current generation of CP-violation experiments.

Since $b\overline{b}$ pairs at the LHC are predominantly produced at small angles with respect to the beam axis, the LHCb detector has been designed as a single-arm forward spectrometer. Its acceptance extends out to 300 mrad in the horizontal bending plane of the 4 Tm dipole magnet and to 250 mrad in the vertical plane. The forward acceptance of the spectrometer is limited by the LHC beam-pipe which follows a 10 mrad cone.

A side view of the LHCb detector is shown in Figure 1. The main tracking system consists of four planar tracking stations: one station ("TT") is located in between RICH1 and the magnet, three stations ("T1-T3") are located between the magnet and RICH2. Two detector technologies are employed in stations T1-T3: the outer region of these stations, away from the beam-pipe, is covered by the straw-tube drift chambers of the Outer Tracker, which has been described in an earlier TDR [2]. The innermost region around the beam-pipe, where particle densities are highest, is covered by silicon microstrip detectors — the Inner Tracker described in this document.

An isometric view of the sensitive elements of one Inner Tracker station is shown in Figure 1.1. It covers a cross-shaped area around the beam pipe, approximately 120 cm wide and 40 cm high. Each station consists of four detection layers, with two $\pm 5^\circ$ stereo views sandwiched in between two layers with vertical strips. The overall sensitive surface of the three Inner Tracker stations amounts to approximately 4.2 m^2. Large strip pitches of approximately 200 μm and read-out strips of up to 22 cm length will be employed in order to minimise the number of read-out channels.

The approximately 140 cm wide and 120 cm high TT station is entirely covered by silicon microstrip detectors. Inner Tracker and TT station together form the Silicon Tracker project, and in order to indicate the overall size of the project, a brief description of the layout of this station is given in section 1.2. However, the TT station is outside the scope of this document and will be described in a future TDR.

1.1 Detector Requirements

In order to fully exploit its exciting physics potential, the LHCb apparatus must ensure high trigger and event reconstruction efficiencies for all interesting decay channels. In the high-rate environment of the LHC, efficient and precise reconstruction of the trajectories of charged particles is a key ingredient towards achieving this aim.

Many of the interesting B meson decay channels are characterised by final states that in-

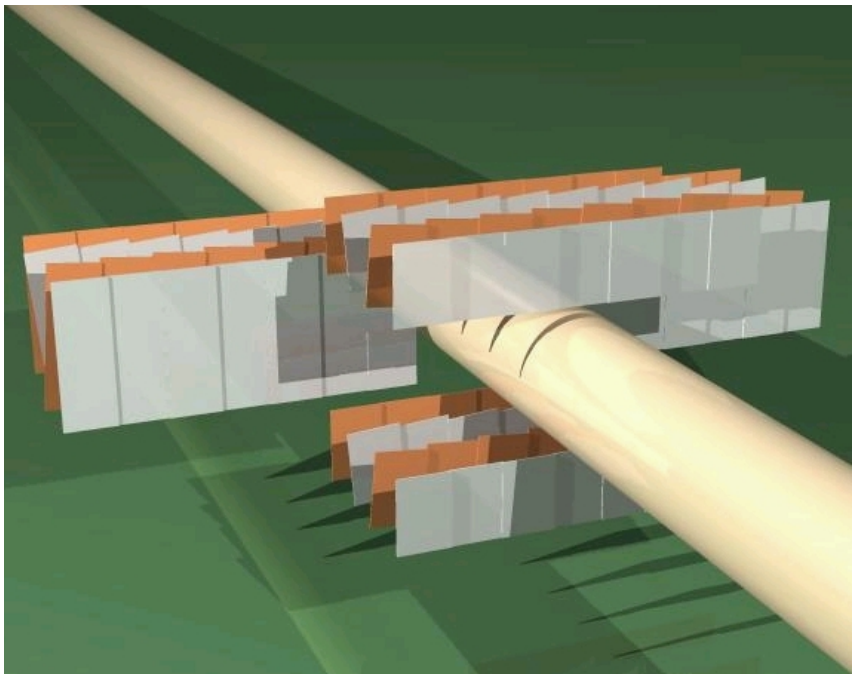

Figure 1.1: Isometric view of the sensitive elements in one station of the Inner Tracker.

volve multiple charged particles. An example is the decay $B_s^0 \to D_s^-(K^+K^-\pi^-)K^+$, which is one of the most promising channels for the determination of the angle γ of the unitarity triangle. For a measurement of the CP asymmetry, the trajectories of five particles, namely those from the B_s^0 decay plus a tagging particle from the "other" b particle, have to be reconstructed. Reconstruction efficiencies for final-state particles in excess of 90% are required in order to obtain high event reconstruction efficiencies. For example, a tracking efficiency per final state particle of 95% results in an 82% reconstruction efficiency for events that are fully contained in the LHCb acceptance.

Charged particle fluxes of up to $5 \times 10^5\,\mathrm{cm}^{-2}\mathrm{s}^{-1}$ are expected in the innermost region of the Inner Tracker. Fluxes decrease rapidly with increasing distance from the beam axis. The readout granularity of the detector has to be matched to the expected particle fluxes in order to ensure low occupancies which are required to obtain high pattern recognition efficiency. The layout and the outer dimensions of the Inner Tracker were determined by the requirement for low occupancies in the Outer Tracker.

Excellent momentum resolution is required in order to measure precisely the invariant mass of B decay candidates and separate the B meson signal from background. Again using the decay channel $B_s^0 \to D_s^- K^+$ as an example, with a momentum resolution of $\delta p/p = 0.4\%$ contributions to the invariant mass resolution of the B_s^0 meson due to momentum resolution and angular resolution at the decay vertex are roughly equal. An invariant mass resolution of approximately $10\,\mathrm{MeV}/c^2$ is expected. In LHCb, the momentum resolution is dominated by multiple scattering over a wide range of momenta and minimisation of material budget is thus an important criterion for the design of the detector. For the Inner Tracker, this poses a special challenge since parts of the front-end electronics and services that have to be close to the detector are located inside the acceptance of the experiment. On the other hand, a moderate spatial hit resolution of around $70\,\mu$m is perfectly adequate.

At the expected particle rates, radiation damage to detector and front-end electronics has to be a concern as well. The expected

particle fluences translate into a total ionizing dose of approximately 1 Mrad and a 1-MeV neutron equivalent fluence of $9 \times 10^{12}\,\mathrm{cm}^{-2}$ in the innermost region of the detector, after ten years of operation at a nominal luminosity of $\mathcal{L} = 2 \times 10^{32}\mathrm{cm}^{-2}\mathrm{s}^{-1}$. These are relatively moderate radiation levels for modern silicon detectors. Front-end electronics, however, have to be radiation qualified.

At the LHC, bunch crossings occur every 25 ns. This calls for front-end electronics with fast shaping time in order to avoid the need to reconstruct overlapping events from consecutive bunch crossings. Fast front-end electronics are, however, susceptible to significant Johnson noise if connected to large load capacitances as given by the long read-out strips employed in the Inner Tracker. Silicon sensors and front-end electronics have to be carefully designed and matched to each other in order to optimise the signal-to-noise performance and guarantee high single-hit efficiencies.

In summary, the key requirements for the design of the detector have been the need for high single layer efficiency, for fast shaping time of the front-end amplifier, a spatial resolution of better than approximately 70 μm, occupancies not exceeding a few percent, and low material budget for all components that are located inside the acceptance of the LHCb detector. Finally, of course, the design of the detector is constrained by the rather prosaic need to minimise the number of readout channels in order to keep cost as low as possible.

1.2 Evolution Since Technical Proposal

Since the time of the LHCb Technical Proposal [1], the design of the Inner Tracker has undergone a number of major revisions. These revisions were to a large extent driven by modified detector requirements as part of an overall optimisation of the LHCb detector.

1.2.1 Detector Technology

The Technical Proposal described an Inner Tracker based upon MSGC/GEM gaseous detectors, similar to those employed in the HERA-B experiment [3]. Silicon microstrip detectors and Micro Cathode Strip Chambers (MCSC) were mentioned as backup solutions.

The MSGC/GEM option was abandoned in the light of evident difficulties to reach stable and reliable operation of large systems of such detectors. The MCSC option was not pursued further. Three alternative micro-pattern gas chamber technologies — Micromegas [4], Microwire Chamber [5] and triple-GEM [6] — were subsequently suggested. Of these, triple-GEM detectors showed the most reliable performance and were for some time pursued as a candidate detector technology for the Inner Tracker.

In parallel, the option of a silicon microstrip Inner Tracker was investigated in detail. A detector concept was developed and it was demonstrated that an all-silicon detector could be built within the Inner Tracker budget. In May 2001, the decision was taken to adopt silicon microstrips as baseline technology for the full Inner Tracker.

1.2.2 Dimensions

At the time of the Technical Proposal, the Inner Tracker covered an area of 60 cm $\times$ 40 cm around the beam-pipe and the initially proposed silicon detector layout [7] was adapted to these dimensions. In the meantime, however, refined simulation studies had demonstrated that occupancies in the innermost regions of the Outer Tracker had increased to worryingly high levels. In order to reduce peak occupancies in the Outer Tracker, without increasing the overall size of the Inner Tracker, a revised tracking-station layout was adopted [8] that follows more closely the actual distribution of particle densities. In this layout, the Inner Tracker covers a cross-shaped area around the beam-pipe. In stations T1-T3, this cross covers an overall width of approximately 120 cm and an overall height of approximately 40 cm.

1.2.3 Number of Tracking Stations

In the original design of the LHCb experiment as presented in the Technical Proposal, the main tracking system consisted of eleven tracking stations. Station positions were optimised for an "upstream tracking" algorithm, identifying track seeds in the low-field region downstream of the magnet and using a Kalman filter algorithm to follow these seeds backwards through the magnet to the vertex region. In addition, both RICH detectors [9] were sandwiched in between tracking stations that had to provide track seeds for the photon ring search. These stations also had dedicated detection layers to precisely measure vertical track coordinates.

Later, the RICH group demonstrated [10] that these dedicated tracking stations and detection planes could be removed without deteriorating RICH particle identification performance.

More recently, it was decided to remove all of the tracking stations inside the magnet and one of the stations in the low-field region downstream of the magnet. In the revised detector layout, as shown in Figure 1, the main tracking system thus consists of four stations: one station in between RICH1 and the magnet (TT) and three stations between the magnet and RICH2 (T1-T3).

The reduction of the number of tracking stations is part of an overall effort to reduce the amount of material in the LHCb detector[1] and is made possible as a result of a changed track reconstruction philosophy. Several complementary tracking algorithms have been developed that allow to reconstruct charged-particle trajectories using the reduced setup. A full and detailed description of the changes to the LHCb detector, and its expected physics performance, will be presented in a forthcoming TDR.

[1] Taking out five tracking stations corresponds to a material reduction of approximately 15% X_0. This is in addition to a reduction by 6% X_0 that had already been achieved by removing the dedicated RICH tracking layers.

1.2.4 TT Station

The TT station fulfils a two-fold purpose: firstly, it is used to reconstruct the trajectories of low-momentum particles. These are bent out of the acceptance of the experiment in the field of the experiment magnet and thus do not reach stations T1-T3. Moreover, it is used in the Level-1 trigger to assign transverse momentum information to large-impact parameter tracks.

In May 2002, the LHCb collaboration decided that the TT station will be constructed entirely using silicon micro-strip detectors, rather than a hybrid layout with silicon strips and straw drift tubes as in stations T1-T3. This decision was motivated by the observation [11] that an all-silicon station layout provides for a significantly better Level-1 trigger performance.

Similar to stations T1-T3, the TT station consists of four detection layers, with two $\pm 5^\circ$ stereo views sandwiched in between two layers with vertical strips. In contrast with stations T1-T3, however, the TT station will be "split", with a gap of 30 cm in between the second and third detection layers.

The currently considered layout for the all-silicon TT station is sketched in Figure 1.2. All front-end hybrids and associated mechanics are moved to the top and bottom of the sensitive region, outside of the acceptance of the experiment. Silicon sensors in the inner region of the station are connected to their front-end readout electronics via low-mass kapton interconnects.

The layout is based upon the same silicon sensor geometry as used in stations T1-T3, except that the sensors are 500 μm thick. Sensors are 11 cm long, 7.8 cm wide and have 384 readout strips with a strip pitch of 198 μm. The two areas left and right of the beam pipe are covered by nine eleven-sensor long ladders each. Five-sensor long ladders fill the areas directly above and below the beam pipe. Vertically, each ladder is subdivided into several readout sectors, as indicated by different shadings in Figure 1.2. The sectors at the top and

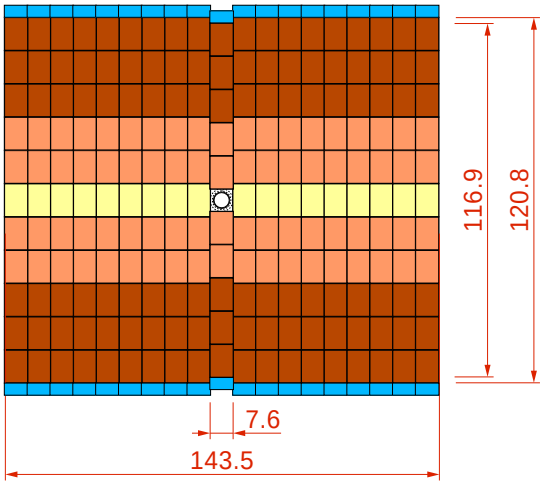

Figure 1.2: Front view of a 0-degree layer in the TT station. Dimensions are in cm.

bottom ends of the ladder each consist of three sensors that are bonded together. They are followed by sectors of two sensors and, for the ladders to the sides of the beam pipe, a central sector consisting of a single sensor. The two-sensor and one-sensor sectors will be read out via 33 cm respectively 55 cm long low-mass interconnects, as indicated in Figure 1.3. A total of 832 silicon sensors and 144k readout channels are used for four detection layers.

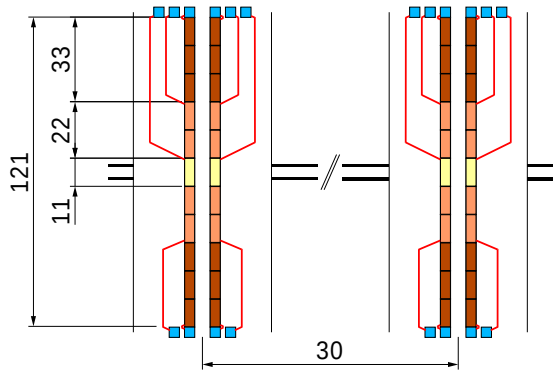

Figure 1.3: Side view with a sketch of the readout scheme for the TT station. Dimensions are in cm.

In order to validate this detector concept, low-mass interconnects have to be designed and the efficiency and noise performance for the different readout sectors have to be measured. The signal-to-noise performance of the detector will be limited by the large capacitances from long readout strips and kapton interconnects. These will also limit the achievable fall-time of the preamplifier signals. The "spill-over" of signals to the following bunch crossings has to be measured and it has to be shown that it can bekept sufficiently small in order not to compromise physics performance.

The operating temperature for the silicon sensors has to be determined, and an appropriate cooling concept must be developed. Finally, ladder supports and station mechanics have to be designed.

Work on this R&D program has started. First prototypes of the low-mass interconnects will be produced by the end of 2002. Investigations of 33 cm long silicon ladders, and a single-sensor ladder equiped with a 55 cm long low-mass interconnect, will be performed in a cosmics test-stand and in test-beams. A first complete mechanical design of the station will be developed by mid-2003. More details on this conceptual design and on the R&D program can be found in [12].

As mentioned previously, the TT station is not within the scope of this TDR. However, the size of this sub-project is comparable to that of the Inner Tracker and therefore has to be taken into account in the planning of the overall Silicon Tracker project described in chapter 6.

1.3 Structure of this Document

This Technical Design Report is intended to be a concise but self-contained description of the Inner Tracker. Further details can be found in the technical notes, which are referenced throughout.

In Chapter 2, an overview is given of the detector layout, in order to motivate the R&D program described in Chapter 3. Results from simulation studies are shown in Chapter 4. The technical design of the Inner Tracker is presented in Chapter 5. The TDR concludes with Chapter 6 on project organisation.

Chapter 2

Detector Layout

The Inner Tracker is a silicon microstrip detector using 320 μm thick single-sided p^+-on-n sensors with a strip pitch of approximately 200 μm. Silicon sensors are 11 cm long and 7.8 cm wide and are assembled on 11 cm (one sensor) and 22 cm (two sensors) long ladders that are connected to a readout hybrid and read out at one end.

In each of the tracking stations T1-T3, the Inner Tracker covers a cross-shaped area around the beam pipe. Each station consists of four independent detector boxes, above, below and to both sides of the beam pipe. A detector box contains four detection layers with vertical or near-vertical readout strips and each detection layer consists of seven staggered silicon ladders. One-sensor ladders are used in the top/bottom boxes, two-sensor ladders in the left/right boxes.

All 28 ladders in a detector box are mounted onto a common cooling plate that removes the heat generated by the front-end readout chips and cools the silicon sensors. This cooling plate also defines the mechanical alignment and the common electrical ground for the silicon ladders. Each detector box is housed in an enclosure that provides thermal, optical, and electrical insulation.

The front-end readout chip samples detector data at the LHC bunch crossing frequency of 40 MHz and stores them in an analog pipeline for the fixed latency of the L0 trigger. Upon a L0-accept, the analog data are read out and transmitted via approximately 5 m long analog copper cables to service boxes located outside the acceptance of the experiment. Here, data are digitised and then transmitted, via 100 m long optical fibres, to the Level-1 electronics boards, located in the LHCb electronics barrack. The Level-1 electronics boards provide interfaces to the data acquisition system and to the Level-1 trigger.

The remainder of this chapter contains concise descriptions of the tracking station layout (Section 2.1), of Inner Tracker detector boxes (Section 2.2) silicon ladders (Section 2.3), and read-out electronics (Section 2.4).

2.1 Station Layout

The three tracking stations T1-T3 are placed at equidistant positions along the beam line in between the downstream face of the LHCb magnet and the entrance window of RICH2. Their nominal z positions are listed in Table 2.1.

Table 2.1: z positions of tracking stations.

	Inner Tracker		Outer Tracker	
	z_{min} [cm]	z_{max} [cm]	z_{min} [cm]	z_{max} [cm]
T1	767.3	782.8	783.8	803.8
T2	836.0	851.5	852.5	872.5
T3	905.0	920.5	921.5	941.5

2.1.1 Tracking Station

Each tracking station consists of four detection layers with a "*xuvx*" topology. The two *x*-

layers have vertical detection cells, the u- and v-layers have detection cells rotated clock-wise, resp. counter clock-wise, by a stereo angle of 5°. This layout provides a precise measurement of track coordinates for momentum determination in the bending plane of the magnet and sufficient resolution for pattern recognition in the vertical coordinate.

A sketch of the front view of a tracking station is shown in Figure 2.1, indicating the sensitive detector elements and the overall dimensions of the active area. The four Inner Tracker boxes are shown, covering a cross-shaped area around the central hole through which the LHC beam-pipe passes the detector. The remainder of the acceptance is covered by long Outer Tracker straw drift-tube modules. The Inner Tracker covers only 1.3% of the sensitive surface of the tracking station, but approximately 20% of all charged particles that are produced close to the interaction point and go through the tracking stations pass through its area.

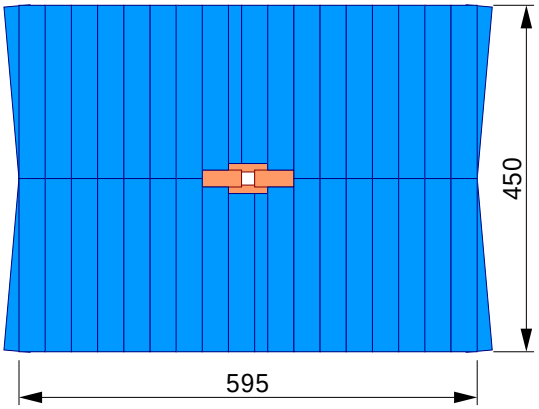

Figure 2.1: Front view of a tracking station. Dimensions are given in cm.

The arrangement of detectors along the LHC beam pipe is indicated in Figure 2.2 which shows a sketch of a top view of a tracking station. The pp-interaction region is to the left. As shown in the sketch, the detector boxes of the Inner Tracker are positioned upstream of the four detection layers of the Outer Tracker, and the left/right boxes of the Inner Tracker are positioned upstream of the top/bottom boxes. Each Inner Tracker box contains four detection layers. The sensitive elements of the different Inner Tracker boxes overlap with each other and with adjacent Outer Tracker modules in both horizontal and vertical direction in order to guarantee full acceptance coverage and allow for relative alignment of the detectors using shared tracks.

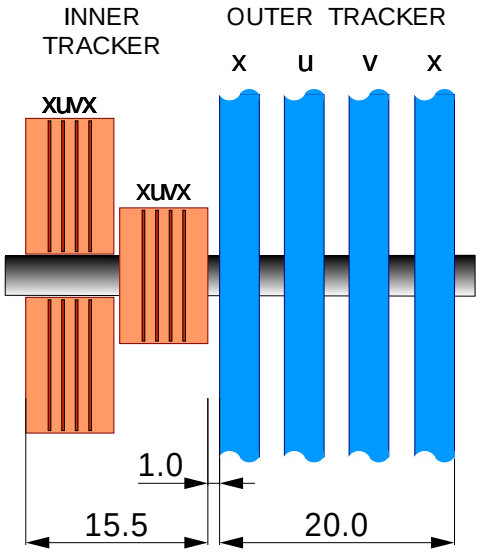

Figure 2.2: Top view of a tracking station. Dimensions along the beam axis are given in cm. Lateral dimensions are not to scale.

2.1.2 Inner Tracker

The concept of a cross-shaped Inner Tracker station, assembled from four detector boxes was first described in [8].

The layout of an x-detection layer and of a stereo layer (u- or v-layer) in station T2 are shown in Figure 2.4. The effective sensitive area covered by an x-layer is sketched in Figure 2.3 and its dimensions for each of the three tracking stations are summarised in Table 2.2.

The inner acceptance of the Inner Tracker is described by a square around the LHC beam pipe. Its size is slightly different for each station, as it follows the conical shape of the beam pipe. The dimensions given in Table 2.2 take into account a distance of 1.2 cm between the outer radius of the beam pipe and the

Table 2.2: Dimensions of the Inner Tracker sensitive area in x-layers. Labels are explained in Figure 2.3.

	$x_{\min} = y_{\min}$ [cm]	x_{cen} [cm]	y_{cen} [cm]	$x_{\max}$ [cm]	$y_{\max}$ [cm]
T1	9.2	26.45	10.9	62.1	20.0
T2	9.9	26.45	10.9	62.8	20.7
T3	10.6	26.45	10.9	63.5	21.4

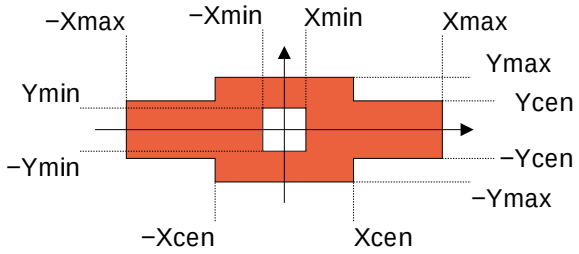

Figure 2.3: Shape of Inner Tracker sensitive area.

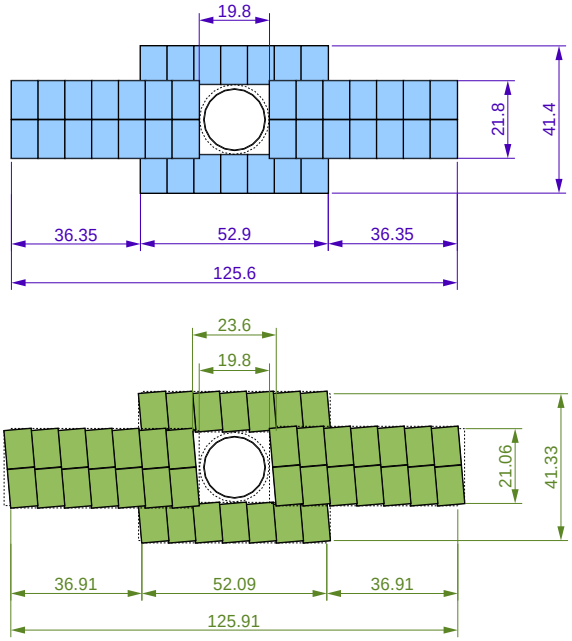

Figure 2.4: Layout of x-layer (top) and stereo layer (bottom) in T2. Dimensions are given in cm and refer to the sensitive surface covered by the Inner Tracker.

inner edge of the Inner Tracker active area. This distance can be broken down into a clearance of 0.5 cm between beam pipe and Inner Tracker mechanics, 0.3 cm thickness of the Inner Tracker insulation box, 0.2 cm clearance between Inner Tracker box and silicon ladder and 0.2 cm dead area on the silicon ladder, the latter being due to ladder mechanics and high-voltage protection (guard ring and n-well) on the silicon sensors.

The shape and the dimensions of the outer acceptance limit were derived from the following requirements:

- average occupancies in the innermost modules of the Outer Tracker should not exceed the level of 10% at the LHCb design luminosity of $\mathcal{L} = 2 \times 10^{32}\text{cm}^{-2}\text{s}^{-1}$ (equivalent to 15% at "high" luminosity of $\mathcal{L} = 5 \times 10^{32}\text{cm}^{-2}\text{s}^{-1}$);
- the sensitive areas of Inner and Outer Tracker overlap by approximately 1 cm;
- the area covered by the expensive silicon microstrip detectors should be kept as small as possible;
- the modularity of standard detectors used in Inner and Outer Tracker should be respected.

The outer dimensions differ slightly for the three tracking stations, due to the increasing diameter of the beam pipe and the use of standard silicon sensors for all stations.

2.2 Detector Boxes

An isometric view of a left/right detector box, assembled from two-sensor ladders, is shown

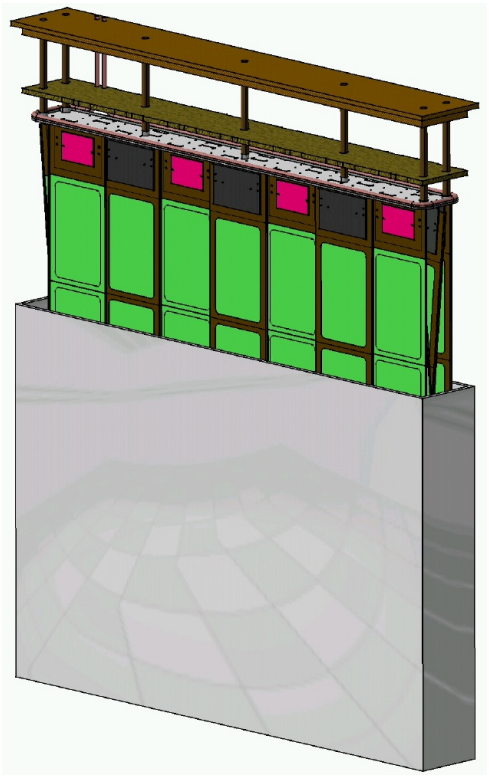

Figure 2.5: Isometric view of a detector box. The box enclosure is shown partially removed such that silicon ladders and the common support mechanics are visible.

in Figure 2.5. Top/bottom boxes are similar except for the fact that one-sensor ladders are used and the box enclosure is correspondingly shorter.

Each detector box contains 28 silicon ladders, arranged in four detection layers. Ladders within a detection layer are pairwise staggered. Adjacent ladders overlap by a few millimetres in order to ensure full acceptance coverage and facilitate the relative alignment of the ladders using hits from shared tracks. They are oriented with silicon sensors alternately facing upstream and downstream, as this allows for minimal staggering distance between silicon sensors.

A close-up of the top part of the detector box is shown in Figure 2.6.

All ladders are individually mounted on a common "cooling plate". This plate will be kept at a temperature of approximately -10°C

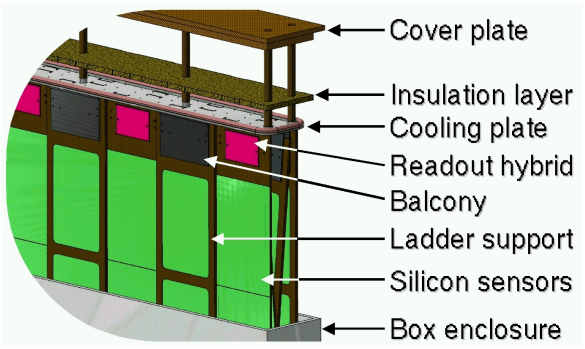

Figure 2.6: Detail of detector box.

in order to remove the heat generated by the front-end readout chips and to provide cooling for the silicon sensors. Liquid C_6F_{14}, running through a cooling pipe attached to the plate is going to be used as cooling agent. The ambient temperature inside the box volume will be approximately 5 °C and the box will be continuously flushed with dry air or nitrogen in order to avoid condensation.

Alignment holes in the cooling plate will be used to precisely position the ladders. These are fixed to the plate via individual L-shaped "balconies". The balconies are an integral part of the silicon ladders and will be described in the next section.

The choice of materials for cooling plate and balconies is the subject of an R&D program that will be described in Section 3.4. Both have to be precisely machined pieces that exhibit excellent thermal conductivity and will need to be made from lightweight materials.

The cooling plate is mounted against a honeycomb cover plate that gives structural strength to the box and carries the weight of the cooling plate and the ladders. All feedthroughs for electrical connections and cooling pipes will be integrated into this honeycomb plate. An additional insulation layer is inserted in between the honeycomb plate and the cooling plate. This reduces the temperature gradient across the honeycomb plate to only a few °C and simplifies the design of the feedthroughs.

The detector box slides into a lightweight enclosure, that is mounted against the honey-

comb plate and provides thermal, optical, and electrical insulation.

The detector boxes underneath the beam pipe will be mounted upside down such that readout hybrids, cooling plate and box mechanics face away from the beam pipe.

2.3 Silicon Ladders

The basic parameters of the single-sided silicon strip sensors are summarised in Table 2.3. Their overall dimensions were optimised to fit the acceptance requirements of the Inner Tracker and fully exploit the usable surface of the 6" silicon wafers from which they are produced. The number of read-out strips was chosen to match the granularity of the 128-channel front-end readout chip. The optimisation of the strip geometry is the subject of an R&D program that will be described in Sections 3.1 and 3.3.

Table 2.3: Basic parameters of silicon sensors.

Technology	p^+-on-n
Thickness	320 μm
Physical dimensions	110 mm $\times$ 78 mm
Length readout strips	108 mm
Number readout strips	384
Readout strip pitch	198 μm
Implant width	$0.25 < w\,/\,p < 0.35$

Detector ladders consist of one or two silicon sensors that are mounted onto a U-shaped support shelf. An isometric view and a sketch of a two-sensor silicon ladder are shown in Figures 2.8 and 2.7, respectively. One-sensor ladders are similar, except that the support shelf is shorter and carries only one sensor. As shown in Figure 2.7, the sensors on a two-sensor ladder are mounted edge to edge and do not overlap. The insensitive region in between the sensors is smaller than 2 mm.

The support shelf is made from a high thermal conductive carbon fibre. It gives mechanical stiffness to the ladder and provides cooling for the silicon sensors. Embedded precision holes allow the accurate mounting of the shelf on the balcony. The balcony is a precisely machined piece, produced from a highly thermal conductive material. It provides the mechanical and thermal contact to the cooling plate described in the previous section. Guide pins ensure the accurate fixation of the carbon fibre support on the balcony and of the balcony on the cooling plate.

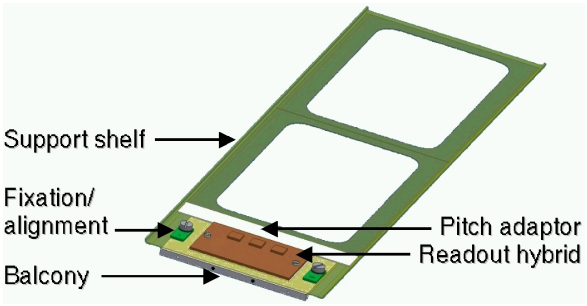

Figure 2.8: Isometric view of a two-sensor ladder. The silicon sensors are not shown in order to display cutouts in the carbon fibre support shelf.

The balcony also acts as the heat sink for the front-end readout chips. Three readout chips are mounted on a four-layer kapton hybrid that is glued onto a thin AlN substrate. This substrate is mounted directly onto the balcony. A direct thermal contact between the substrate and the carbon fibre support shelf is thus avoided, preventing possible heat flow from the hybrids to the silicon sensors. The input pads of the readout chips are directly bonded to a pitch adaptor that is produced in thin-film technique on an Al_2O_3 substrate and provides the electrical interface to the silicon sensors.

The R&D program on ladder mechanics and cooling will be described in Section 3.4.

The kapton hybrid extends into a "tail" (not shown in Figure 2.7) that connects all signal, LV, HV and control lines to the cover plate at the top of the detector box, as sketched in Figure 2.9. The cooling plate contains thin slits at the position of each silicon ladder, through which the kapton tails pass. They are further

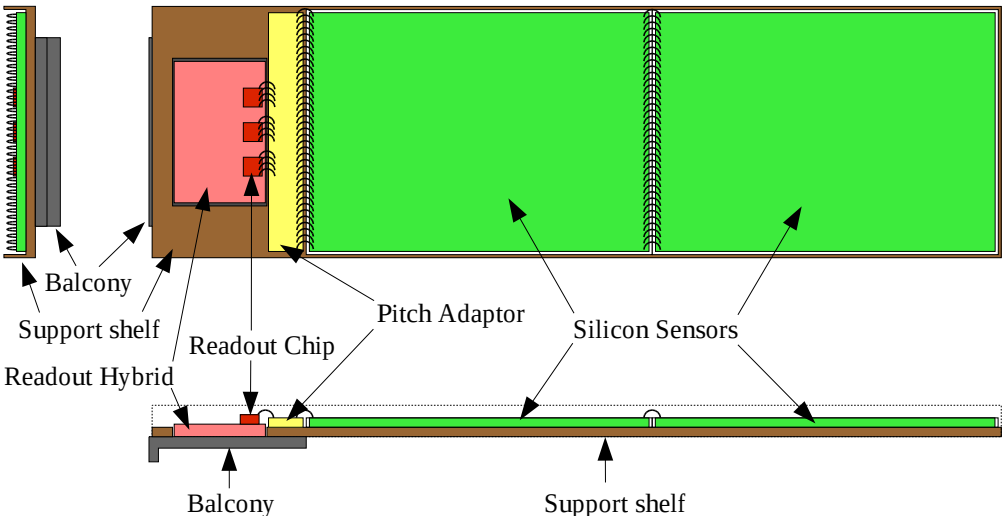

Figure 2.7: Sketch of a two-sensor silicon ladder.

routed around the insulating layer and are inserted in zero-insertion-force connectors on the cover plate.

2.4 Readout Electronics

A sketch of the Inner Tracker readout scheme is shown in Figure 2.10. The Beetle front-end chip [13] is an LHCb custom development in radiation hard 0.25 μm CMOS technology. The chip operates at a sampling rate of 40 MHz. It incorporates 128 channels of fast preamplifiers and active shapers, followed by an analog pipeline in which data are stored during the fixed latency of the LHCb Level-0 trigger. Upon a Level-0 trigger accept, 32-fold multiplexed analog signals are transmitted via four analog output ports.

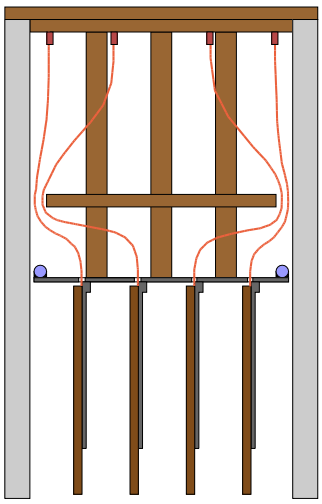

Figure 2.9: Sketch of vertical cross section of detector box, showing routing of kapton hybrid tails to cover plate.

The front-end of the chip was optimised for speed and noise performance in order to cope with the large load capacitances given by the 22 cm long readout strips of the Inner Tracker ladders. A key parameter for the characterisation of the signal shape is the signal remainder 25 ns after the maximum, i.e. at the time of the next LHC bunch crossing. This determines the probability with which a detector signal generated by a particle in the previous bunch crossing can pass clustering algorithms and lead to a "ghost" hit in a triggered event. On the other hand, faster signal shape implies higher Johnson noise, especially for high load capacitances. A careful design of the front-end amplifier and the optimisation of its operating parameters is thus required. The acceptable ghost rate and thus the acceptable signal remainder depend on the particular tracking algorithm. A study of the Level-1 trigger performance [15] has shown that a signal remainder of less than 35% in the VELO [14] is required

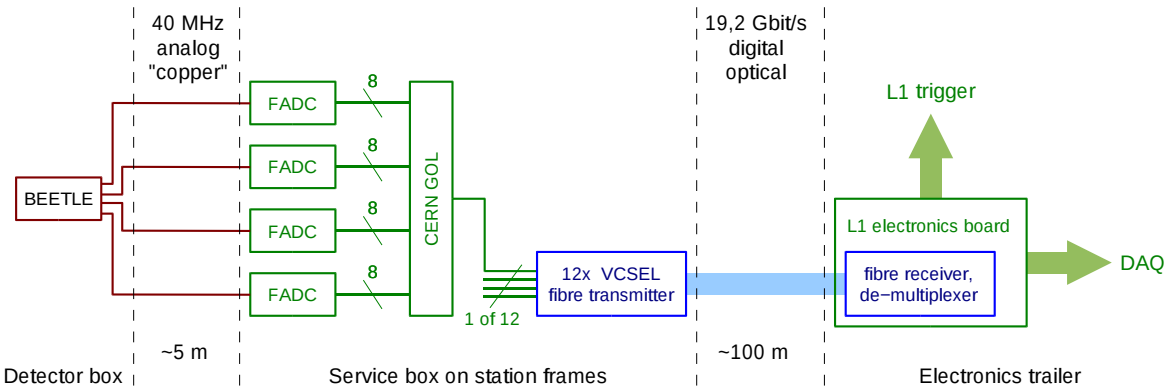

Figure 2.10: Sketch of the readout scheme.

in order to keep the number of ghost hits at an acceptable level. This value can be taken as a guideline for the acceptable signal shape for the Inner Tracker. A detailed simulation study will be performed soon, using the newly developed tracking algorithms.

R&D on the Beetle chip, especially on its front-end, will be described in Section 3.2.

Each detector ladder carries three Beetle chips on a four-layer kapton hybrid. The hybrid incorporates a tail that connects to an interface board on the cover plate of the detector box. Here, the analog signals are re-routed and further transmitted via approximately 5 m long multichannel shielded fine-pitch twisted pair cables to a service box that is located on the frames of the tracking station. In this service box, the analog signals from each Beetle will be digitised using four parallel 8 bit FADC channels and then serialised by a CERN Gigabit Optical Link (GOL) chip [16]. The data from 12 GOL chips, corresponding to four silicon ladders, will be fed into a parallel VCSEL optical transmitter and transmitted via a 100 m long 12-fibre parallel optical cable to the Level-1 electronics located in the LHCb electronics hut. Tests of a prototype readout link will be described in Section 3.5.

Each Level-1 electronics board will receive the data from two 12-fibres cables, corresponding to the data from eight ladders. The Level-1 electronics will perform synchronisation checks, run pedestal- and baseline subtraction algorithms and perform zero-suppression and cluster finding. In addition, they provide an interface to the Level-1 trigger. Upon a Level-1 trigger accept, data are processed and transmitted to the data acquisition system. Prototyping work on the Level-1 electronics board will be described in Section 3.6.

Chapter 3

Summary of R&D and Prototyping

Detector R&D for the Inner Tracker has to a large extent been driven by material budget optimisation. It has concentrated mainly on two issues: the optimisation of silicon sensors and front-end electronics, and the development of light-weight solutions for detector mechanics.

A careful optimisation of the read-out strip geometry of the silicon sensors and the front-end of the read-out amplifier are of crucial importance in order to guarantee good particle detection efficiency using the thinnest possible sensors. As was explained in Chapters 1 and 2, the detector layout calls for the employment of long detector ladders, while the LHCb bunch-crossing frequency requires the use of fast readout electronics. These are contradictory requirements concerning noise performance, since long ladders imply large readout strip capacitances which give rise to significant Johnson noise in fast preamplifiers. The higher the detector noise, the thicker the silicon sensors have to be in order to provide enough signal to ensure good single-hit efficiency. In this context, it is interesting to note that the longest silicon ladders employed elsewhere in LHC experiments are the 16 cm long ladders in the outermost regions of the CMS tracker where 500 μm thick silicon sensors are used. The aim for the Inner Tracker is to use 22 cm long readout strips with 320 μm thick sensors. Results from laboratory measurements on prototype silicon sensors are described in Sections 3.1, R&D on the Beetle readout chip and on a front-end hybrid in Section 3.2, and results from test-beam measurements in Section 3.3.

Besides material budget optimisation, an important design criterion for the ladder and detector-box mechanics is to ensure an adequate operating temperature for the silicon sensors. Due to the large surface covered by each readout strip, shot noise from leakage currents in the silicon sensors can constitute a significant noise contribution after several years of operation if the sensors are not operated at low temperatures. R&D on mechanics and thermal studies are summarised in Section 3.4.

The chapter concludes with summaries of prototyping work for the digital optical readout link in Section 3.5 and for the L1 electronics board in Section 3.6.

3.1 Silicon Sensors

The large surface to be covered by the Inner Tracker, together with moderate requirements on spatial resolution and radiation hardness, calls for a simple and robust design of the silicon sensors.

Single-sided, AC-coupled p^+-on-n strip detectors were selected as sensor technology for the Inner Tracker. A thickness of 320 μm was chosen because it is the minimum thickness that can be expected to give an acceptable signal-to-noise performance for the long silicon ladders employed in the Inner Tracker.

The expected radiation levels in the Inner Tracker do not exceed 1 Mrad and a 1-MeV neutron equivalent fluence of $9 \times 10^{12}\,\mathrm{cm}^{-2}$ after ten years of operation at nominal LHCb luminosity (see Section 4.4). For silicon of in-

termediate bulk resistivity of (3-8) kΩ·cm, type inversion will occur only after approximately $2 \times 10^{13}\,\mathrm{cm}^{-2}$. Radiation damage is thus not a major concern, even if safety factors are taken into account.

The R&D program has concentrated mainly on the optimisation of the strip geometry. A strip pitch of 200-240 μm is suggested by the required spatial resolution, the detector geometry, and the readout chip granularity. Another important parameter is the width of the strip implants. For a given pitch p, the total strip capacitance increases with increasing implant width w [17]. Thus, small values of the width-over-pitch ratio, w/p, are in principle favoured since reducing strip capacitance also reduces preamplifier noise. On the other hand, one of the first results of the R&D program presented in the following sections was that charge collection efficiency in the region in between readout strips deteriorates significantly for small w/p values when fast readout electronics are used.

A careful optimisation of the strip geometry is thus necessary in order to optimise the signal-to-noise ratio S/N that determines the single-hit efficiency of the detector. For this purpose, different strip geometries, using pitches between 198 μm and 240 μm and implant widths corresponding to w/p values between 0.2 and 0.35 were implemented and investigated on prototype sensors.

Two generations of prototype sensors were developed and tested. In this section, technology and geometry specifications of the sensors will be described, as well as their characterisation in the laboratory. Test-beam measurements will be described in Section 3.3.

3.1.1 Technology and Geometry

First prototype sensors were designed and produced by the company SPA Detector in Kiev, Ukraine, from 300 μm thick 4" silicon wafers. A second generation of sensors was designed and produced by HPK in Hamamatsu, Japan. These sensors were produced on 320 μm thick 6" wafers and already have the final overall dimensions foreseen for the Inner Tracker.

Technology specifications and strip geometries for both prototypes are summarised in Tables 3.1, 3.2 and 3.3.

The SPA prototype sensors have a strip length of 66.7 mm, such that 20 cm long ladders[1] could be assembled from three sensors. Two sensors were produced from each 4" wafer: on one sensor, AC metal strips were 2 μm narrower than the p^+ implants, on the other sensor they were 8 μm wider than the implants. The latter was motivated by the observation [18] by the CMS tracker group, that this so-called over-metallisation significantly improved HV performance after irradiation, while it had only a small effect on the total strip capacitance. The HPK prototype sensors all had over-metallised readout strips.

3.1.2 Characterisation of SPA Sensors

A drawing of the corner of a prototype sensor from SPA Detector is shown in Figure 3.1. It shows details such as the fifteen-ring guard ring structure, the bias ring, polysilicon bias resistors, and DC- and AC-contact pads.

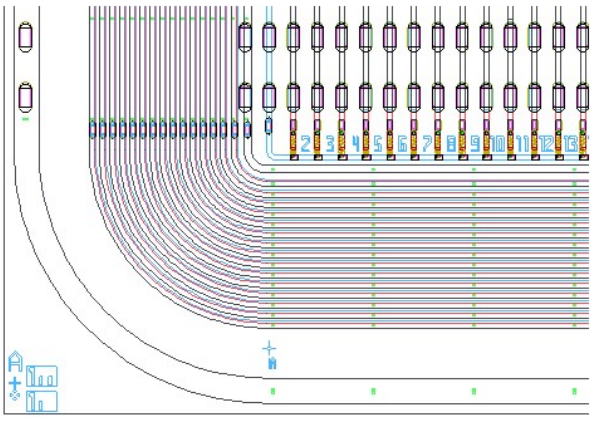

Figure 3.1: Drawing of a corner of a SPA prototype sensor.

Laboratory measurements on these sensors are summarised in [19] and [20]. Measurements of total strip capacitances as function

[1] This was the foreseen ladder length at the time these sensors were designed.

Table 3.1: Technology specifications for SPA and HPK prototype sensors.

Prototype	SPA	HPK
Wafer size	4”	6”
Wafer thickness	300 μm	(320±20) μm
Bulk material	n type, oxygenated	n type
Bulk resistivity	(3-8) kΩ·cm	
Crystal orientation	$< 100 >$	
Implant	p^+ type	
Bias resistors	(1.5±0.5) MΩ, polysilicon	
Readout coupling	AC, SiO_2 / Si_3N_4 multilayer	
Coupling capacitance	> 100 pF/cm	> 125 pF/mm^2

Table 3.2: Sensor geometry for SPA prototype sensors.

Overall dimensions		68.7 mm × 17.36 mm			
Active area		66.7 mm × 15.36 mm			
region	strip no.	strip pitch [μm]	implant width [μm]	metal width [μm]	w/p
A	1-21	240	48	46 (56)	0.20
B	22-42	240	60	58 (68)	0.25
C	43-64	240	72	70 (80)	0.30

Table 3.3: Sensor geometry for HPK prototype sensors.

Overall dimensions		110 mm × 78 mm			
Active area		108 mm × 76 mm			
region	strip no.	strip pitch [μm]	implant width [μm]	metal width [μm]	w/p
A	1- 64	198	50	58	0.252
B	65-128	198	60	68	0.303
C	129-192	198	70	78	0.354
D	193-272	237.5	70	78	0.295
E	273-352	237.5	85	93	0.358

of bias voltage (CV-curves) demonstrated that the sensors fully deplete at 50-70 V, as expected for 300 μm thick sensors. However, all delivered sensors exhibited low breakdown voltages of 100-120 V. As an example, Figure 3.2 shows the measured leakage current as function of bias voltage (IV-curve) for one of the sensors.

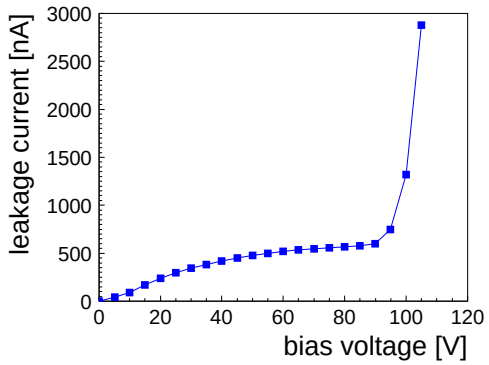

Figure 3.2: IV-curve for SPA prototype sensor.

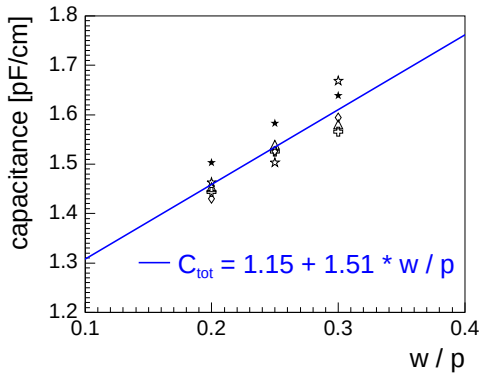

Figure 3.3: Total specific strip capacitances vs. w/p, for over-metallised SPA prototype sensors at 75 V bias voltage. Different symbols refer to different tested sensors.

Total strip capacitances for fully depleted sensors were measured separately for each of the six strip geometries. Measured specific capacitances (per cm strip length) are shown as function of w/p in Figure 3.3, for sensors with over-metallised readout strips. A linear fit to all data points yields the relation

$$C_{tot} = (1.15 + 1.51 \times w/p) \text{ pF / cm}$$

for sensors with over-metallised readout strips, and similarly

$$C_{tot} = (1.01 + 1.55 \times w/p) \text{ pF / cm}$$

for sensors without over-metallisation.

Sensors were also connected to a HELIX [21] readout chip and tested with a 1083 nm infrared laser. The laser beam had a spot size of 7 μm and was scanned in steps of 10 μm across the inter-strip gap in between two readout strips. For every point, the charge collected on each of the two strips was recorded. The fraction of charge collected on the right readout strip is shown in Figure 3.4 as function of the laser position. Figure 3.5 shows the signal on the right strip versus the signal on the left strip. These measurements were performed at a bias voltage of 80 V and indicate a sizeable charge loss in the region in between the strips. If charge collection were perfect everywhere, the measured points should lie on the indicated line in Figure 3.5. This phenomenon was further investigated in subsequent beam tests and will be discussed in detail in Section 3.3.

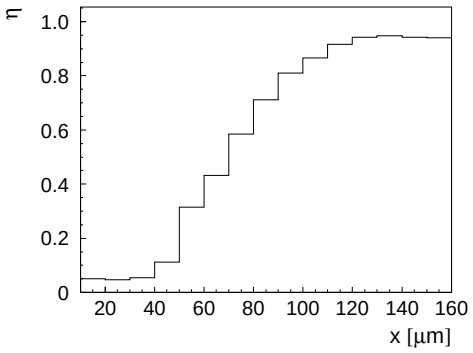

Figure 3.4: Fraction of charge collected on the right readout strip as function of laser position, at 80 V bias voltage.

3.1.3 Characterisation of HPK Sensors

A photograph of a corner of a prototype sensor produced by HPK Hamamatsu is shown in Figure 3.6. Details such as the single guard

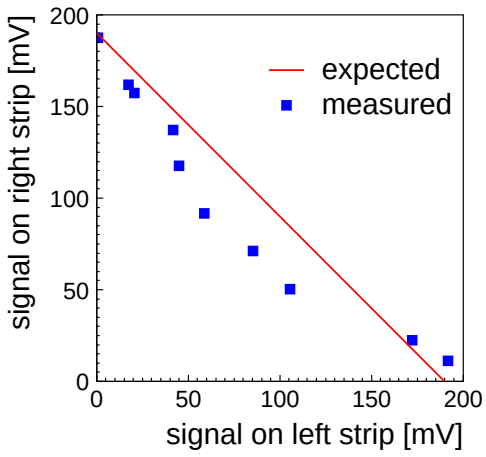

Figure 3.5: Signal on the right strip versus signal on the left strip, at 80 V bias voltage.

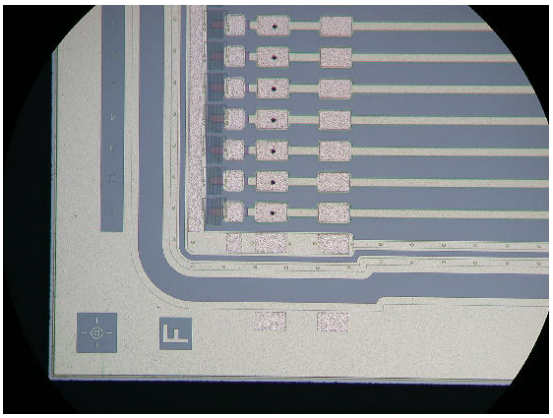

Figure 3.6: Photograph of one corner of an HPK prototype sensor.

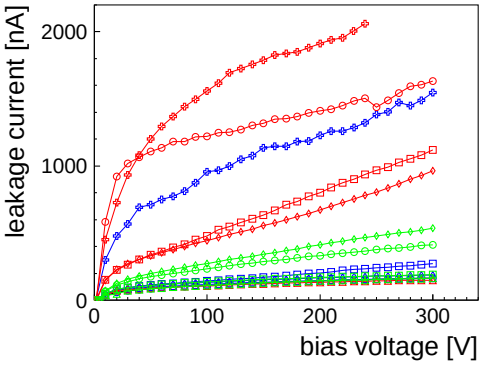

Figure 3.7: IV-curves for HPK prototype sensors. Different symbols refer to different tested detectors.

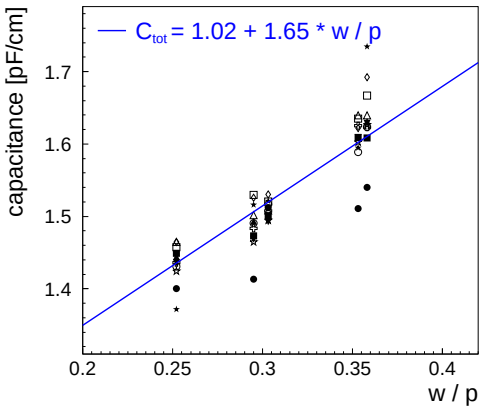

Figure 3.8: Total specific strip capacitances vs. w/p at 80 V depletion voltage. Different symbols refer to different tested detectors.

ring, bias ring, polysilicon bias resistors, and DC- and AC-contact pads can be seen.

Results from the characterisation of these sensors are summarised in [22]. IV- and CV-curves were measured for all 15 delivered prototype sensors. IV-curves where measured up to 300 V, except for one sensor that exhibited a breakdown at 280 V. The measured IV-curves are shown in Figure 3.7. Leakage currents at 300 V were below 500 nA for many, and below 2 μA for all sensors. A sub-sample of the sensors were also tested up to 500 V and none of these showed signs of breakdown.

CV-curves were measured separately for each strip-geometry region. A plot of the measured total specific strip capacitances as function of w/p for fully depleted detectors is shown in Figure 3.8. As was the case for the first-generation prototype sensors, the total strip capacitance increases with increasing w/p for any given sensor but a large spread of absolute values is observed between different sensors. A linear fit to all measurements yields

$$C_{tot} = (1.02 + 1.66 \times w/p)\ \mathrm{pF\,/\,cm},$$

which is compatible with previous measurements.

Using an automatic probe station, a strip-by-strip scan of AC coupling capacitances was performed on a subset of sensors. An example of such a scan is shown in Figure 3.9. The four

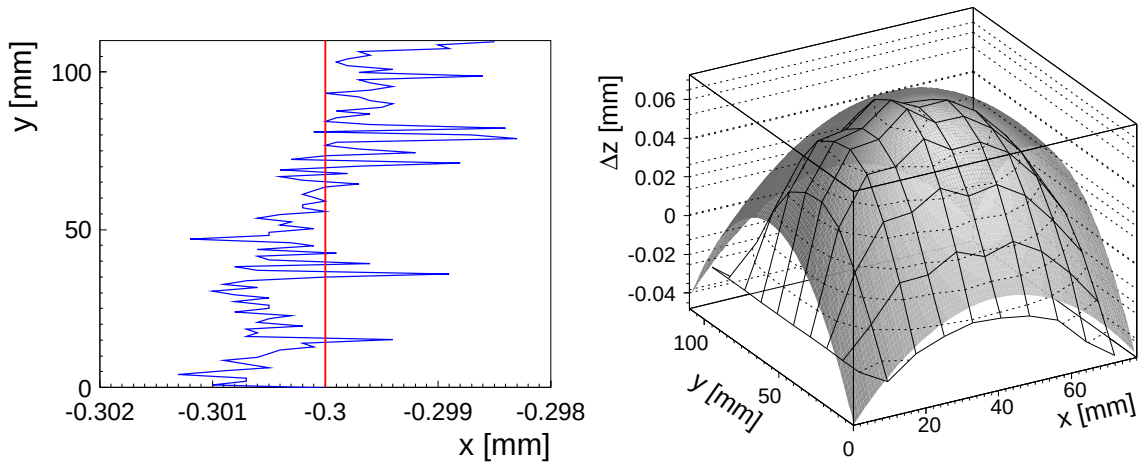

Figure 3.10: Metrological measurements on HPK prototype sensor: nominal and measured position of dicing line as function of position along the edge of the sensor (left) and measured profile of sensor with parabolic fit (right).

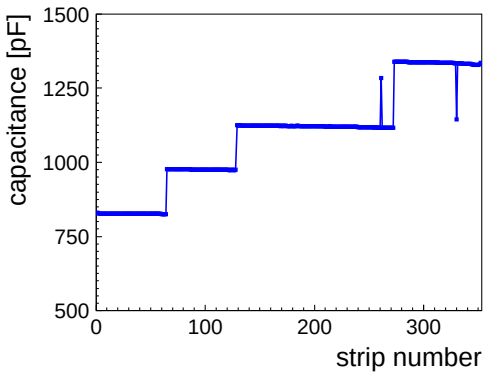

Figure 3.9: AC coupling capacitance as function of strip number.

regions of different strip width (note that strip regions C and D have the same implant width) are clearly visible, as are two "bad" strips with anomalous values of the coupling capacitance. These were found to be due to pinholes in the oxides.

Metrological measurements were performed in order to determine the warp of sensors and the precision of the dicing edge. The latter is of importance for the proposed ladder assembly procedure (see Section 5.2), that relies on the dicing edge for the positioning of the sensors on the ladder. The left-hand plot in Figure 3.10 shows the measured position of the sensor edge for one of four tested sensors. The edge was measured to be parallel with respect to the nominal dicing line to better than $\pm 4\,\mu$m. The average deviation from the dicing line was smaller than $\pm 3.5\,\mu$m for all four sensors.

The measured profile of a sensor is shown in the right-hand plot in Figure 3.10, together with a parabolic fit of the form

$$z = A + B \cdot x + C \cdot y + D \cdot x^2 + E \cdot y^2.$$

All four tested sensors show a systematic warp, the fit giving values of $(2.2 - 2.9) \times 10^{-5}\,\mathrm{mm}^{-1}$ for the parameters D and E. Given the almost perpendicular incidence of particles in LHCb, the measured overall sensor warps between $\pm 40\,\mu$m and $\pm 50\,\mu$m will not contribute significantly to the spatial resolution of the detector. They have, however, to be taken into account in the assembly procedure, in order to ensure good thermal contact of the sensor to the ladder support.

3.2 Front-End Chip and Hybrid

Since no existing front-end readout chip fulfilled the special requirements of the LHCb trigger and readout scheme, a radiation hard readout chip in $0.25\,\mu$m CMOS technology,

called Beetle [13], is being custom developed for the Inner Tracker and the VELO. It is a further development of the HELIX chip [21] that is used extensively in the HERA experiments.

Like its predecessor, it integrates 128 input channels and is based upon the RD20 front-end architecture [23]. Each channel contains a low-noise charge sensitive preamplifier, followed by an active adjustable CR-RC pulse shaper, a 160 cell deep analog pipeline and a 16-cell deep derandomizer buffer for triggered events. Output signals are transmitted 32-fold multiplexed to four output ports. The chip operates at a sampling rate of 40 MHz. The design of the Beetle chip will be described in more detail in Section 5.4.

The development of the Beetle chip started in late 1998. A first prototype of the complete readout chip, the Beetle 1.0, was submitted in April 2000. An error in the layout of the control circuitry of the chip prevented its programming. Using a focused ion beam, a patch could be applied to a small number of chips that could then be used for further debugging.

An improved version of the complete chip, the Beetle 1.1, was submitted in March 2001. It contained a number of bug fixes and is fully functional. However, it does not yet contain SEU resistant digital circuits and its front-end is not yet fully optimised for the large input capacitances of the Inner Tracker. The Beetle 1.1 was tested extensively in the laboratory and submitted to a total ionising dose irradiation up to 45 Mrad. These measurements are described below. Several Beetle 1.1 chips were also connected to Inner Tracker prototype sensors and operated successfully during two test-beams at the CERN–X7 facility in October 2001 and in May 2002. Details about the test-beam measurements are given in Section 3.3.

Several test chips [24] without full functionality were submitted in May 2001. The BeetleSR 1.0 chip was developed to test SEU resistant digital circuits. The BeetleFE 1.1 and BeetleFE 1.2 chips contain a total of twelve different front-end designs using NMOS and PMOS input and feedback transistors. Extensive tests on these chips were performed in order to identify an optimal front-end design for the final chip. These tests are described below.

The latest version of the complete readout chip, the Beetle 1.2, was submitted in April 2002 and received back in August 2002. It contains SEU-resistant digital circuits, the improved front-end design, and a fully differential output driver. The chip is functional and is currently undergoing an extensive test program.

3.2.1 Beetle 1.1 Performance

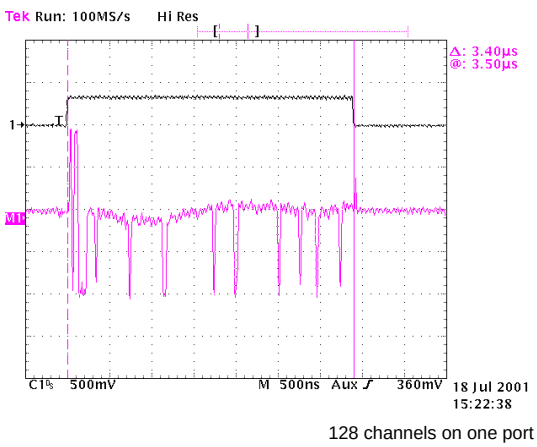

Figure 3.11: Screen shot of Beetle output.

A screen shot of the Beetle output for one readout cycle is shown in Figure 3.11. For this measurement, all 128 input channels were multiplexed into a single output port. The readout sequence starts with an eight-bit encoded pipeline column number, followed by the 128 analog data samples. Signal pulses corresponding to a charge of 22500 e^- were coupled into seven single and two groups of two adjacent input channels.

In a long-term performance test, Beetle 1.1 chips correctly processed 10^{12} random triggers, for effective trigger rates between 100 kHz and 1.2 MHz. No triggers were lost.

One problem found with the Beetle 1.1 chip was a worse than expected performance of the front-end amplifier. The measured peaking time (0-100%), peak amplitude, and remainder

of the signal amplitude 25 ns after the maximum, i.e. at the time of the next following signal sampling, are shown in Table 3.4, for identical front-ends implemented on one of the BeetleFE test chips and on the complete Beetle 1.1 chip. The worse performance on the Beetle 1.1 chip was found to be due to a weak bias current source. This feature has been corrected on the Beetle 1.2 chip.

Table 3.4: Measured signal shape parameters for identical front-ends implemented on the Beetle 1.1 chip and on a BeetleFE test chip.

	Beetle 1.1	BeetleFE 1.1
peaking time	29.2 ns	17.5 ns
remainder	32.6 %	28.7 %

Another limitation of the Beetle 1.1 chip was a too large feedback resistor that caused the preamplifier to saturate for high input signal rates. This has also been fixed on the Beetle 1.2 chip.

The noise performance of the Beetle 1.1 chip was measured for load capacitances of up to 40 pF. A linear fit to the measurements yielded for the equivalent noise current (ENC):

$$\mathrm{ENC} = 871\ \mathrm{e}^- + 41.5\ \mathrm{e}^- \times C\,[\mathrm{pF}]$$

3.2.2 Radiation Hardness

Four Beetle 1.1 chips were submitted to a total ionizing dose irradiation at the X-ray facility of the CERN micro-electronics group in October 2001. A photograph of the setup is shown in Figure 3.12. The chips were powered, triggered and read out during the irradiation. After irradiation, two of the chips were kept at room temperature, the other two were annealed at 100°C. No difference was observed in the performance of these two samples.

The chips were tested up to a total dose of 45 Mrad. They still showed full trigger, readout and slow-control functionality, and only a small degradation of the analog performance was observed. Measured signal shapes,

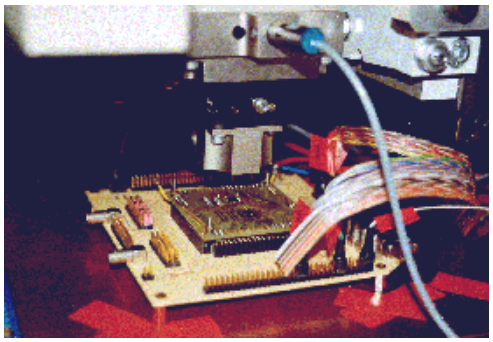

Figure 3.12: Photograph of the total ionizing dose irradiation setup.

for a load capacitance of 3 pF and an input pulse corresponding to 22500 e^-, are shown in Figure 3.13 for different accumulated doses. In Figure 3.14, the signal amplitude, peaking time, and signal remainder after 25 ns are shown as function of the accumulated dose and for different load capacitances. Overall, no significant deterioration of the signal shape is observed up to a dose of 30 Mrad.

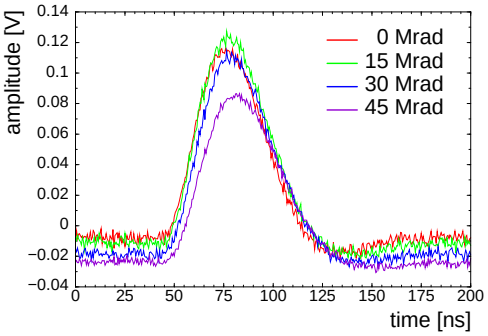

Figure 3.13: Measured Beetle 1.1 signal shape after different irradiation doses, for a load capacitance of 3 pF.

Simulation studies of radiation levels in the LHCb experiment are described in Section 4.4. They have shown that an ionizing dose of up to 1 MRad can be expected at the position of the front-end chips after 10 years of LHCb operation at nominal luminosity. Even applying large safety factors, the Beetle chip will thus survive the full lifetime of the experiment.

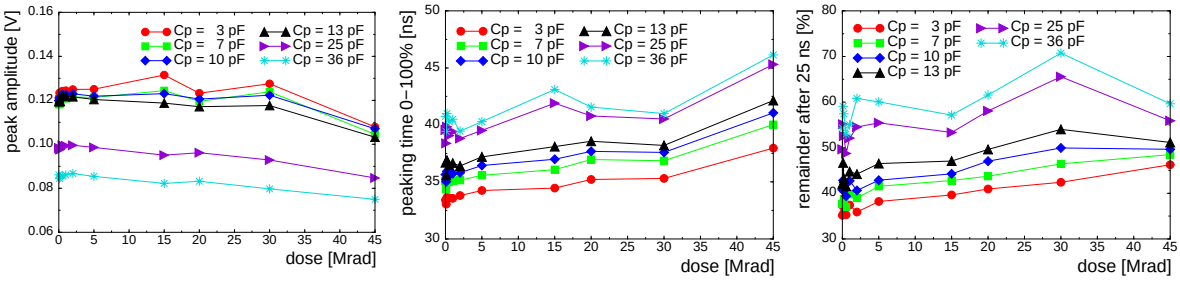

Figure 3.14: Measured Beetle 1.1 signal amplitude (left), peaking time (middle) and signal remainder after 25 ns (right), as function of irradiation dose and for different load capacitances.

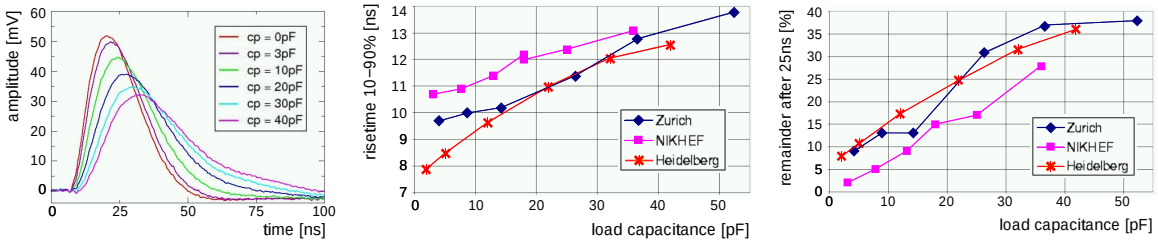

Figure 3.15: Measured signal shape, rise time and signal remainder after 25 ns for the selected front-end for the Beetle 1.2 chip. These measurements were performed on the BeetleFE test chip, at the operation point described in the text.

3.2.3 BeetleFE Tests

The different front-ends implemented in the two BeetleFE test chips are described in detail in [24]. They differ in the technology and size of the employed input transistor, the technology of the feedback transistor and the size of the shaper feedback capacitor. The test chips were studied in detail in three independent laboratory setups at NIKHEF, in Heidelberg and in Zürich. Complementary methods were employed to determine the signal shape and noise performance of the front-ends, for input capacitances of up to 50 pF.

All three groups found compatible results, and based upon these measurements a front-end for the Beetle 1.2 chip was selected. For a certain setting of operating parameters[2], a rise time (10-90%) of below 13 ns and a signal remainder of less than 35% after 25 ns were measured for this front-end, for load capacitances up to 30 pF. The results of these measurements are shown in Figure 3.15.

[2] $I_{pre} = 600\,\mu$A, $I_{sha} = 80\,\mu$A, $I_{buf} = 80\,\mu$A, $V_{fp} = 0$ V, $V_{fs} = 0$ V,

Measurements of the equivalent noise current (ENC) for the same operating point are shown in Figure 3.16. The agreement amongst the three measurements is excellent. Their results can be averaged to

$$\mathrm{ENC} = 450\ \mathrm{e}^- + 47\ \mathrm{e}^- \times C\,[\mathrm{pF}]$$

Adjusting the operating point, the noise performance can be improved further, albeit at the cost of a slightly slower signal shape. This is demonstrated in Figure 3.17, where the measured noise for a load capacitance of 37 pF is shown as function of the signal remainder after 25 ns.

The selected front-end has been implemented in the Beetle 1.2 chip. First measurements on the signal shape and noise performance of the full Beetle 1.2 chip confirm the results [25] that have been measured on the BeetleFE test chip.

3.2.4 Front-End Hybrid

A prototype hybrid carrying three Beetle 1.1 chips has been designed and produced as a so-

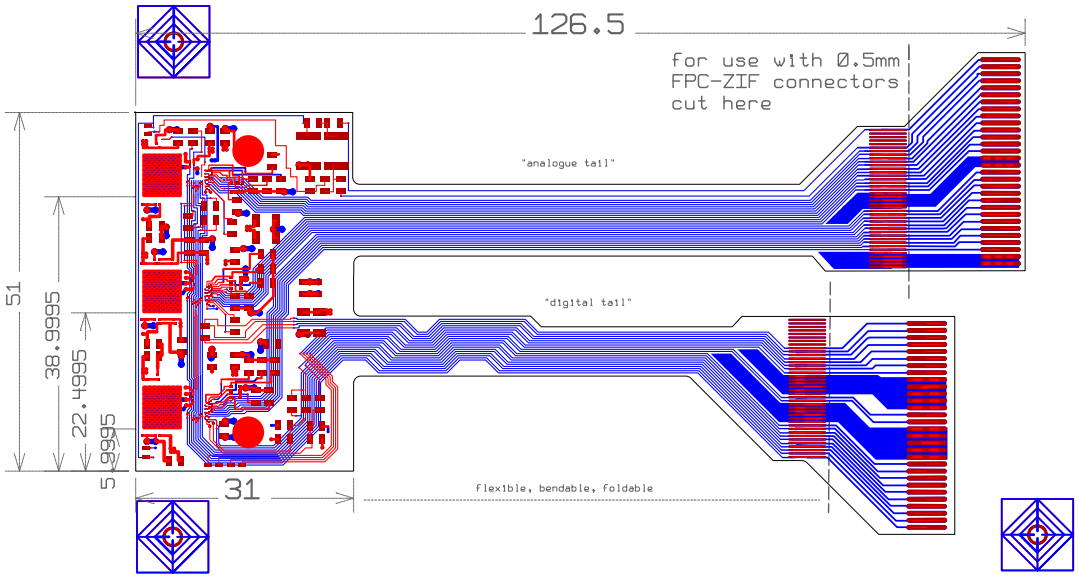

Figure 3.18: Layout of front-end hybrid.

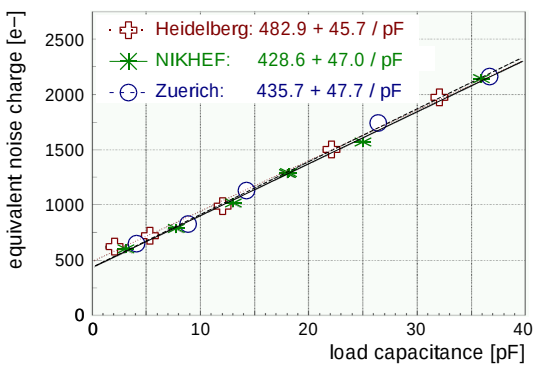

Figure 3.16: Measured noise performance as function of load capacitance for the selected front-end for the Beetle 1.2 chip. These measurements were performed on the BeetleFE test chip, at the operation point described in the text.

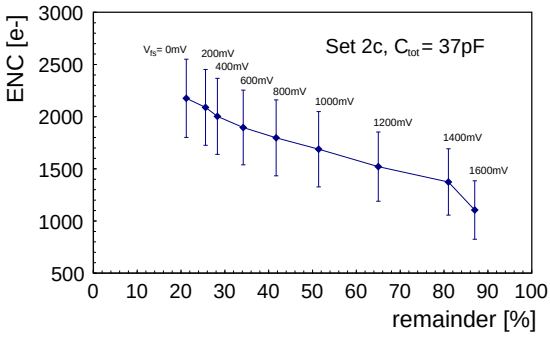

Figure 3.17: Noise performance as function of the signal remainder after 25 ns for the selected front-end for the Beetle 1.2 chip. These measurements were performed on the BeetleFE test chip and a load capacitance of 37 pF. Error bars take into account an overall uncertainty on the noise determination.

called flex-circuit Multi-Chip Module (MCM), using standard PCB manufacturing techniques on polyimide.

The layout of the hybrid and technical details are described in [26]. Four copper layers are used to implement traces for analog and digital signals (two top-most layers) and separate power planes for analog and digital power (two lower layers). The routing was optimised to separate analog lines as much as possible from digital control lines. Beetle chips are glued to the top layer using a conductive epoxy glue and are connected via 25 μm aluminium wire bonds. Passive components are all SMD and soldered to the top layer. The hybrid integrates connections for the detector bias voltage and return current, including a π filter for the sensor bias voltage. Space for a PT100 thermal sensor is foreseen in order to allow monitoring of the temperature on the hybrid.

The hybrid extends into two separate two-layer tails, for analog and digital signals, respectively. The ends of these tails are layed out to fit flexible-printed circuit zero insertion force (ZIF) connectors. In the final detector, this tail will connect directly to the patch panel on the cover plate of the detector box, as described in Section 2.3.

The prototype hybrid was employed successfully to read out the Inner Tracker prototype ladders during the May 2002 beam test.

3.3 Test-Beam Results

In this section, the results from two beam tests are summarised. The first beam test was carried out at the CERN T7 test-beam facility in May 2001, using a beam of 9 GeV pions. Measurements were performed on silicon ladders of SPA prototype sensors connected to HELIX readout chips [21]. The second beam test was performed on silicon ladders of HPK prototype sensors, connected to Beetle 1.1 chips. It was carried out at the CERN X7 test-beam facility in May 2002, using a beam of 120 GeV pions.

In the following, the two beam tests will be referred to as "SPA/Helix" and "HPK/Beetle" test-beams, respectively.

In both beam tests, the setup comprised a beam telescope consisting of two pairs of double-sided silicon strip detectors of the HERA-B vertex detector [27], placed upstream and downstream of the prototype ladders. The single-hit resolution of the beam-telescope sensors was measured to be 14 μm and allowed a determination of the particle impact point in the prototype ladders to a precision of better than 20 μm. Data from the beam telescope and from the Inner Tracker prototype ladders were digitised and written to disk using a data acquisition system provided by the HERA-B vertex group.

Detailed descriptions of the analyses and results from these beam tests are given in [28] and [29].

3.3.1 SPA/Helix Test-Beam

A photograph of the setup in the T7 test-beam area is shown in Figure 3.19. The beam telescope detectors as well as the two installed prototype ladders can be seen. One prototype ladder consisted of a single SPA silicon sensor, the second ladder was assembled from three sensors that were bonded in series to give an effective readout strip length of 20 cm. In the following, the two ladders will be referred to as the "short" and the "long" ladder, respectively. The sensors were glued on G10 frames that had cutouts underneath the sensors in order to minimise multiple scattering. The ladders were mounted on copper blocks that were cooled with water to remove the heat generated by the Helix front-end chips. For data taking, the complete setup was enclosed in a common light-tight, electrically insulating housing.

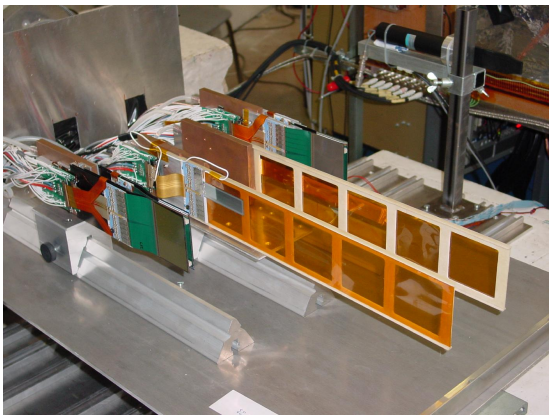

Figure 3.19: Photograph of test-beam setup at T7.

Data were taken with two different operating points of the HELIX front-end amplifiers, corresponding to signal shaping times of approximately 150 ns ("slow" shaping) and 70 ns ("fast" shaping) FWHM, respectively. The latter was the fastest signal shape obtainable with the HELIX chip and is approximately a factor of two slower than operation at LHCb requires. However, the most relevant parameter for this study is the noise performance of the chip, and the noise performance of the HELIX is quite similar to that of the Beetle.

Trigger delay scans were performed in order to determine the optimal HELIX sampling time for further data taking. The delay between the sampling time and the trigger signal was varied, and the most probable cluster charge signal was determined for each of the delay settings. The results of the delay scans for fast shaping are shown in Figure 3.20 and reflect the signal shape of the HELIX chip.

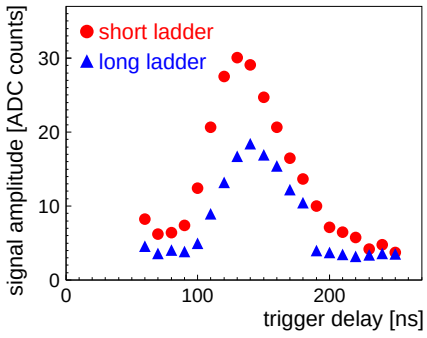

Figure 3.20: Most probable cluster charge as function of trigger delay. These results were measured for fast shaping in the SPA/Helix test-beam.

The employed reconstruction algorithms for pedestal and common-mode subtraction and clustering are described in [28]. The distribution of reconstructed cluster sizes is shown in Figure 3.21. As could be expected from the strip geometry, most clusters consist of one or two strips.

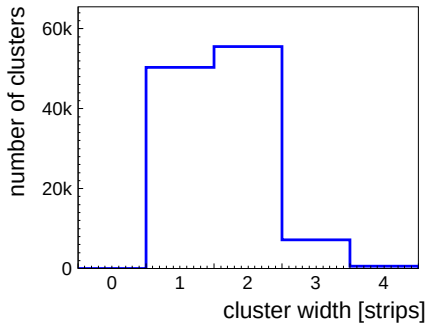

Figure 3.21: Cluster-size distribution for the short ladder in the SPA/Helix test-beam.

The spatial resolution of the prototype ladders was determined from the distribution of residuals of reconstructed hit coordinates with respect to predicted track positions from the beam telescope. For multiple-strip clusters, hit coordinates were reconstructed as the charge-weighted average of strip coordinates, for one-strip clusters the strip coordinate was used. The residual distribution is shown in Figure 3.22. A fit with a single Gaussian gives a one-sigma resolution of 0.196 strip pitches or 47 μm. This is well within the LHCb requirement of 70 μm single-hit resolution.

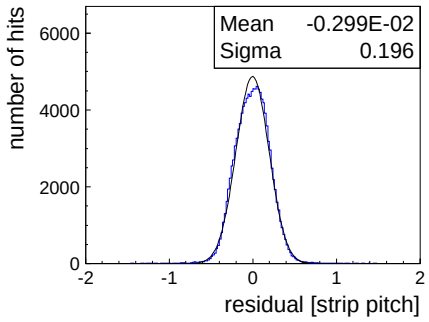

Figure 3.22: Hit residual distribution for the short ladder in the SPA/Helix test-beam.

In Figure 3.23, signal-to-noise (S/N) distributions for the short ladder and fast shaping are shown separately for one-strip and two-strip clusters. For multiple-strip clusters, the signal was determined adding the charges of all strips, whereas noise values were added in quadrature and normalised to the number of strips, i.e.

$$S/N = \sum S_i \Big/ \sqrt{1/n \sum N_i^2} \, .$$

Since correlated strip noise is removed in the common-mode subtraction algorithm, signal-to-noise distributions should be identical for all cluster sizes if perfect charge collection is assumed. However, the measured distributions show a significant shift towards lower S/N values for two-strip clusters compared to one-strip clusters. The two distributions were each fitted with a Landau function folded with a Gaussian. The fits yielded most probable S/N values of 17.4 for one-strip clusters and of 15.0 for two-strip clusters, respectively.

Due to the charge sharing properties, two-strip clusters occur mainly for particles that

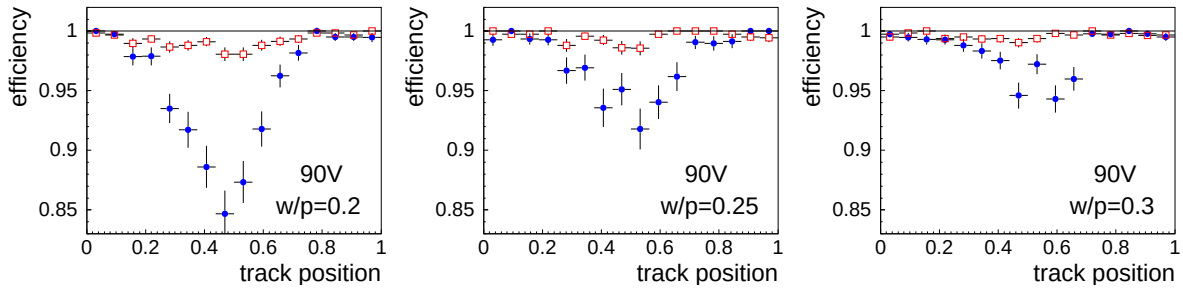

Figure 3.24: Hit efficiency as function of track position in the inter-strip gap, for the different w/p regions. These results were measured for the long ladder in the SPA/Helix test-beam. Filled circles are for fast shaping, open squares for slow shaping.

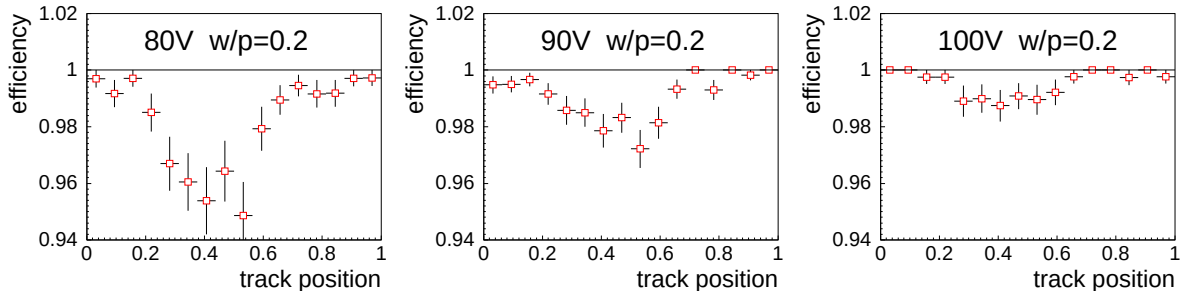

Figure 3.25: Hit efficiency as function of track position in the inter-strip gap, for the $w/p = 0.2$ region and for bias voltages of 80 V, 90 V, and 100 V. These results were measured for slow shaping on the long ladder in the SPA/Helix test-beam.

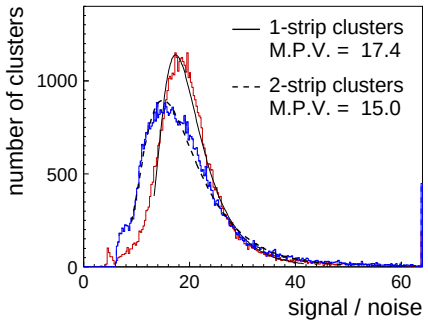

Figure 3.23: S/N distributions for 1-strip clusters and 2-strip clusters for fast shaping and 90 V bias voltage. These results were measured for the short ladder in the SPA/Helix test-beam.

pass in the central region in between two strips, whereas one-strip clusters occur mainly for particles that pass close to a read-out strip. The observation of lower signals for two-strip clusters thus indicates a charge loss in the inter-strip region, confirming the earlier observation of such an effect in the laboratory tests described in Section 3.1.

As expected, significantly worse S/N values were measured for the long ladder, the larger load capacitances leading to higher preamplifier noise. Here as well, a clear deterioration of S/N was observed in the inter-strip region: for fast shaping and 90 V bias voltage, most probable S/N values of 9.0 and 6.9 were found for tracks close to a strip and in the inter-strip gap, respectively. For the long ladder, S/N values in the inter-strip gap became so low that particle detection efficiency was affected. This is demonstrated in Figures 3.24 and 3.25, where reconstructed hit efficiencies for the long ladder are plotted versus the extrapolated track position in the inter-strip gap.

In Figure 3.24, the effect is shown for the different w/p regions on the long ladder, at a bias voltage of 90 V and for fast and slow shaping. In Figure 3.25, it is shown for different bias voltages in the $w/p = 0.2$ region on the long

ladder and for slow shaping. Unfortunately, no data with fast shaping were collected during the bias voltage scan.

An efficiency loss of up to 15% in the inter-strip region was observed for $w/p = 0.2$ and fast shaping at 90 V depletion voltage. The efficiency loss was significantly reduced for slow shaping, and decreased with increasing bias voltage and with increasing w/p. Although preamplifier noise is known to grow with increasing w/p because of higher load capacitances, the improved charge collection efficiency in the inter-strip gap leads to an overall improvement of S/N and efficiency in this region.

In summary, the tests showed that for wide-pitch sensors and fast signal shaping, a significant charge loss occurs in the inter-strip region. This effect was observed both for the short and the long ladder. For the 20 cm long ladder, S/N values in the inter-strip region became so low that the hit efficiency was affected.

Unfortunately, the low breakdown voltage of the employed SPA prototype sensors did not allow to investigate to which extent the loss of charge-collection efficiency would be suppressed at more significant over-biasing.

The problem was further investigated in the second beam test, described below, using HPK prototype sensors and the Beetle 1.1 readout chip.

3.3.2 HPK/Beetle Test-Beam

Photographs of the setup in the X7 test-beam area are shown in Figure 3.26. Prototype ladders and beam telescope detectors were installed in three separate light-tight, electrically insulating boxes, as shown in the left-hand photograph. The right-hand photograph shows the two prototype silicon ladders. One ladder used a single HPK prototype sensor, the other was assembled from two sensors[3]. The sensors were mounted on G10 frames that had cutouts underneath the sensors in order to minimise multiple scattering. Each ladder was read out by three Beetle 1.1 front-end chips that were mounted on the prototype hybrids described in Section 3.2. A pitch adaptor produced in a thin-film technique on a ceramic substrate was used to match the readout strip pitch of the prototype sensors to the input pad pitch of the Beetle chips. The ladders were mounted on to copper blocks that were cooled with water to remove the heat generated by the front-end chips.

In the following, results will be discussed only for the "long" two-sensor ladder, since the 22 cm long readout strips pose the more demanding challenge for signal-to-noise and efficiency performance. A complete description of the beam test, including results from the "short" one-sensor ladder, is given in [29].

Results are shown for three different regions of strip geometry: region C has a strip pitch of 198 μm and an implant width of 70 μm, regions D and E both have a strip pitch of 237.5 μm and implant widths of 70 μm and 85 μm, respectively.

Data were taken with two different operating points of the Beetle 1.1 front-end amplifiers, corresponding to signal shaping times of approximately 35 ns ("fast" shaping) and 70 ns ("slow" shaping) FWHM, respectively. As described in Section 3.2, the slower shaping time gives a better noise performance of the readout chip.

Trigger delay scans were performed in order to determine the optimal Beetle sampling time for further data taking. The delay between the sampling time and the trigger signal was varied, and the most probable cluster charge signal was determined for each of the delay settings. The results of the delay scans for fast shaping are shown in Figure 3.27. They reflect the signal shape of the Beetle 1.1 front-end.

Charge sharing between neighbouring strips is illustrated in Figure 3.28 for strip geometry regions C and E. The fraction of the generated charge that is collected on the right readout strip is plotted as function of the track position in between two neighbouring readout strips.

The residual distribution of reconstructed

[3] One-sensor ladders will be employed in the top/bottom boxes, two-sensor ladders in the left/right boxes of the final detector.

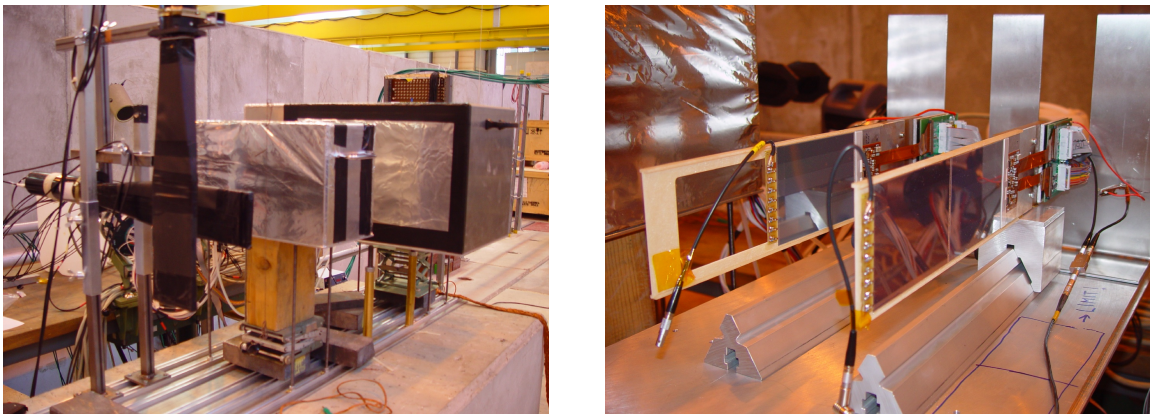

Figure 3.26: Photographs of the test-beam setup at X7.

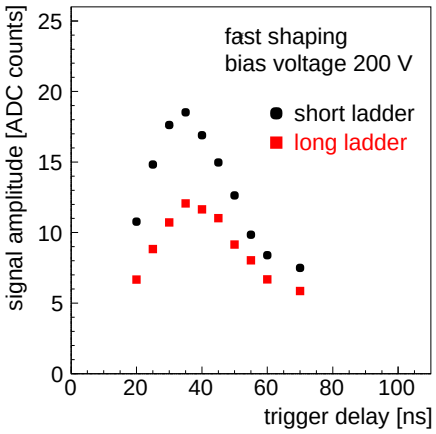

Figure 3.27: Most probable cluster charge as function of trigger delay, measured for fast shaping in the HPK/Beetle test-beam.

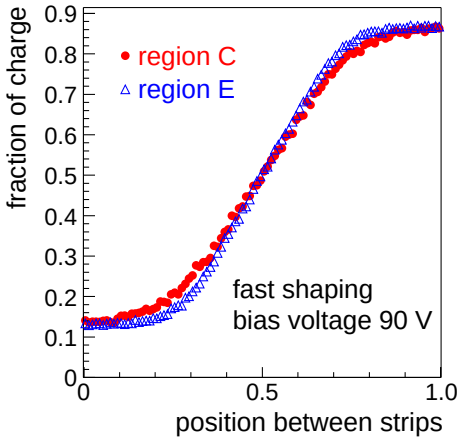

Figure 3.28: Fraction of charge collected on the left readout strip as function of track position between neighbouring strips, measured for the two-sensor ladder in the HPK/Beetle test-beam.

hit coordinates with respect to predicted track positions from the beam telescope is shown in Figure 3.29 for strip geometry region C. For multiple-strip clusters, hit coordinates were reconstructed as the charge-weighted average of strip coordinates, for one-strip clusters the strip coordinate was used. A fit with a single Gaussian gives a one-sigma resolution of 0.23 strip pitches, corresponding to 46 μm.

Measured signal amplitude distributions for strip geometry region C and a bias voltage of 90 V are shown in Figure 3.30. Distributions are shown separately for tracks close to the centre of a readout strip ("tracks on strip") and for tracks extrapolating to the region in between two readout strips ("tracks between strips"). In both cases, the pedestal- and baseline-subtracted signals from the four closest strips to the track were summed. Doing this ensures that the full deposited charge is included in the signal distribution and avoids possible bias from clustering algorithms.

The measured distributions were each fitted with a Landau function convolved with a Gaussian. For tracks on strip, the fit gives a value of 15.7 ADC counts for the most probable signal amplitude. With a measured per-strip noise of 1.43 ADC counts, this translates to a S/N-value of approximately eleven. This result is in good agreement with the expected

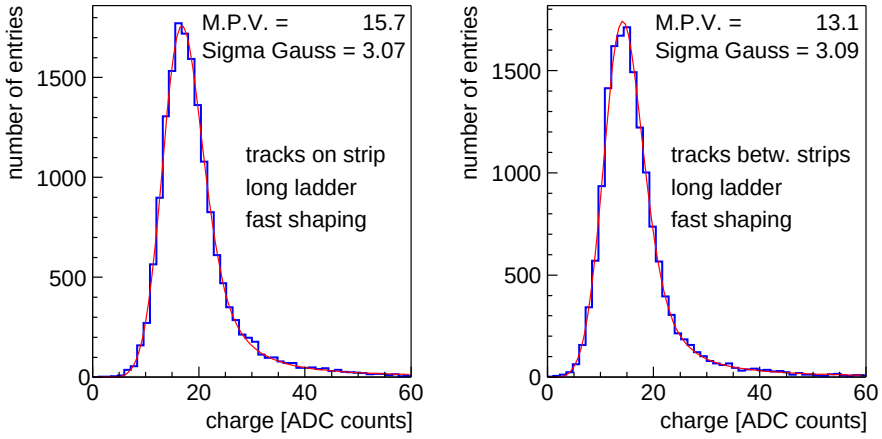

Figure 3.30: Measured signal distributions for tracks passing on top of a readout strip (left) and in between two readout strips (right). These results were measured for region C on the two-sensor ladder in the HPK/Beetle test-beam.

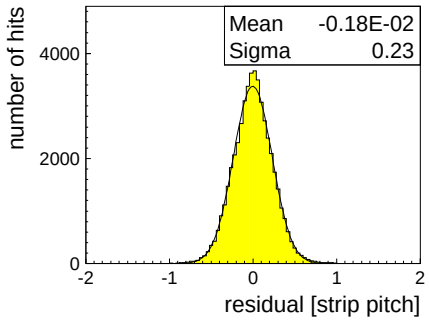

Figure 3.29: Hit residual distribution for strip geometry region C on the two-sensor ladder in the HPK/Beetle test-beam.

S/N-value calculated for 120 GeV pions generating a charge of 25600 e^- in 320 μm of silicon [30, 31], combined with the measured total strip capacitance of 34.4 pF of the test ladder and the measured noise performance of the Beetle 1.1 readout chip (see section 3.2).

The observed signal amplitude distribution for tracks between strips is shifted towards lower values, the most probable signal being approximately 13.1 ADC counts. This observation is consistent with earlier results and confirms that a significant charge loss occurs in the central region in between two strips.

The Gaussian contribution to the width of the signal distribution includes effects from atomic binding effects in silicon, preamplifier noise, digitisation noise and channel-to-channel gain variations. Estimates of these effects are given in [29]. They result in an expected one-sigma width for the Gaussian of 3.16 ADC counts, which is in good agreement with the fitted values of 3.07 and 3.09 ADC counts for the two data samples.

In order to determine the hit efficiency of the prototype ladder, a clustering algorithm was applied on the data. The algorithm is described in [29]. Clustering cuts were adjusted to give a noise hit rate of 0.1% per strip and event.

Reconstructed hit efficiencies for strip geometry region C and fast shaping are shown in Figure 3.31, as function of the track position in between strips and for bias voltages of 90 V and 200 V. For tracks on strip, efficiencies close to 99% are reconstructed for both bias voltages, where the largest part of the observed inefficiency is attributed to ghost tracks from the beam telescope. In the central region in between strips, an additional efficiency loss of approximately 1.5% is observed at a bias voltage of 90 V. This efficiency loss is reduced, but not completely absent for a bias voltage of 200 V.

Reconstructed hit efficiencies as function of the applied bias voltage and for fast shaping are shown in Figure 3.32. Results are shown for the three strip geometry regions C, D and

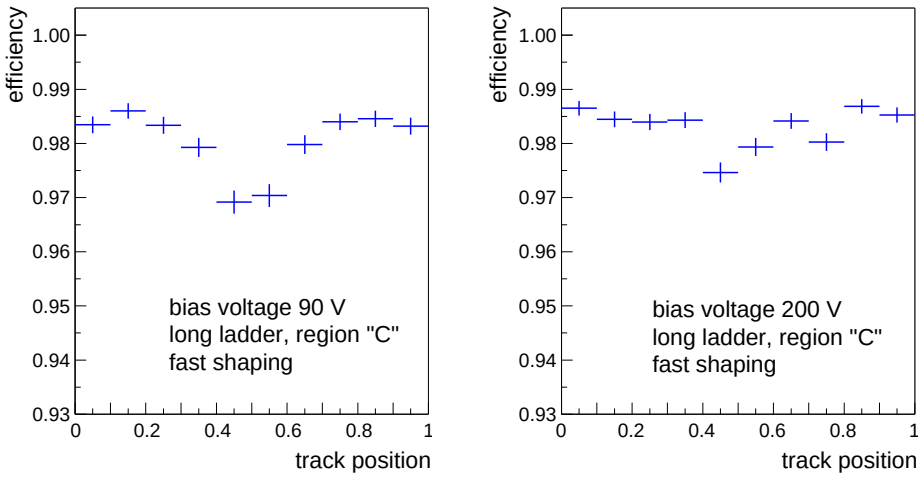

Figure 3.31: Efficiency as function of track position in between strips, for bias voltages of 90 V (left) and 200 V (right). These results were measured for fast shaping on the two-sensor ladder in the HPK/Beetle test-beam.

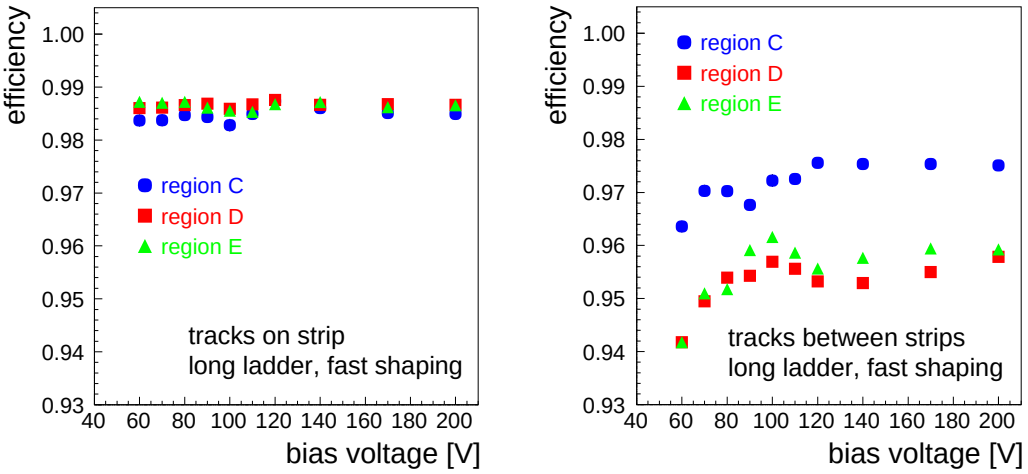

Figure 3.32: Efficiency as function of bias voltage, for tracks passing on top of a readout strip (left) and in between two readout strips (right). These results were measured for fast shaping on the two-sensor ladder in the HPK/Beetle test-beam.

E, and separately for tracks on strip and for tracks in between strips.

For tracks on strip, efficiencies close to 99% are reconstructed for all bias voltages and all strip geometry regions. Again, the largest part of the observed inefficiency is due to ghost tracks from the beam telescope. The efficiency loss in between strips is, however, much more pronounced for regions D and E than it is for region C. The efficiency loss in between strips clearly increases for bias voltages below 100 V, which is consistent with results from the SPA/Helix beam test. However, the efficiency loss does not decrease any further for bias voltages above 120 V.

The same distributions for slow shaping are shown in Figure 3.33. As expected, the better noise performance of the readout chip leads to overall improved hit efficiencies. In between strips, region C still shows a significantly better performance compared to regions D and E.

In summary, hit efficiencies in excess of 99% are found for particles passing close to a readout strip. The test-beam confirms the occur-

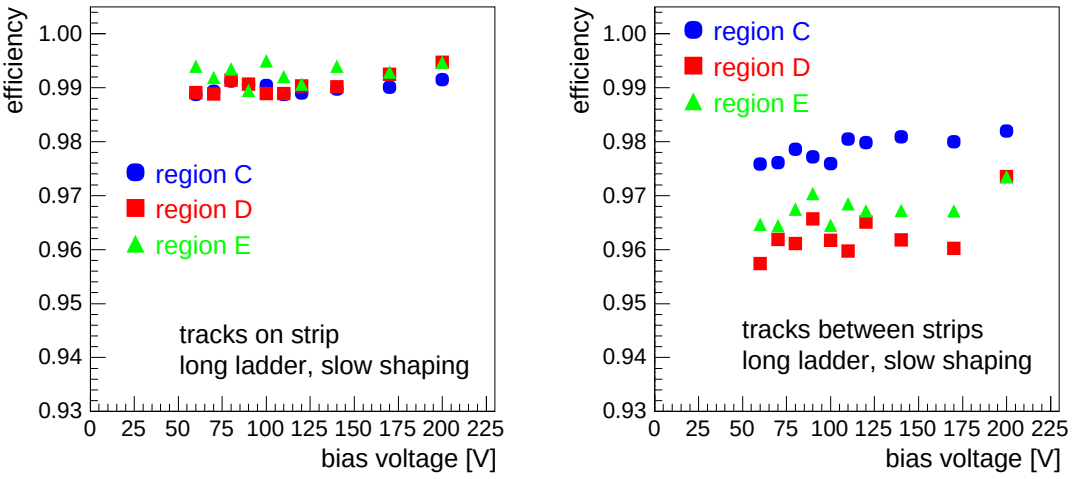

Figure 3.33: Efficiency as function of bias voltage, for tracks passing on top of a readout strip (left) and in between two readout strips (right). These results were measured for slow shaping on the two-sensor ladder in the HPK/Beetle test-beam.

rence of a charge loss in the central region in between strips. This charge loss does not decrease for bias voltages above 120 V. For a strip pitch of 198 μm, fast shaping, and bias voltages above 120 V, an efficiency loss of the order of 1% is observed in the central region in between readout strips. This efficiency loss is significantly more pronounced for the wider strip pitch of 237.5 μm.

In view of the significant charge loss that has been observed in the inter-strip region for the larger pitch of 237.5 μm, it has been decided to adopt a strip pitch of 198 μm for the Inner Tracker. The improved noise performance of the front-end of the Beetle 1.2 chip (see Section 3.2) is expected to add extra robustness such that reliable operation of the detector is ensured.

3.4 Station Mechanics

3.4.1 Detector Box

The layout of the detector box has been described in Section 2.2. A prototype detector box was assembled in order to test production techniques and study the thermal properties of the box.

The goals of the thermal measurements were to determine the necessary wall thickness for the box enclosure, to measure thermal impedances in the cooling path between cooling pipe and silicon ladder, and to demonstrate that the desired ambient temperature of below 5°C can be reached inside the volume of the detector box. Temperature probes were distributed at various points inside and outside the prototype detector box and measurements were performed for a variety of setups, as function of temperature and mass flow of the coolant and for different heat loads. For each setting, the measured temperatures were compared to an empirical cooling model and excellent agreement was found, proving the consistency of the measurements and the validity of the model. These investigations are described in detail in [32].

Setup The prototype box was constructed according to a realistic design but did not yet use the final materials for all components. The cooling plate was machined from 1.5 mm thick aluminium, according to the technical drawing shown in Figure 3.34. It incorporated all cutouts necessary to attach balconies and route kapton readout tails from the silicon ladder to the patch panel at the top of the box. A copper cooling pipe with an outer diameter of 5 mm and a wall thickness of 0.3 mm was

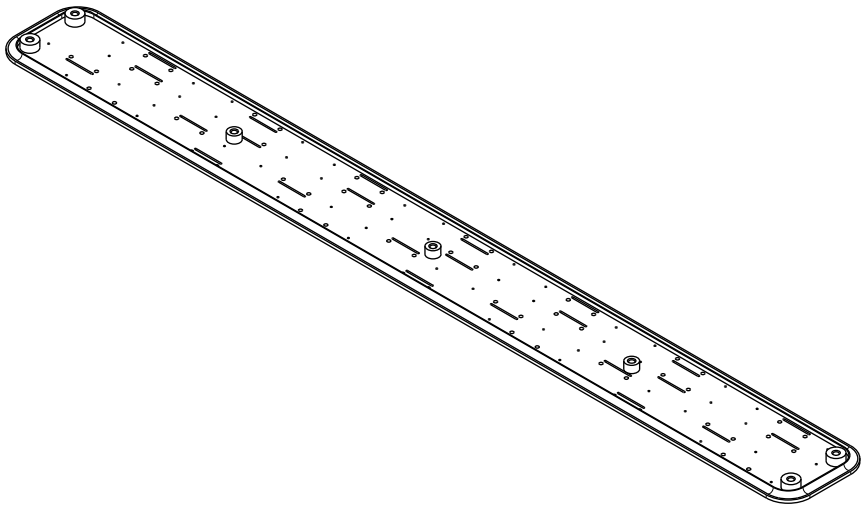

Figure 3.34: Isometric view of the prototype cooling plate. The cooling pipe, alignment fixtures, and slits for routing of kapton tails are shown. The overall dimensions of the plate are 564 mm $\times$60 mm.

glued along the upper edge of the cooling plate. C_6F_{14}, the prefered choice for the final system, was used as a cooling agent. Up to twelve balconies made from aluminium were attached to the cooling plate. They were equipped with kapton heater elements to simulate the power dissipated by the Beetle front-end chips. Silicon ladders were simulated by up to eight 400 μm thin copper sheets that had the same dimensions as the final ladder supports.

The box enclosure was assembled from 6 mm thick sheets of a special class of polyurethane (PUR) foams, called PIR, which is the prefered material for the final detector box. With thermal conductivities of $\lambda = 0.02 - 0.025\,\mathrm{W/(m\,K)}$, PUR foams exhibit the best thermal insulation of all considered materials. Their structural properties are acceptable and they have been tested for radiation doses of up to 100 Mrad. Compared to ordinary PUR foams, PIR stands out for its improved flammability resistance. The PIR sheets were clad on both sides with a 100 μm thin Kevlar tape in order to improve their mechanical rigidity, and a 25 μm thin aluminium foil that provides electrical shielding and acts as an additional vapour barrier. Along the edges of the box, the sheets were bonded together using a special one-component PUR adhesive. Using this technique, strong bonds were achieved and heat leaks that conventional epoxy bonding would entail could be avoided. A photograph of the completed enclosure is shown in Figure 3.35.

The box cover was constructed from a carbon-fibre honeycomb sandwich plate. The cooling plate was mounted onto this honeycomb plate on seven polystyrene rods and an additional insulation layer of 7-8 mm Rohacell was inserted in between the honeycomb plate and the cooling plate. A photograph of the complete setup, including a number of balconies and dummy silicon ladders attached to the cooling plate, is shown in Figure 3.35.

Temperature probes were attached to each of the installed balconies and dummy ladders, to the cooling plate, to the inside and outside walls of the box enclosure, and to the inlet and outlet of the cooling pipe. Additional probes were suspended inside and outside of the box volume in order to measure the respective ambient temperatures.

Cooling Model Measurements were compared to an empirical cooling model that assumed free convection along the cooling plate

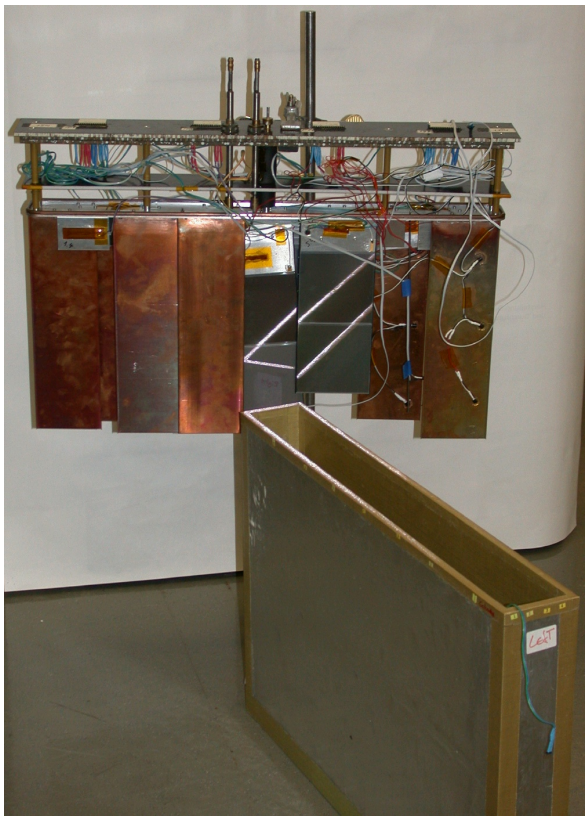

Figure 3.35: Photograph of the box enclosure and the test setup with cover plate, cooling plate and several balconies and dummy silicon ladders.

and the ladders, and along the inside and outside faces of the box enclosure.

The a priori unknown heat exchange parameters for free convection along these surfaces were adjusted to fit measured temperatures from a calibration run. The validity of the model is demonstrated in Figure 3.36, where measured and calculated ambient temperatures inside the box are shown as function of the inlet temperature of the coolant and for two setups. One set of measurements was performed for a setup in which no ladders were mounted on the cooling plate, the other with eight dummy ladders. The lower ambient temperature obtained in the setup with eight ladders clearly demonstrates that the ladders contribute significantly to the cooling of the box.

Wall Thickness The minimum wall thickness of the box enclosure is determined by two

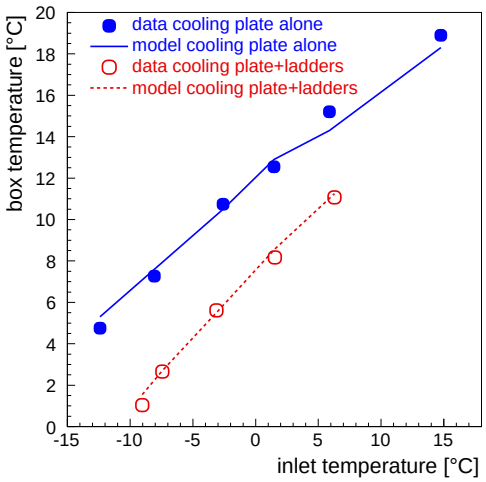

Figure 3.36: Calculated and measured ambient temperatures inside the box, as function of coolant temperature.

conditions: the total heat flow into the volume of the box must be acceptably small, and the temperature on the outside of the wall must be well above the dew point in the experiment hall, in order to avoid condensation on the surface of the box[4].

The cooling model was used to calculate these parameters as function of the wall thickness, assuming a thermal conductivity of the foam of 0.028 W/(m K) and an ambient temperature of 0°C inside the detector box.

The results of this calculation, as function of the wall thickness, are shown in Figure 3.37. For a wall thickness of 6 mm, the calculation gives a heat flow of approximately 30 W through the complete surface of the enclosure. This is acceptable compared to the expected 42 W of heat generated by the 84 Beetle front-end readout chips inside each box. In total, a heat load of 72 W has to be removed from the detector box. A surface temperature of 16°C was calculated for the outside of the wall, which is above the expected dew point.

The calculation also showed that the wall thickness can be reduced to 3 mm for the side walls of the box. For this thickness, the outside

[4]During Delphi running, relative humidities between 30% and 65% were observed. For a temperature of 21°C this corresponds to a dew point between 3°C and 14°C.

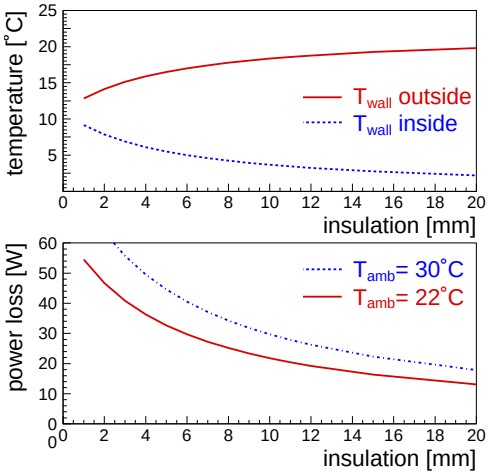

Figure 3.37: Calculated temperatures on inner and outer surfaces of enclosure (top) and heat flow through enclosure (bottom) as function of wall thickness.

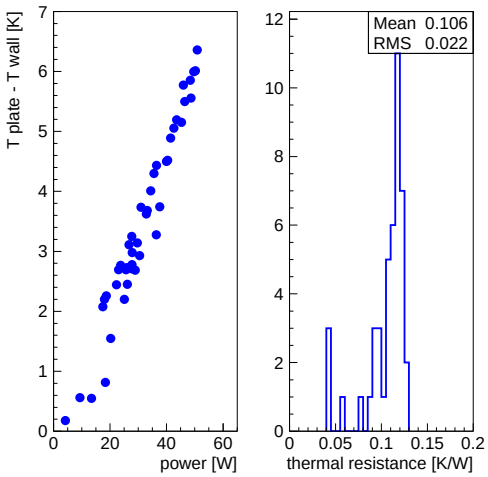

Figure 3.38: Difference between measured temperature of cooling plate and calculated temperature of cooling pipe (left) and resulting thermal impedance of cooling plate (right).

wall temperature is still above 14.5°C and, due to the small contribution of the side walls to the overall surface of the box enclosure, the total heat flow into the box is increased only marginally, by approximately 2 W.

Thermal Impedances The thermal impedance of the cooling plate was determined from the temperature difference between the measured cooling plate temperature and the temperature on the inside wall of the cooling pipe. The latter was calculated from the measured coolant temperature using the equation of Dittus-Boelter [33] for turbulent flow. The result of the measurement is shown in Figure 3.38, as function of the total heat load applied to the kapton heaters.

As expected, the temperature drop across the cooling plate increases linearly with the heat load, and a thermal impedance of 0.11 K/W is calculated. This translates into a temperature drop of more than 8°C for the total heat load of approximately 72 W expected for a complete detector box. As this is not satisfactory, an improved design of the cooling plate is currently being investigated. An additional improvement is expected since the final material for the cooling plate will have a better thermal conductivity than the aluminium that was employed in the prototype setup.

The thermal impedance of an aluminium balcony was similarly determined from the difference between temperatures measured on the balcony and on the cooling plate. A value of 1.6 K/W was calculated, corresponding to a temperature drop of approximately 2°C for a thermal load of 1.5 W from three Beetle chips. This temperature drop is expected to be smaller for the final balcony material, which will have a better thermal conductivity than aluminium.

Temperatures measured at three points along a dummy ladder were compared to calculated temperature profiles from a finite-element analysis. Results for two different cooling settings are shown in Figure 3.39. The finite-element analysis was performed for different values of the thermal conductivity of the ladder, and the best agreement with the measurements was found for a value of 300 W/(m K). This is in reasonable agreement with the tabulated thermal conductivity of 394 W/(m K) for copper. A similar analysis was applied to estimate the thermal conductivity of a prototype ladder support. These investigations will be described below.

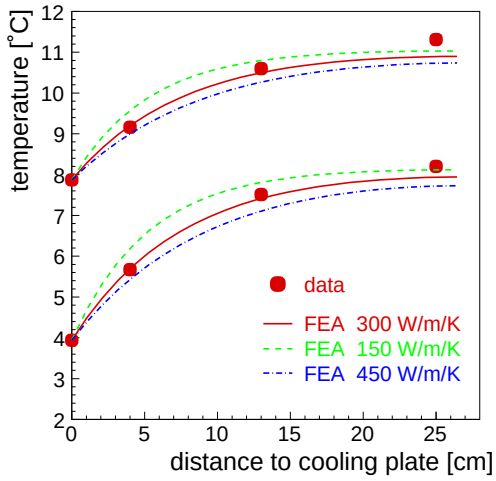

Figure 3.39: Results from FEA calculation compared to measured temperatures on ladder, for two different cooling settings.

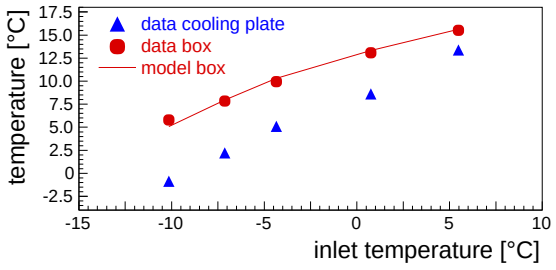

Figure 3.40: Measured ambient temperature inside the detector box as function of the inlet temperature of the coolant.

Ambient Temperature In Figure 3.40, the measured ambient temperature inside the detector box is shown as a function of the inlet temperature of the coolant, for a setup with eight dummy ladders. A heat load of 48 W was generated on the kapton heaters, which is approximately 15% higher than the heat load expected from the 84 Beetle chips in a fully equipped detector box. As for all performed measurements, excellent agreement with the cooling model was found. Unfortunately, the cooling system employed in this setup did not allow to operate at coolant temperatures below -10°C, at which point the desired ambient temperature of around 5°C was just reached. The measurements show an almost linear correlation between coolant temperature and ambient temperature inside the box, and a simple extrapolation shows that in this setup an ambient temperature of around 1-2°C will be reached for the inlet coolant temperature of -15°C that is foreseen for the final detector.

The final detector box will contain 28 ladders instead of the 8 ladders employed in this setup. The corresponding increase of cold surface is expected to further lower the ambient temperature in the box. The effect of the number of installed ladders and of the thermal conductivity of the ladder supports on the ambient temperature in the box was estimated in a calculation that combined the cooling model and the finite-element analysis of the ladder temperature profile in an iterative procedure to determine temperatures inside the box. Results from this calculation, as function of the assumed thermal conductivity of the ladders and of the number of installed ladders, are shown in Figure 3.41. An inlet coolant temperature of -10°C and a total heat load of 72 W were assumed. The results show a continuous improvement with increasing number of ladders and demonstrate that a thermal conductivity of approximately 150 W/(m K) or better is desirable for the ladder supports.

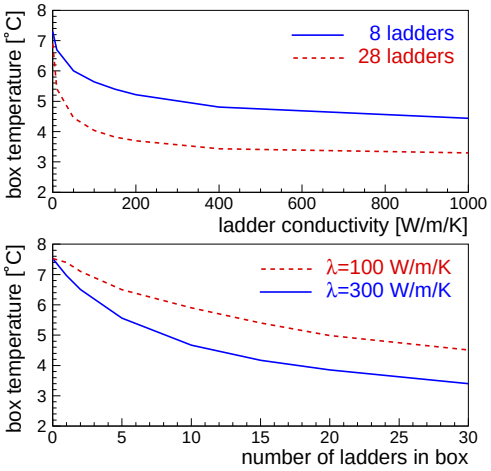

Figure 3.41: Calculated ambient temperature inside the detector box as function of the thermal conductivity of the ladder supports and as function of the installed number of ladders.

The measurements have also demonstrated that the insulation layer that was inserted

in between the cooling plate and the cover plate efficiently shielded the upper part of the box volume from the cold part containing the cooling plate and ladders. For the volume above this insulation layer, ambient temperatures above 15°C were measured for all settings. This greatly simplifies the design of cable feedthroughs through the cover plate.

In summary, the cooling properties of the detector box have been studied in great detail and are well described by a simple, phenomenological cooling model. Extrapolating the measured performance to the final setup, we are confident that the desired ambient temperature of below 5°C inside the detector box will be reached with the described design.

3.4.2 Ladder Supports

The layout of the silicon ladders has been described in Section 2.3. Either one or two silicon sensors are mounted onto a support shelf that fulfils a two-fold function. It gives mechanical rigidity to the ladder, and it provides the thermal contact between silicon sensors and the cold balcony.

The basic requirements on the support shelf are an overall flatness of better than 50 μm in order to allow an accurate positioning of the silicon sensors, and a thermal conductivity of 150 W/(m K) or better. The thermal studies described above have shown that the support shelves then efficiently contribute to the cooling of the detector box volume.

A technical drawing of the end section of a prototype ladder support is shown in Figure 3.42. Precisely machined alignment and fixation holes guarantee the accurate positioning of the shelf on the balcony. A rectangular cutout in the shelf allows to mount the readout hybrid directly onto the balcony, thus avoiding heat flow from the front-end hybrids to the silicon sensors. Two 2 mm high wings along the long sides of the support improve its bending strength.

Several prototype support shelves have been produced according to this drawing at the company Composite Design in Echandens, Switzerland. The production technique and measurements of the thermal and mechanical properties of these prototypes are described in [34].

A carbon-fibre composite material consisting of uni-directional Amoco K1100 carbon fibres impregnated with a cyanate ester resin was used as raw material for the production of the supports. This material is commercially available in sheets of 80-100 μm thickness and was selected for its excellent mechanical and thermal properties. Along the direction of the fibres, a thermal conductivity of 540 W/(m K) and a Young's modulus of 560 GPa are quoted by the manufacturer.

However, a single sheet provides no stiffness in the direction orthogonal to the fibres and multi-layer structures with fibres running along different orientations have to be formed in order to obtain a rigid shelf.

The prototype ladder supports were assembled from four layers, resulting in a total thickness of the shelf of approximately 350 μm. Fibres were oriented along the length of the ladder in two layers, and orthogonal to that direction in the other two. Stiffness in the region of the side wings was further improved by sheets that had fibres oriented at $\pm 45°$.

At the location of the alignment and fixation holes, thin plates of aluminium were glued onto the shelf in order to allow the precision machining of these features.

Thermal Tests In Figure 3.43, a photograph is shown of the test setup that was used to measure the thermal properties of the support shelf. The shelf was mounted onto an aluminium balcony in the same way as in the final setup. The balcony was mounted onto a copper cooling block. Silicon sensors were simulated by two 300 μm thin glass plates of the correct dimensions. Heat dissipation from the front-end chips was simulated by kapton heaters that were glued directly onto the balcony. Temperature sensors were attached at different positions on the support shelf and on the balcony. In addition, the temperature of the cooling block and the ambient tempera-

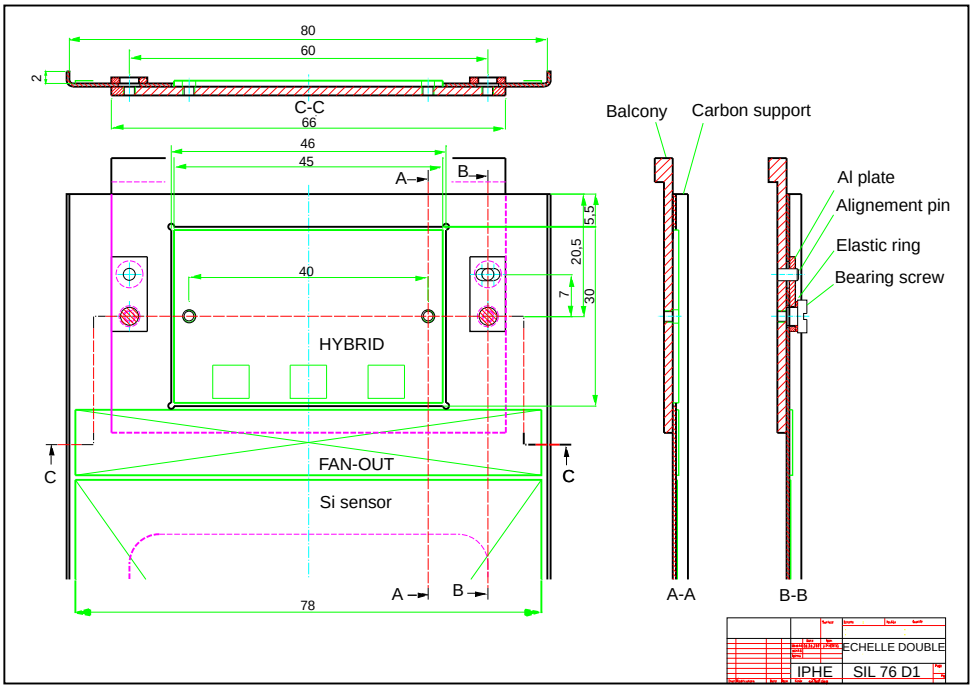

Figure 3.42: Technical drawing of the end section of the prototype ladder support.

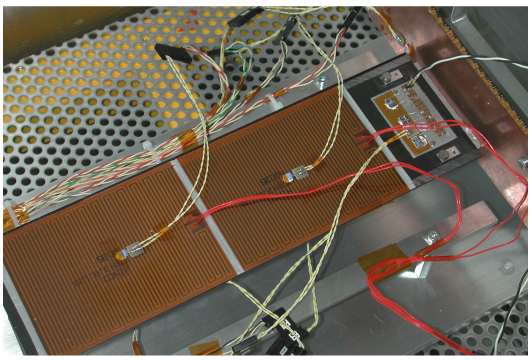

Figure 3.43: Photograph of test setup for thermal measurements on the prototype ladder supports.

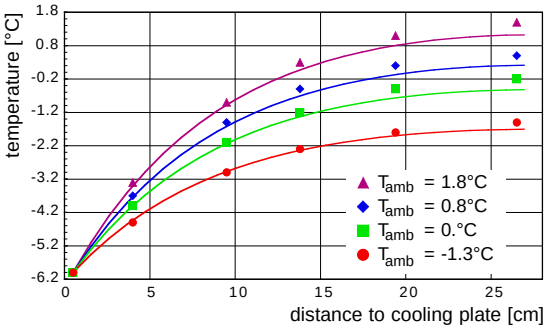

Figure 3.44: Measured (points) and calculated (curves) temperatures on the ladder support.

ture inside the box were monitored. Measurements were compared to a thermal model that used a finite element method to calculate the expected temperature profile along the ladder. The model used an iterative procedure to solve the heat transport equation for each cell element, taking into account conductive and convective heat transport.

Model calculations were performed for different assumed values of the thermal conductivity of the support shelf, and best agreement with data was found for a value of approximately 200 W/(m·K). Measurements and calculated temperature profiles for four different ambient temperatures and a temperature of -6°C on the cooling block are shown in Figure 3.44.

3.4.3 Balconies and Cooling Plate

An extensive R&D program has been launched in order to identify appropriate low-mass materials for the construction of balconies and cooling plate.

A technical drawing of a prototype balcony, including the desired tolerances, is shown in Figure 3.45, a drawing of the cooling plate was shown in Figure 3.34.

The demands on material properties are very similar for the two pieces. The material must allow the precise machining of the alignment and fixation features that are used to position the silicon ladders. It has to provide sufficient flexural strength and has to exhibit high thermal conductivity in order to guarantee efficient heat transfer between silicon ladders and coolant. In addition, it should have a low electric resistance because the cooling plate will be used to define the common ground for all ladders in a detector box. For the cooling plate, a high specific Young's modulus E/ρ is desirable to suppress vibrations that may be induced by the turbulent flow of the coolant. Ideally, balconies and cooling plate should be produced from the same material since construction is simplified if thermal expansion coefficients are matched.

One of the major motivations for the R&D program was to identify materials that combine all these properties and have in addition the longest possible radiation length and nuclear interaction length.

The R&D program is described in detail in [35]. The characterisation of candidate materials included measurements of mechanical and thermal properties. Prototype balconies were machined from several of the tested materials.

Tested Materials For the prototype detector box described above, balconies and cooling plate were machined from aluminium. This material exhibits good thermal and mechanical properties but has a relatively short radiation length. Beryllium and aluminium/beryllium alloys were considered as alternatives. They have significantly larger radiation lengths but are unattractive because beryllium is highly toxic and so very restrictive safety requirements apply for the machining of these materials and lead to a very high production cost.

The R&D program focused on three classes of materials: metal matrix composites (MMC), graphitic foams and carbon-carbon composites (C-C). A total of 14 different materials were investigated.

Three different MMC samples were produced at EMPA Thun, Switzerland. They consist of a magnesium metal matrix that was reinforced either with long continuous carbon fibres (Cytec Thermalgraph 6000X), with short fibres (Cytec DKDX), or with a graphitic foam produced [36] at the Oak Ridge National Laboratory (ORNL). The magnesium infiltration was performed in a squeeze casting process, at a temperature of 700°C. Photographs of three prototype balconies produced from the three different MMC materials are shown in Figure 3.46.

Several samples of graphitic foams of different densities were produced at ORNL. One low-density sample was infiltrated with magnesium as described above, other samples were carbon-vapour infiltrated (CVI) at ORNL. Some samples were encapsulated in epoxy or in a cyanate ester resin.

C-C composite samples were prepared by the high-energy physics detector group at the Institute for Nuclear Research in Cracow. The group has considerable experience in the production of C-C composites and has built several prototype supports for ATLAS silicon pixel detectors. For the study described here, prototype plates were produced from a Toray M55J carbon-fibre fabrics. This material does not exhibit very high thermal conductivity but is well suited for studies of mechanical properties of the produced C-C composite.

Mechanical Measurements In order to assess the machinability of the different materials, prototype balconies were produced and the quality of the precision holes and threads was evaluated by optical inspection. MMC

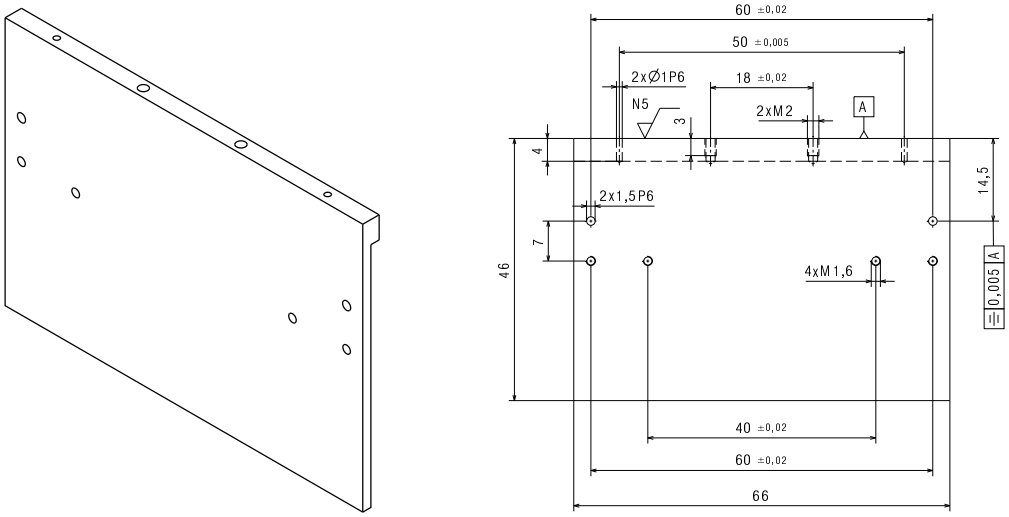

Figure 3.45: Isometric view and technical drawing of the prototype balcony.

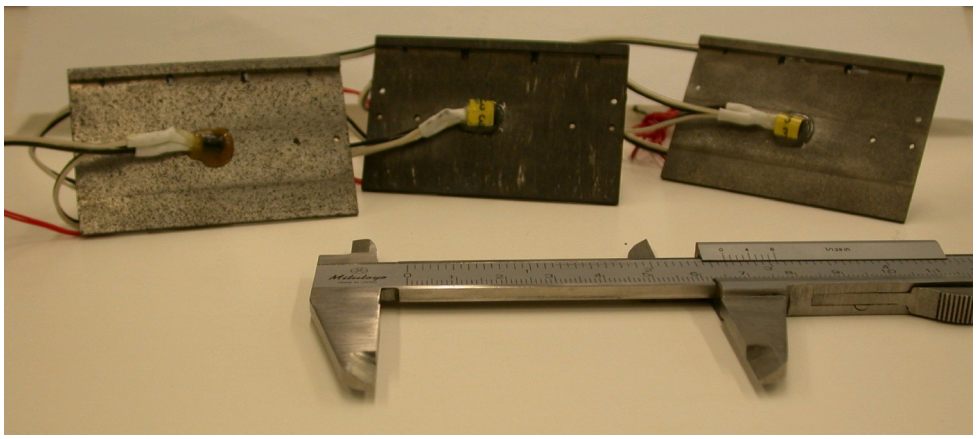

Figure 3.46: Photographs of the three balconies produced from MMC material using graphitic foam (left), short fibres (middle) and continuous fibres (right).

materials with long and short fibres showed the best machinability. Low- and medium-density graphitic foams were machinable only if encapsulated, but even then the quality of threads and precision holes was poor. The very-high density foams could be machined, but an acceptable precision was obtained only for the sample encapsulated in epoxy. The machinability of the C-C samples has not yet been tested.

In addition to these tests, the Young's modulus and tensile strength of standard-sized material samples were determined at EMPA in Dübendorf, Switzerland. The C-C samples were characterised in Cracow. The best results were measured for the long-fibre MMC sample, but the two C-C samples also exhibit acceptable properties. The very-high density graphitic foam samples have not yet been tested.

An overview of the measured mechanical properties is given in Table 3.5 for those material candidates that were machinable with at least acceptable quality. A complete overview of all tested material samples is included in [35]. Aluminium and beryllium are shown for comparison. Material properties for these two materials were taken from literature.

Table 3.5: Compilation of material properties (tbd: to be determined). Values for Al and Be are taken from literature, all others are measured. Values in brackets measured at FhGIKTS.

sample	description	ρ [g/cm^3]	machinability	E [GPa]	strength [MPa]	λ [W/mK]	X_0 [cm]	Λ [cm]
Al	Aluminium (6061)	2.75	very good	69	570	150-190	8.9	39.4
Be	Beryllium (SR200)	1.85	safety!	303	480	200	35.3	40.6
MgLF	MMC, Mg with long fibres	2.05	good	1000-1400	>500	433	17.1	43.5
MgSF	MMC, Mg with short fibres	1.92	very good	63	69.9	89 (78)	16.0	47.7
MgGF	MMC, Mg with graphitic foam	1.86	acceptable	24.2	27.1	82 (76)	15.4	50.5
ORNL 5a	graphitic foam, epoxy encapsulated	1.39	acceptable	tbd	tbd	250	29.8	63.9
Cracow 1	C-C, M55J tissue	1.43	tbd	355	30	118	28.9	60.3
Cracow 2	C-C, M55J in phenolic resin	1.52	tbd	497	28	117	27.2	61.3

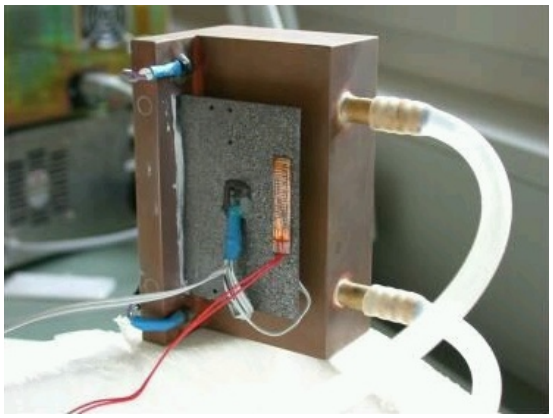

Figure 3.47: Photograph of the setup used to measure thermal conductivities.

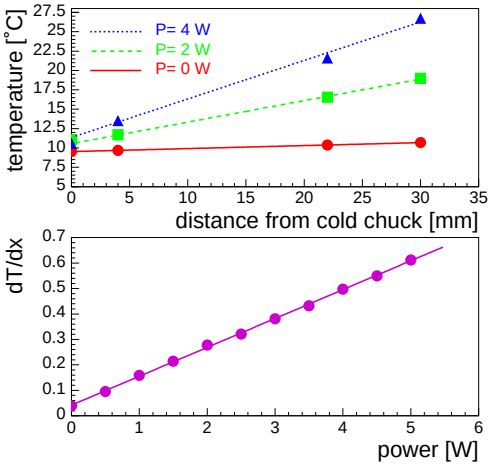

Figure 3.48: Measurement of thermal conductivity on the short-fibre MMC balcony: temperature as function of position for different power settings (upper plot) and temperature gradients as function of power setting (lower plot).

Thermal Measurements A test setup was prepared to measure thermal conductivities directly on the produced prototype balconies. A photograph of the setup is shown in Figure 3.47. The balcony was mounted onto a copper cooling block in the same way in which it will be mounted onto the cooling plate in the final detector. Kapton heater elements were glued onto the far end of balcony and three temperature sensors allowed to measure the temperature profile along the length of the balcony. The complete setup was placed in a thermally insulating box. Large temperature differences between balcony and ambient were avoided in order to minimise convective effects.

The principle of the measurement is illustrated in Figure 3.48 for the example of the balcony from short-fibre MMC. Temperature measurements were performed for up to ten power settings between 0 W and 5 W, and the temperature gradient $\Delta T/\Delta x$ was determined for each setting. With $Q/A = \lambda \cdot \Delta T/\Delta x$ and A the known cross section of the balcony, the thermal conductivity λ of the sample was then determined from a linear fit to the measured temperature gradients as function of the applied heat load Q. The validity of the described procedure was tested on an aluminium balcony. The measured thermal conductivity of 177 W/(m K) is in excellent agreement with values quoted in literature and reproduced in Table 3.5.

In addition to this series of measurements, standard-sized material samples were evaluated at the Fraunhofer Institute für Keramische Technlogien und Sinterwerkstoffe (FhGIKTS) in Dresden, Germany, using a certified comparative method. For all tested samples, results from the two measurements agree within 10-15%.

Thermal conductivities of the C-C samples were determined in Cracow, in a different setup.

The results of the thermal measurements are summarised in Table 3.5. It should be noted that the very high thermal conductivity measured for the long-fibre MMC sample is valid only along the direction of the fibres. Orthogonal to the fibres, thermal conductivities as low as 30 W/(m K) are expected. This is, however, no problem for the application in balconies where heat flow is predominantly one-directional. For C-C composites, higher thermal conductivities should be possible if high thermal conductive fibres are used as base material.

Radiation Length The radiation length and nuclear interaction length for all mate-

rial candidates were calculated, using tabulated values [37] for graphite, magnesium, air and epoxy, and estimated weight fractions for the different material samples. The results of these calculations are listed in Table 3.5. Due to the significant fraction of magnesium, MMC samples have approximately a factor of two shorter radiation length and interaction length than graphitic foams and C-C composites.

Summary In an ongoing R&D program, three low-mass materials have been identified as possible candidates for the production of balconies and cooling plate. Long-fibre magnesium MMC (MgLF) gives excellent results for thermal conductivity and Young's modulus along the direction of fibres and is a promising candidate for the production of balconies and cooling plate. Its radiation length is approximately a factor of two longer compared to aluminium. The other two promising materials do not provide the mechanical qualities that are required to make them candidates for both, balconies and cooling plate. A mixed solution may, however, be feasible. Another factor of two could be gained in radiation length and in interaction length. Very-high density graphitic foam embedded in epoxy resin (ORNL 5a) exhibits long radiation and interaction lengths and a reasonably high thermal conductivity, but its mechanical properties have to be investigated further. It may be a good candidate for balconies but probably not for the cooling plate. C-C composite materials are also very interesting from the point of view of radiation length and interaction length. The machinability of these materials has to be tested. They could be a good candidate for the cooling plate, but probably not for the balconies that require the machining of precise threads.

3.5 Readout Link

The layout of the readout link has been described in Section 2.4. More details can be found in [38]. Analog output data from the Beetle readout chip are transmitted over a distance of approximately 5 m to a service box located on the frames of the tracking station. Here, they are digitised, multiplexed and further transmitted via approximately 100 m long 12-fibre parallel optical links to the L1 electronics in the LHCb electronics hut.

This readout scheme requires that the fully differential analog Beetle output signals are transmitted over a distance of approximately 5 m across the sensitive surface of the Outer Tracker. Detailed tests using realistic cables will soon be performed on the Beetle 1.2 chip.

The R&D program has so far concentrated mainly on the optical part of the link. Appropriate components have been identified and a prototype link has been set up. A sketch of the setup is shown in Figure 3.49.

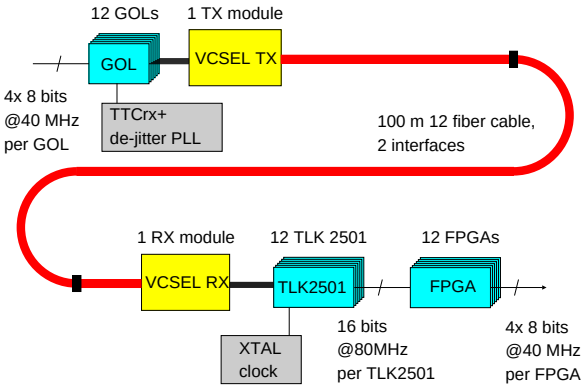

Figure 3.49: Sketch of prototype readout link.

The output signals of a Beetle 1.1 chip were digitised in an 8-bit Analog Devices AD9288 FADC chip running at 40 MHz. The digital data were multiplexed by a CERN GOL chip, and Paracer PR2000 parallel optical converters were used to transmit the data over a 98 m long optical cable. The link included two optical-cable interfaces to simulate a possible installation in LHCb. The observed eye pattern at the receiving end is shown in Figure 3.50. The received data were then de-serialised on a printed-circuit board that carried a Texas Instruments TLK2501 demultiplexer, a low-jitter crystal oscillator and a small FPGA.

For monitoring purposes, the data were further fed into an 8-bit DAC running at 40 MHz to restore the analog data. This allowed an

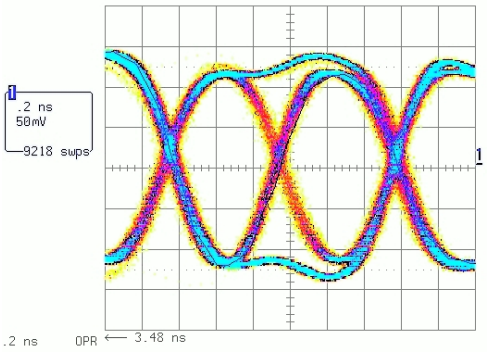

Figure 3.50: Eye pattern at receiving end of optical link.

easy comparison of input and output signals on an oscilloscope. A screen shot of the Beetle output for one readout cycle, before and after transmission is shown in Figure 3.51.

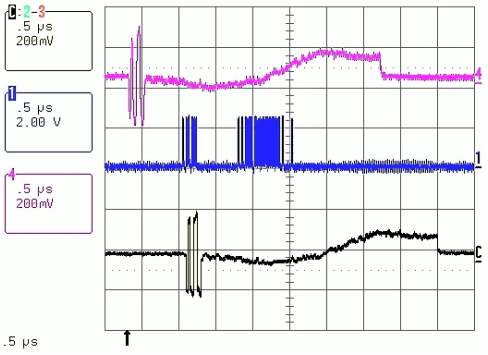

Figure 3.51: Screen shot of Beetle output signal, before (top curve) and after (bottom curve) transmission over 98 m optical link.

A TTCvm unit provided the optical clock source for the 40 MHz master clock. A TTCrm mezzanine card equipped with a TTCrx 3.1 chip was used to decode the optical signal and generate the 40 MHz clock. The resulting clock jitter of 150 ps peak-to-peak was larger than the input specification of the GOL chip, which is 100 ps. This is a known incompatibility of the TTC system and the GOL chip, for which a radiation-hard solution is being developed by the CERN microelectronics group. In this setup, an external low phase noise PLL was fitted to clean up the clock signal, resulting in an acceptable clock jitter that was smaller than 80 ps.

The readout link was operated stably over a period of 7 days, and no errors were observed. A proper bit-error test will be performed soon.

3.6 Level-1 Electronics Board

The Level-1 electronics board receives digitised data via the optical readout links. It has to perform event synchronisation tests, provide data buffering during the latency of the Level-1 trigger, perform algorithms for pedestal subtraction, common mode correction, zero-suppression and cluster finding, and provide interfaces to the Level-1 trigger and the data acquisition system.

The Level-1 electronics board is a common development for the Inner Tracker and the VELO. The requirements for the two subdetectors are very similar, except for the input stage of the board since the VELO are planning to use analog data links and digitise data on the Level-1 electronics board.

Several generations of prototype boards have been developed and tested. The first prototype, called RB1, was a wire-wrap card operating at 10 MHz. The RB2 and RB3 prototype boards are described in the following. The design of a full-size board, the RB4, is currently under way.

3.6.1 RB2 Prototype Board

The RB2 [39] was the first prototype board operating at 40 MHz. It could be equipped with up to four input lines and contained many of the Level-1 electronics features.

It was tested extensively [40] and used to read out prototype silicon sensors in laboratory test setups and in test-beams. Crucial features such as the interfaces to the TTC and ECS systems and the data pre-processing for the Level-1 trigger interface were tested successfully.

A photograph of the board is shown in Figure 3.52. It consists of a 6U VME mother board plus several interchangeable daughter

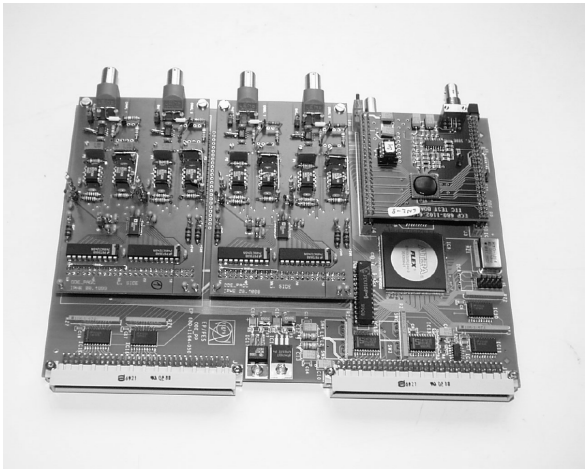

Figure 3.52: Photograph of RB2 prototype board.

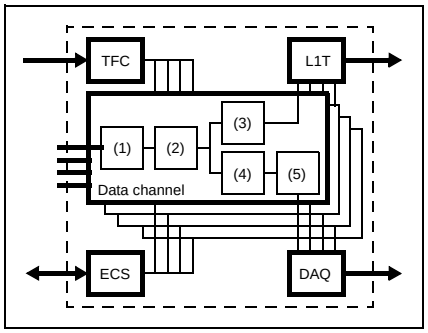

Figure 3.53: Block diagram of RB3 prototype board. Labels are explained in the text.

cards. Firstly, a TTCrx daughter board carries a TTCrx chip that was used to decode the 40 MHz system clock and receive trigger commands. Secondly, a prototype experiment control system (ECS) interface card, based on a 68HC12D60 micro controller, allows remote access to the board via serial interface or CANbus. The on-board EPROMS storing the FPGA configuration data can be programmed via a JTAG interface, while an I^2C interface allows to download operating parameters for TTCrx and DAC devices.

Finally, a Level-1 pre-processor (L1PP) interface card [41] equipped with an Altera APEX100K-2E FPGA working at 80 MHz, was used to test fast zero-suppression algorithms for the Level-1 trigger interface. The prototype card processes 128 channels, which is one quarter of the final L1PP interface. Its performance was tested on Monte-Carlo generated data and on test-beam data. The measured output of the FPGA agreed in all cases with device simulation and the measured contribution of the algorithm to the Level-1 latency was below 17 μs.

3.6.2 RB3 Prototype Board

The RB3 prototype board can receive data from up to 16 input channels and contains the full functionality of the final Level-1 electronics board. Its specifications are layed out in [42]. The board has been produced and testing is under way.

The RB3 is implemented as a standard-size 9U VME module, although the VME backplane is not used. Some functional blocks of the board, for example the link receivers and the Level-1 buffer, are implemented on daughter cards such that different implementations of these blocks can be easily tested during the prototyping phase.

A block diagram of the board is shown in Figure 3.53. The board is composed of four identical data channels that each process data from four input links. Each of these data channel consists of a link receiver (1), a synchronisation logic (2), a preprocessor for the Level-1 trigger (3), a Level-1 buffer (4) and a data processor for the DAQ system (5).

The interfaces to the LHC timing and fast-control system (TFC), the experiment control system (ECS), the Level-1 Trigger (L1T) and the data acquisition system (DAQ) are common for all data channels.

Most of the logic functionality of the board is implemented in FPGAs. The FPGAs are interfaced to the ECS controller to allow for parameter setting, monitoring and testing.

A synchronisation FPGA receives input from four data links, performs consistency checks and formats the data for the Level-1 trigger preprocessor and the Level-1 buffer.

The Level-1 pre-processor FPGA receives data input from two synchronisation FPGAs,

i.e. from eight data links. It performs algorithms for pedestal subtraction, channel masking, common-mode subtraction, hit detection and cluster encoding, and transmits cluster information to the Level-1 trigger interface. The trigger interface FPGA receives event fragments from 8 pre-processor FPGAs and formats them for transfer via an S-link transmitter.

The Level-1 buffer, data preprocessor and DAQ interface are implemented on a daughter card. Several options for the Level-1 buffer are under investigation, the choice of final implementation will be made after further prototype tests. Data received from four synchronisation FPGAs are stored during the Level-1 latency. Upon a Level-1 trigger accept, the data are extracted from the buffer, zero-suppression and cluster finding algorithms are performed, and the data are formatted for transfer to the DAQ via S-link.

Interfaces to the ECS and TFC systems use LHCb standard solutions, as described in [43]. The interface to the TFC system is provided by a TTCrx receiver chip, the ECS interface by a Credit-Card PC (CC-PC). The ECS interface provides read/write access to the internal registers of board components, and allows configuration of the on-board FPGAs.

Chapter 4

Simulation Studies

The Inner Tracker performance studies presented in this chapter are based upon simulations using the LHCb simulation and reconstruction packages, SICBMC and Brunel.

Proton-proton interactions at $\sqrt{s} = 14\,\text{TeV}$ were generated using the PYTHIA (v6.1) event generator [44]. A multiple parton-parton interaction model with varying impact parameter and a running P_T cutoff was used. Model parameters were tuned [45] to reproduce existing low-energy data. Particle decays are simulated using the QQ package [46] that relies, where possible, on measured branching fractions.

The generated final-state particles are followed through the LHCb detector in the SICBMC program that is based upon GEANT3 [47] and contains a detailed description of the detector geometry. Particle interactions and energy loss in the material of the detector are simulated and hit positions in the sensitive detector elements are recorded.

A detailed simulation of the Inner Tracker detector response and a hit clustering algorithm are implemented in the LHCb event reconstruction application program (Brunel).

The implementation of the Inner Tracker geometry and the simulation of the detector response are both described in Section 4.1.

Data were generated using the LHCb detector geometry shown in Figure 1. Relevant changes with respect to the geometry used in similar studies [48, 49] for the Outer Tracker TDR are: the reduction of the main tracking system to four stations (TT and T1-T3), a modified VELO geometry, the implementation of light-weight mirrors in RICH1 and the removal of the magnet shield, such that the magnetic field extends into RICH1. A strip pitch of $240\,\mu\text{m}$ was used in the Inner Tracker digitisation.

Studies of occupancies in the Inner Tracker and Outer Tracker parts of the tracking stations and of momentum resolution in the LHCb spectrometer are described in Sections 4.2 and 4.3, respectively. These studies have demonstrated that the chosen Inner Tracker layout results in acceptably low occupancies everywhere and that the spatial resolution of the Inner Tracker does not limit the achievable momentum resolution.

Track reconstruction in the LHCb detector depends on information from all parts of the tracking system and therefore track and event reconstruction studies have to be discussed in the context of the overall detector layout. They will be presented in a forthcoming TDR.

This chapter concludes in Section 4.4 with the description of a study of radiation levels in the region of the Inner Tracker, using the FLUKA [50] simulation package. Results from this study were used to estimate expected radiation induced leakage currents and determine the operating temperature of the silicon sensors.

4.1 Detector Description

In this section, the implementation of the Inner Tracker geometry in the LHCb simulation package SICBMC, and the simulation of the detector response in the reconstruction package Brunel, are described.

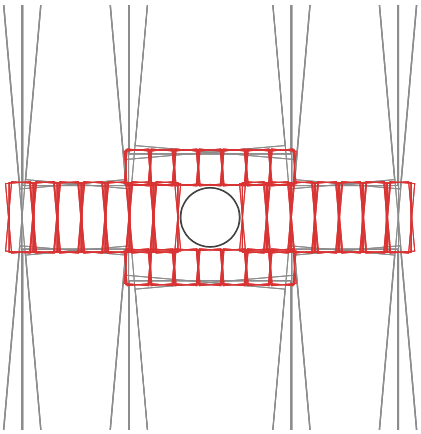

Figure 4.1: GEANT drawing of sensitive detector elements in station T1.

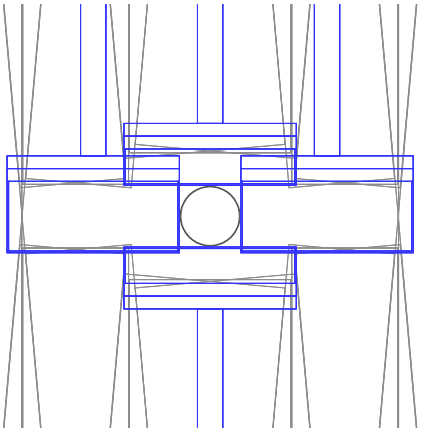

Figure 4.2: GEANT drawing of insensitive detector elements in station T1.

4.1.1 Geometry Description

The geometry description of the Inner Tracker includes sensitive detector elements as well as "dead" material from read-out hybrids and station mechanics inside the acceptance of the experiment. GEANT drawings of the front view of the sensitive and the insensitive elements of a station are shown in Figures 4.1 and 4.2, respectively. A top view of the station, including both sensitive and insensitive elements, is shown in Figure 4.3.

Sensitive detector elements are described in full detail, following the layout described in Section 2.2. Detector overlaps and the staggered z positions of silicon ladders within a detection layer are implemented, as well as individually rotated ladders in stereo views.

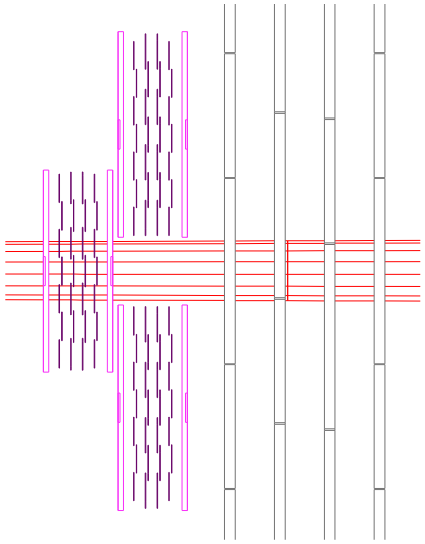

Figure 4.3: GEANT drawing of top view of station T1.

For each simulated track, its entrance and exit points in each traversed sensitive detector element is recorded, as well as its time of flight with respect to the interaction time. This information is used to simulate the detector response.

A simplified description of insensitive detector elements was implemented, in order to speed up the GEANT simulation. The dead material of each detector box was described by a number of rectangular regions that simulate the front face of the box enclosure, its side walls, the front-end hybrids and balconies, and the cooling plate and patch panel above the sensitive detector elements. For each of these regions, the average radiation length of all materials was estimated and simulated by thin walls of material upstream and downstream of the detection layers. Support beams and cables running from the Inner Tracker detector boxes to the outer frames of the tracking station are simulated in a similar way.

4.1.2 Material Budget

The simulated amount of material for each detector box corresponds to 2% X_0 in the sensitive region of the Inner Tracker and to 5% X_0

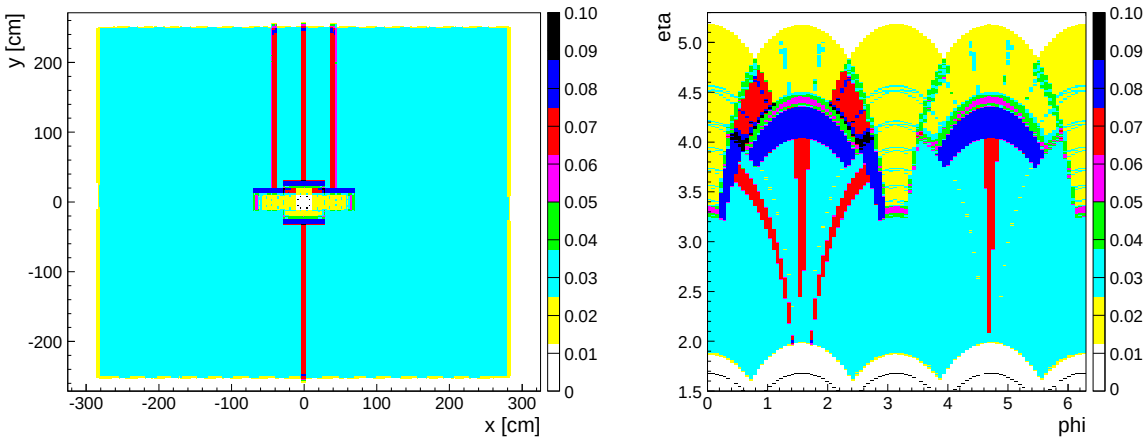

Figure 4.4: "Geantino" scan of material budget (in X_0) in station T2, including contributions from Inner and Outer Tracker. Distributions are shown in the x/y-plane (left) and in η/ϕ (right).

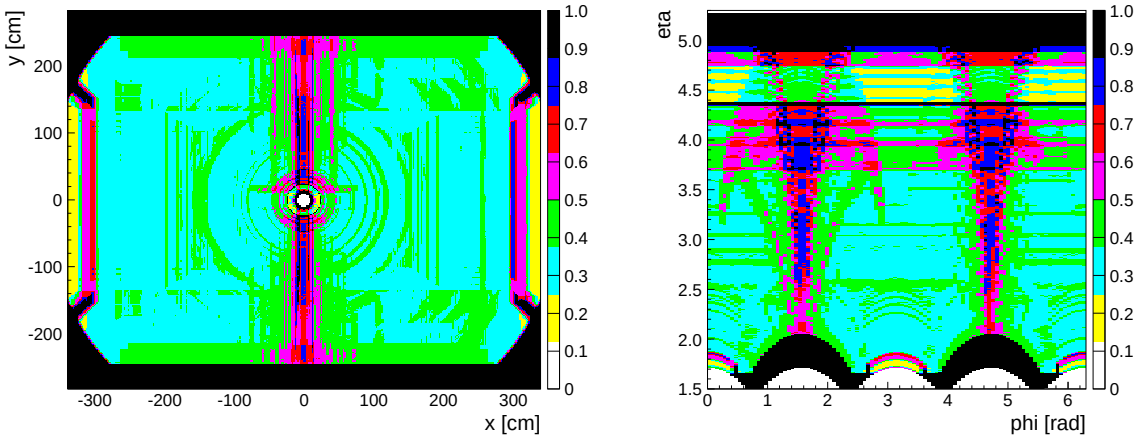

Figure 4.5: "Geantino" scan of integrated material budget (in X_0) from the pp-interaction region up to the front face of RICH2. Distributions are shown in the x/y-plane (left) and in η/ϕ (right).

in an 8 cm high region of front-end hybrids, cooling plate and patch panel. The material budget of the LHCb detector was mapped using "geantino" particles produced in the nominal pp-interaction point. Figure 4.4 shows a map of the radiation length seen by a particle while traversing one tracking station. The shown distribution includes contributions from Inner Tracker and Outer Tracker. The structure of the Inner Tracker is clearly visible, and as expected the material budget is highest in the region where Inner Tracker mechanics overlap the Outer Tracker. A maximum value of approximately 8% X_0 is reached in this area. Maps of the integrated material budget from the pp-interaction region up to the front face of RICH2, just downstream of the last tracking station, are shown in Figure 4.5. Averaged over the acceptance of the experiment, defined as 10 mrad $< \theta <$ 300 mrad corresponding to $5.3 > \eta > 1.9$, the contribution of each Inner Tracker station is 1.4% X_0, namely 0.6% X_0 from silicon sensors and 0.8% X_0 from "dead" material.

4.1.3 Detector Response

The simulation of the detector response is described in detail in [51]. It includes descriptions of statistical fluctuations of charge generation in the silicon sensors, of charge sharing between neighbouring strips, of electronics

noise and of the signal shape of the front-end amplifier. The description of these effects is based upon results from laboratory measurements on the SPA prototype sensors (see Section 3.1) and on the Beetle 1.1 readout chip (see Section 3.2).

The particle trajectory in the silicon sensor is calculated from the GEANT entry and exit points. Charge is generated along the trajectory assuming a constant charge density corresponding to an integrated signal of 24000 e^- per 320 μm of track length. The generated charge is then smeared according to a Landau distribution, which is folded with a Gaussian with a sigma of 1700 e^- in order to take into account effects from the binding energies of electrons [31]. Charge sharing between neighbouring strips is described by an empirical curve that was adjusted to the laser measurements shown in Figure 3.4. The measured points are shown again in Figure 4.6, together with the parametrisation used in the digitisation. The full curve indicates the fraction of charge collected on the right strip, the dashed curve the fraction of charge collected on the left strip. The sum of charges collected on both strips is indicated by the dotted curve and corresponds to a charge loss of approximately 25% in the central region between the two strips. This may be a somewhat conservative assumption in view of recent test-beam results using HPK prototype sensors and the Beetle 1.1 readout chip (see section 3.3).

A Gaussian distributed noise with a sigma of 2000 e^- is added to the charge collected on each strip. Finally, the recorded time of flight of the particle is used to take into account the pulse shape of the front-end amplifier. The latter is simulated by an empirical curve, shown in Figure 4.6, that describes the measured signal shape of the Beetle 1.1 chip for an input capacitance of 30 pF.

Finally, readout strips with a signal of more than 6000 e^- are registered as "hit".

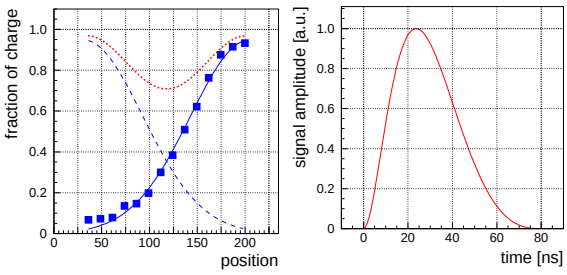

Figure 4.6: Left: Parametrisation of charge sharing between neighbouring strips. Laboratory measurements are indicated by squares, the curves are explained in the text. Right: Parametrisation of front-end amplifier signal shape.

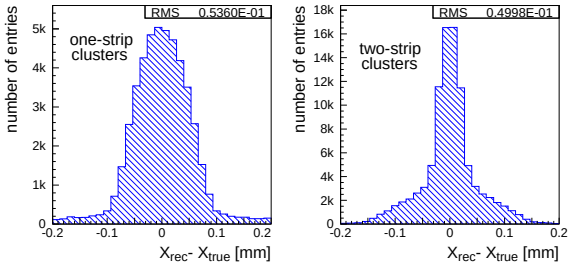

Figure 4.7: Residual distributions of reconstructed cluster coordinates and generated GEANT hit coordinates. Left: one-strip clusters, right: two-strip clusters.

4.1.4 Clustering

A simple clustering algorithm is employed, that looks for groups of consecutive hit strips. For multi-strip clusters, the cluster coordinate is calculated as the charge-weighted average of all strip coordinates. In the case of two-strip clusters, a further correction is applied to correct for the non-linear charge sharing between neighbouring strips. Figure 4.7 shows residual distributions of reconstructed cluster coordinates for one-strip and two-strip clusters. The RMS of the distributions is approximately 50 μm, in good agreement with test-beam results presented in Section 3.3.

4.2 Occupancies

For the occupancy study [52], B$\rightarrow \pi^+\pi^-$ events were generated for the nominal LHCb luminosity of $\mathcal{L} = 2 \times 10^{32}\text{cm}^{-2}\text{s}^{-1}$. The effects of multiple pp-interactions in the bunch crossing of interest were taken into account as well as interactions in the two previous and the following crossing. The latter is important for occupancies in the Outer Tracker, since here two consecutive pipeline cells have to be read out upon a positive trigger decision. Interactions in earlier bunch crossings can contribute to the occupancy due to slow low-momentum particles.

Inner Tracker Occupancies Due to the fine granularity of the silicon microstrip detectors, occupancies in the Inner Tracker are generally low, in spite of the elevated charged particle densities close to the beam pipe. Average and maximum occupancies in each of the stations T1-T3 are summarised in Table 4.1.

Table 4.1: Average (ave) and maximum (max) Inner Tracker occupancies (in %).

station	top/bottom		left/right	
	ave	max	ave	max
T1	0.26	0.41	0.65	1.5
T2	0.23	0.39	0.54	1.3
T3	0.20	0.26	0.51	1.2

Results are given separately for top/bottom boxes and left/right boxes. Maximum occupancies refer to the highest average of any group of 64 consecutive strips. Not surprisingly, in the top/bottom boxes these are the central strips in the middle of the detection layer, whereas in the left/right boxes they are the innermost strips close to the beam pipe.

Outer Tracker Occupancies The layout for the Inner Tracker was conceived in order to avoid occupancies exceeding 10% in the innermost part of the Outer Tracker. As in previous studies, three critical regions of high occupancy in the Outer Tracker were defined (see also the sketch above Table 4.2):

- "top" sector refers to the 96 straws-wide regions above and below the top/bottom boxes of the Inner Tracker;
- "corner" sector refers to the 64 straws-wide regions adjacent to the top/bottom boxes of the Inner Tracker;
- "side" sector refers to 64 straws-wide regions adjacent to the left/right boxes of the Inner Tracker.

Table 4.2 summarises the average occupancies found for each of these three regions, as well as the average over the full Outer Tracker station.

Table 4.2: Outer Tracker occupancies (in %).

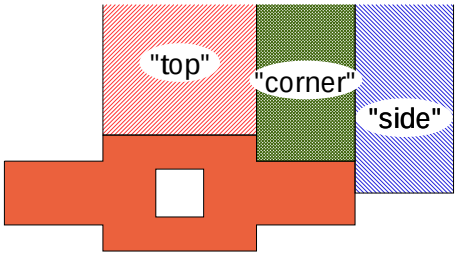

station	average	top	corner	side
T1	4.3	5.4	6.6	6.3
T2	4.0	5.2	6.6	6.2
T3	3.9	5.3	6.7	6.3

These results are lower than those quoted in the Outer Tracker TDR. This is partially due to improvements in simulation and detector description. In addition, the reduction of material in the new LHCb detector layout has reduced charged particle fluxes in the region of T1-T3 by 15-20%.

In conclusion, the study has been demonstrated that the chosen layout and size of the Inner Tracker is adequate. A maximum occupancy of around 7% is found which is comfortably lower than the 10% requirement.

4.3 Momentum Resolution

Charged particle momenta are determined by fitting a five-parameter track model to reconstructed hit coordinates in the Inner Tracker, Outer Tracker and VELO. The track fit [49] employs a Kalman filter technique and takes into account multiple scattering and energy loss in the detector material. In order to speed up the algorithm, a simplified description of the detector geometry is used to calculate the amount of material traversed along the particle trajectory.

The results presented here, were obtained [53] using reconstructed hit coordinates from the detector simulations as input to the fit. As in previous studies [49], hits were assigned to tracks according to the Monte-Carlo particle that caused them. A reference sample of reconstructible tracks was selected based upon the number and position of hits on the generated tracks. These selection criteria are explained in detail in [53]. The most important criteria are that $e^{\pm}$ were excluded from the sample, and that a minimum momentum of $p_{true} > 2\,\mathrm{GeV}/c$ was demanded.

Momentum resolution ($\delta p/p$) was defined as the one standard deviation central width of a double Gaussian fitted to the distribution $(p_{rec} - p_{true})/p_{rec}$, where p_{rec} and p_{true} are the reconstructed and generated particle momenta, respectively. Momentum resolution as function of particle momentum was determined by fitting this distribution in bins of the generated momentum. The contribution of the second Gaussian to the fit was always smaller than 20%.

Momentum resolution as function of momentum is shown in Figure 4.8 for tracks passing through the Inner Tracker. Also shown are the corresponding momentum spectra for all charged particles originating from the pp-interaction region, and for charged pions from the decay $B \to \pi^+\pi^-$, respectively.

The LHCb tracking system is layed out as a dipole spectrometer and it is expected that the momentum resolution as function of momentum can be parametrised as

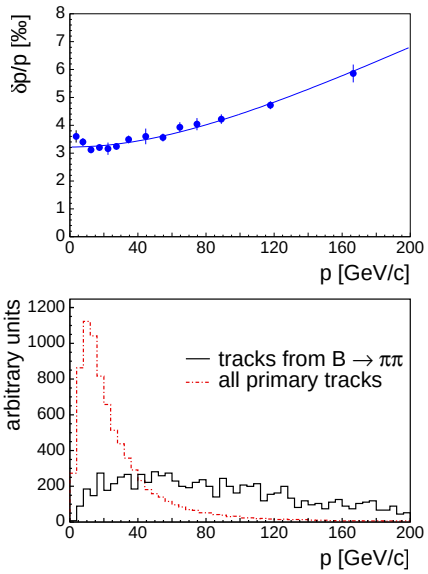

Figure 4.8: Momentum resolution as function of momentum (top) and momentum spectra (bottom) for particles traversing the Inner Tracker.

$$(\delta p/p)^2 = A_{ms}^2 + (\,B_{res} \times p\,)^2, \qquad (4.1)$$

where the first term represents a contribution from multiple scattering and the second term is due to the finite spatial resolution of the detectors.

The superimposed curve in Figure 4.8 shows a fit to this equation for momenta $p > 20\,\mathrm{GeV}/c$. The result of this fit, and of a similar analysis for particles traversing the Outer Tracker, are summarised in Table 4.3.

Table 4.3: Results from fit to equation 4.1, for particles passing through the Inner Tracker and Outer Tracker, respectively.

	A_{ms}	B_{res} [GeV^{-1}]
Inner	3.2×10^{-3}	3.0×10^{-5}
Outer	3.9×10^{-3}	3.6×10^{-5}

From these results, it can be concluded that momentum resolution is dominated by multiple scattering for momenta up to above

100 GeV/c. Furthermore, momentum resolution is in general slightly better for particles passing the Inner Tracker region in T1-T3 than for those passing the Outer Tracker region.

Given these observations, it is not expected that a further improvement of the spatial resolution should have a sizeable influence on momentum resolution. Nevertheless, this influence was investigated explicitly by varying the strip pitch used in the digitisation over a range from 120 μm to 330 μm. Smaller (larger) pitch implies better (worse) spatial resolution.

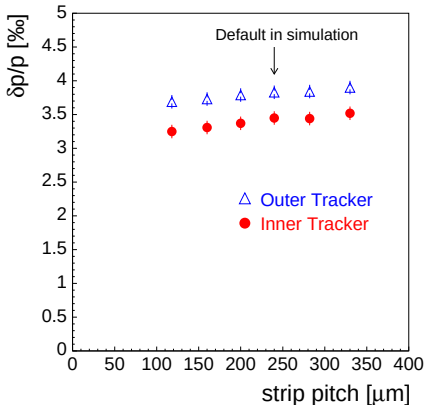

Figure 4.9: Average momentum resolution as function of Inner Tracker strip pitch.

The result of this study is shown in Figure 4.9, where the momentum resolution averaged over all momenta is plotted as function of the strip pitch. Results are shown separately for particles passing the Inner Tracker region and the Outer Tracker region in stations T1-T3.

The results show a small but systematic improvement of momentum resolution with decreasing Inner Tracker pitch. However, the same improvement is observed for tracks passing through the Outer Tracker region in stations T1-T3. Therefore, we conclude that the observed effect is due to the change of spatial resolution in the TT station, where silicon microstrip detectors cover the full acceptance of the experiment. In this study, the strip pitch was always adjusted simultaneously for all four tracking stations (T1-T3 and TT).

In conclusion, strip pitch and spatial resolution in stations T1-T3 are appropriate for the momentum resolution of the LHCb spectrometer.

4.4 Radiation Environment

Expected radiation levels in LHCb have been determined in a FLUKA [50] simulation, using a realistic description of the LHC beam pipe, the LHCb detector and the experiment hall. As part of this program, the Inner Tracker region in tracking stations T1-T3 was investigated in detail. This study is described in [54].

The calculated radiation levels were used to estimate the expected bulk damage and radiation-induced leakage currents in silicon sensors and to determine the operating temperature for the detector.

4.4.1 Radiation Levels

Particle fluences for electrons/positrons, neutrons and charged hadrons, as well as the expected ionizing dose, were determined at the position of each of the Inner Tracker stations. Momentum spectra were determined separately for electrons/positrons, neutrons, pions and other charged hadrons, and the non-ionising energy loss (NIEL) damage in silicon, expressed in the usual units of 1 MeV-neutron equivalent fluence, was estimated by folding the obtained momentum spectra and fluences with damage factors from [55].

Electrons and positrons were tracked down to kinetic energies of 1 MeV, neutrons to 10^{-11} MeV, anti-neutrons to 50 MeV, and photons and other particles to 0.1 MeV. The energy spectra for the different particle species are shown in Figure 4.10.

In the following, results are quoted per primary pp-interaction, and for 10 years of operation at nominal LHCb luminosity of $\mathcal{L} = 2 \times 10^{32}\text{cm}^{-2}\text{s}^{-1}$. With an assumed total inelastic cross section of 80 mb, the pp-interaction rate is 1.6×10^{7} s^{-1} at nominal luminosity.

The quoted results include no safety factors.

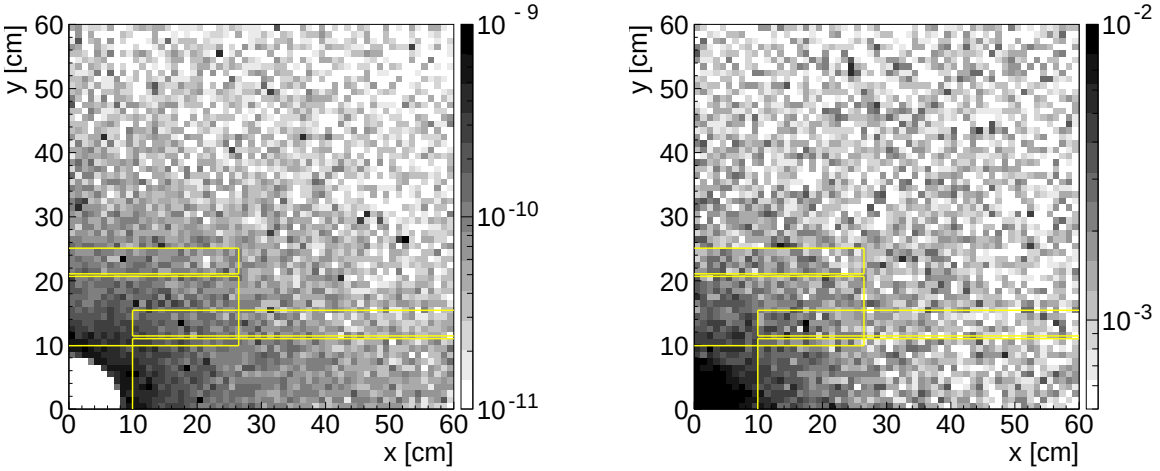

Figure 4.11: Ionizing dose in rad / pp-interaction (left) and 1-MeV neutron equivalent fluence per pp-interaction (right), as function of x and y in one quadrant of T2. Rectangles indicate the area covered by Inner Tracker sensors and front-end electronics.

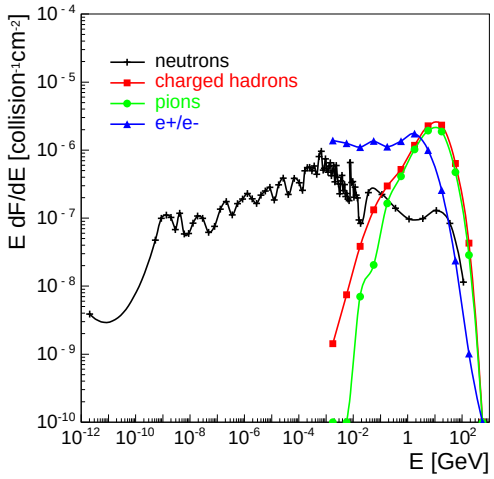

Figure 4.10: Expected particle energy spectra at the location of T1.

Distributions of the expected ionizing dose are shown in the left-hand plots in Figures 4.11 and 4.12. The highest dose is observed in the innermost region of the left/right boxes of station T1, at $x \approx 9\,cm$. Here, an ionizing dose of 6×10^{-10} rad per $\mathrm{p-p}$ interaction is expected, corresponding to approximately 1 Mrad after ten years of operation at nominal luminosity. Similar doses are expected at the location of the front-end electronics on the innermost ladders. At the location of the outermost ladders in the left/right boxes, at $x = 60$ cm, the accumulated ionizing dose after 10 years of operation is not expected to exceed 100 kRad.

The calculated 1-MeV neutron equivalent fluence ϕ_{eq} is shown in the right-hand plots in Figures 4.11 and 4.12. The maximum 1-MeV neutron equivalent fluence in the innermost region of the Inner Tracker amounts to $\phi_{\mathrm{eq}} = 5 \times 10^{-3}\,\mathrm{cm}^{-2}$ per interaction, or $\phi_{\mathrm{eq}} = 9 \times 10^{12}\,\mathrm{cm}^{-2}$ for ten years of operation at nominal luminosity. It is approximately a factor five lower for the outermost ladder at $x = 60$ cm.

4.4.2 Leakage Currents and Operating Temperature

Radiation levels in the Inner Tracker region are moderate and modern silicon detectors are expected to survive ten years of LHCb operation without any problem. However, due to the long readout strips and the large strip pitch employed in the Inner Tracker, each readout strip collects leakage currents from a relatively large volume of the silicon bulk. Shot noise due to leakage currents can therefore become sizeable after several years of operation, if the sensors are not adequately cooled.

Significant noise contributions from shot noise are, however, not acceptable since the S/N performance of the 22 cm long silicon ladders is limited to values of approximately

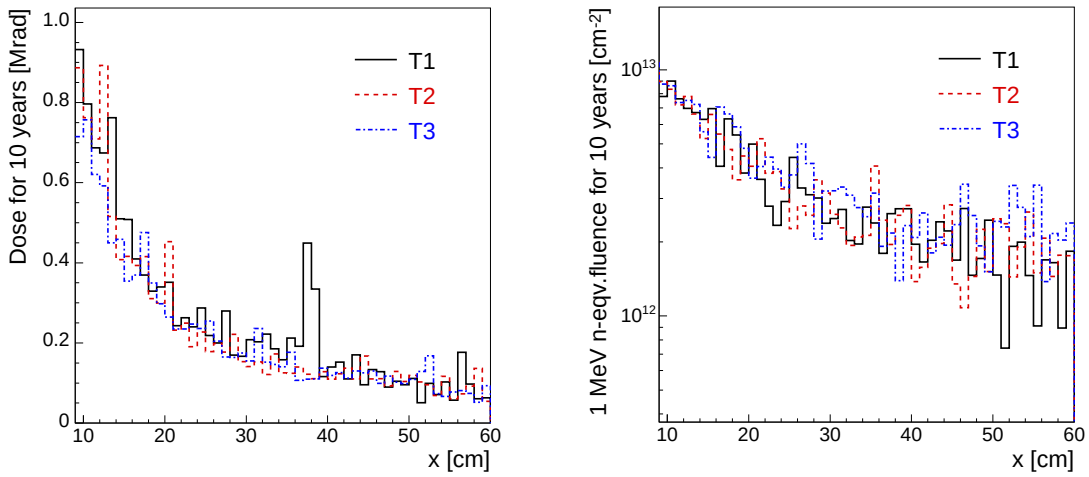

Figure 4.12: Ionizing dose (left) and 1-MeV neutron equivalent fluence in T1-T3, for ten years of operation at nominal luminosity, as function of x averaged over $0 < y < 5\,\text{cm}$ (right).

twelve by Johnson noise from the large input capacitances seen by the preamplifier (see sections 3.1 and 3.2). S/N values in excess of ten are required in order to guarantee full efficiency of the detector [29].

In order to ensure an efficient and reliable operation over the full lifetime of the detector, the operating temperature of the silicon sensors should thus be chosen such that shot noise from leakage currents does not deteriorate the total noise by more than approximately 10%. This requirement translates to an equivalent noise charge of less than $900\,\text{e}^-$.

The equivalent noise charge due to shot noise is given by [56]

$$\text{ENC} = \sqrt{12 \cdot I_{\text{leak}}[\text{nA}] \cdot \tau[\text{ns}]}\ ,$$

where τ is the shaping time of the preamplifier, taken as the FWHM of the signal shape. For a typical shaping time of 35 ns foreseen for the Inner Tracker, a shot noise of $900\,\text{e}^-$ thus corresponds to a leakage current of less than $2\,\mu\text{A}$.

Radiation induced leakage currents at room temperature are described by

$$I_{\text{leak}} = \alpha \cdot V \cdot \phi_{\text{eq}},$$

where V is the bulk volume from which each strip collects leakage current and $\alpha = 3 \times 10^{-17}\,\text{A/cm}$ is the radiation damage coefficient.

The highest leakage currents are expected for the 22 cm long strips in the innermost regions of the side boxes. With a strip pitch of approximately $200\,\mu\text{m}$ and a bulk thickness of $320\,\mu\text{m}$, $V = 0.0141\,\text{cm}^3$. Applying a safety factor of two on the radiation levels calculated above, $\phi_{\text{eq}} = 1.8 \times 10^{13}\,\text{cm}^{-2}$ for the innermost ladders after 10 years of operation, and a leakage current of $I_{\text{leak}} = 6.8\,\mu\text{A}$ is expected at room temperature.

However, leakage currents decrease with the temperature of the silicon bulk as

$$\frac{I_2}{I_1} = \left(\frac{T_2}{T_1}\right)^2 \cdot \exp\left(\frac{E_g(T_2 - T_1)}{2kT_2T_1}\right)$$

where $E_g = 1.2\,\text{eV}$ is the gap energy for silicon, and $k = 8.6 \times 10^{-5}\,\text{eV/K}$ is the Boltzmann constant. With this, one can easily calculate that leakage currents below the required $2\,\mu\text{A}$ can be obtained if the silicon sensors are operated at temperatures of 5°C or lower.

In conclusion, at the radiation levels expected in the Inner Tracker area, radiation damage is no major concern and silicon sensors are expected to survive ten years of LHCb operation. Radiation hard front-end electronics are, however, required. Silicon sensors should be operated at a temperature of 5°C or lower,

in order to ensure low shot noise after ten years
of operation.

Chapter 5

Detector Design

The technical design of the Inner Tracker is based as much as possible upon the experience gained in the R&D and prototyping described in Chapter 3.

In the following sections, certain repetitions in the description of components are thus unavoidable, although an effort was made to keep them to a minimum and to refer to previous sections wherever possible.

Design parameters of the Inner Tracker silicon sensors are summarised in Section 5.1. Ladder mechanics and a ladder assembly procedure are described in Section 5.2, followed by a description of the detector box and station mechanics in Section 5.3. Sections 5.4, 5.5 and 5.6 give a technical description of Level-0 electronics, readout link, and Level-1 electronics, respectively. An overview of detector infrastructure — cooling system, power distribution and grounding scheme — is given in Section 5.7. Finally, safety aspects are discussed in Section 5.8.

5.1 Silicon Sensors

A total of 504 identical silicon sensors are used to construct the Inner Tracker stations T1-T3. The design of these sensors will be very similar to that of the HPK prototype sensors described in Section 3.1, except that a unique strip geometry will be used for all strips. The test-beam program described in Section 3.3 has demonstrated that in regions of 237.5 μm strip pitch, a significant charge loss occured in the inter-strip region and that this charge loss was suppressed in the regions of the smaller pitch of 198 μm. Given the requirements on shaping time and strip length, the detectors have to cope with significant preamplifier noise and the observed charge loss leads to unacceptable efficiency losses. It was therefore decided that the final detector will use a strip pitch of 198 μm with 384 strips per sensor. Since no clear difference in the behaviour was observed for the regions of different w/p, the decision on the implant width will be delayed until after further beam tests with the Beetle 1.2 readout chip.

Further technology and geometry specifications of the sensors were given in Tables 3.1 and 3.3.

For bonding and probing, the sensor design incorporates two AC pads and one DC pad at each end of each readout strip, as well as two strip bias pads and two backplane bias pads in each corner of the sensor. To simplify handling and ladder assembly, the backplane bias pads are located on the strip side of the sensor and connected to the backplane by a via through the silicon bulk.

The backplane of the sensors will be passivated in order to provide electrical insulation from the electrically conductive ladder support.

Furthermore, alignment targets are located in each corner of the sensor. During ladder assembly, these targets will be used to verify the correct positioning of the sensors with respect to alignment features on the ladder support.

Finally, the sensors carry a consecutive strip numbering at both ends of the strips and a unique serial number for each sensor. This will allow each sensor and strip to be identified and

traced during testing and assembly.

All these features, with the exception of the backplane passivation, were already implemented in the HPK prototype sensors.

5.2 Silicon Ladders

The layout of the silicon ladders has been described in Section 2.3. Two types of ladders are employed, that are built from one silicon sensor or two sensors, respectively. Except for the overall length of the carbon fibre support shelf, the design of the two ladder types is identical. In total, 168 one-sensor ladders and 168 two-sensor ladders are used in stations T1-T3.

In this section, the design of the individual components — supports, balconies, pitch adaptor and hybrid — will be explained and the ladder assembly procedure will be described.

5.2.1 Ladder Supports

The silicon sensors are mounted onto a U-shaped carbon fibre support shelf that has a two-fold functionality: it provides mechanical rigidity to the ladder and it helps to cool the silicon sensors and reduce the ambient temperature inside the detector box.

The backplane of the silicon sensors is passivated in order to electrically insulate it from the carbon support shelf. If necessary, additional insulation can be provided by inserting a thin kapton foil in between the support shelf and the sensors. Several glues are being considered for fixing the silicon sensors. The final choice will be made after further prototype tests.

The support shelf will be produced as a multi-layer structure from thin sheets of a unidirectional carbon fibre composite, using high-tensile fibres with high thermal conductivity. The overall thickness of the structure will be of the order of 350-400 μm. The final material choice has not yet been made. The Amoco K1100 carbon-fibre used for the prototype shelf described in Section 3.4 showed acceptable thermal properties but is rather expensive. An alternative could be provided by the K13D2U carbon fibre by Mitsubishi.

A technical drawing of the end section of a support shelf, where the balcony and hybrid are located, was shown in Figure 3.42.

The shelf is 80 mm wide in order to accommodate the 78 mm wide silicon sensors. Two 2 mm high wings along the long sides of the support give mechanical strength to the support and provide some protection during handling of the assembled ladder. A 46 mm wide and 30 mm high cutout allows to mount the readout hybrid directly onto the balcony, thus avoiding direct thermal between hybrid and carbon fibre support. Two little aluminium inserts to both sides of the hybrid area allow the precision machining of alignment and fixation holes that will be used to position the support shelf on the balcony with a precision of better than 5 μm. These alignment holes are also used as a reference during the ladder assembly for the accurate positioning of the silicon sensors onto the support.

Additional cutouts in the support shelf are foreseen underneath the silicon sensors. The sole purpose of these cutouts is to minimise the material budget of the detector and their exact size will be fixed based upon studies of mechanical and thermal properties using the final support shelf material.

5.2.2 Balconies

The balcony provides the mechanical and thermal interface of the ladder to the cooling plate. It contains alignment features to precisely position the ladder and it acts as a heat sink for the front-end hybrid. Three types of balconies will be produced for the three different stereo views. A technical drawing of a balcony for a ladder in an x-detection layer was shown in Figure 3.45. Balconies for the u and v stereo layers are similar, except that alignment and fixation holes for the carbon fibre shelf and front-end hybrid will be shifted according to the different angle of inclination of the ladder. Two material candidates for the balconies

have been identified: a metal-matrix composite of magnesium-infiltrated carbon fibre and a high-density graphitic foam encapsulated with an epoxy resin. The choice of the final material will be based upon further studies of the mechanical and thermal properties of these two materials. In parallel, design studies are ongoing in order to further reduce the material budget.

5.2.3 Pitch Adaptor and Hybrid

The pitch adaptor and the readout hybrid will be produced as two separate pieces. The pitch adaptor has to provide the interface between the 198 μm strip pitch of the silicon sensors and the input pitch of the Beetle readout chip, which is 40.24 μm. It will be produced in single-layer thin film process on a 500 μm thick Al_2O_3 substrate. It has the same width as the silicon sensors and is 11 mm long. It will be glued directly onto the ladder support shelf.

The front-end hybrid will be produced in the same technique and have a similar layout as the prototype hybrid described in Section 3.2. The central part of the kapton hybrid will be glued onto a 400 μm thick support of AlN or a similar material, that provides mechanical stiffness for bonding and provides good thermal contact to the balcony. The dimensions of this support will be 45 mm $\times$ 29 mm such that it fits into the cutout in the ladder support shelf.

5.2.4 Ladder Assembly

The ladder assembly procedure should be fast, simple and robust, and must ensure a sufficiently precise positioning of the silicon sensors. A detailed analysis of alignment tolerances is described in [57]. It shows that silicon sensors (i.e. the readout strips) should be positioned with an accuracy of better than 10 μm RMS with respect to the alignment holes on the balcony. Overall sensor misalignment will then not contribute more than 10% to the resolution of the detector.

A ladder assembly procedure has been developed that exploits the measured, excellent accuracy of the dicing edge of the sensors to obtain this alignment precision. The procedure is described in detail in [58]. Similar procedures have been employed successfully by other experiments, for example by GLAST for the large BTEM prototype detector [59].

A sketch of the tooling is shown in Figure 5.1. It consists of a positioning jig for the carbon fibre support shelf, a positioning jig for the silicon sensors, and a transfer jig. The positioning jigs are equipped with alignment fixtures that allow to accurately position the support shelf and the sensors, respectively. In addition, both positioning jigs are equipped with precision dowel pins that fit into precision feedthroughs in the transfer jig. This allows to transfer the silicon sensors from their positioning jig to the carbon fibre support shelf in an accurate and reproducible way.

Silicon sensors are placed on their positioning jig and pushed against alignment pins on the jig. This is where the accuracy of the dicing edge is exploited in order to accurately position the sensors. Vacuum suction is then applied to hold the sensors in position. The transfer jig is placed on top of the sensors, vacuum suction is applied in the transfer jig and switched off in the positioning jig. In the meantime, the bare carbon fibre support shelf is positioned in its jig. This jig contains alignment pins that fit into the same alignment holes on the support shelf that will later determine its position on the balcony. Glue is applied using a glue dispenser. Next, the transfer jig with the silicon sensors is placed on top of the prepared carbon fibre support shelf. The vacuum in the transfer jig is left on until the glue is cured and the silicon sensors are reliably positioned on the carbon fibre support shelf.

Since the tooling is simple and cheap to produce, several jigs can easily be employed in parallel in order to speed up ladder production.

The pitch adaptor is mounted onto the support shelf using similar tooling and a similar procedure. Once the glue is cured, the ladder support is mounted onto the balcony. A thin layer of a thermally conductive paste will be

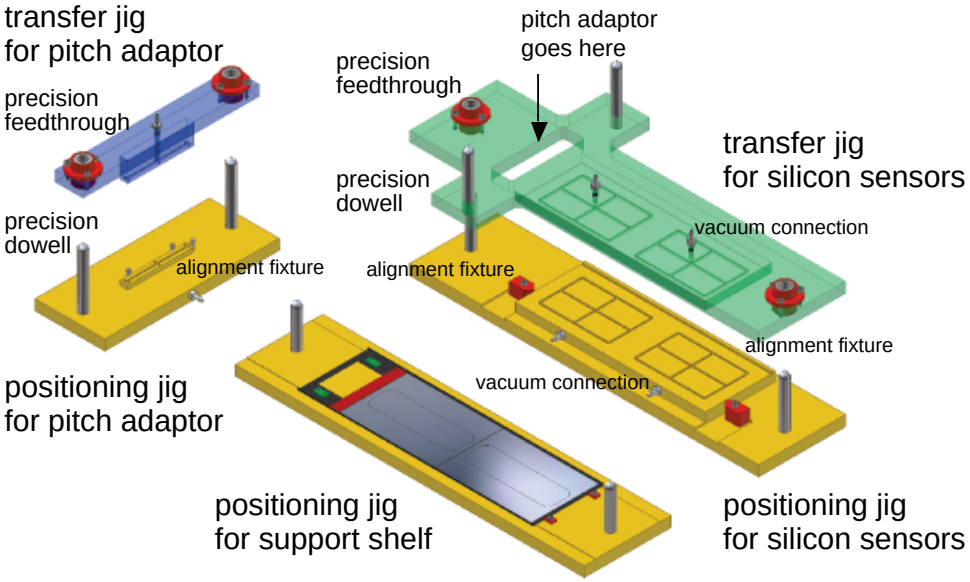

Figure 5.1: Sketch of the ladder assembly tooling.

applied in between balcony and the support shelf in order to ensure good thermal contact. Finally, a fully assembled and tested hybrid will be mounted onto the balcony, and the ladder is ready for bonding. Three rows of 388 bonds each are necessary to complete a two-sensor ladder: one row between the second and the first sensors, a second row between the first sensor and the pitch adaptor, and a third row between pitch adaptor and Beetle readout chip (respectively hybrid for the bias voltage and return lines).

5.3 Station Mechanics

The layout of the detector box has been described in Section 2.2, a technical drawing of the box is shown in Figure 5.2. A detector box consists of 28 silicon ladders, arranged in four detection layers. The ladders are mounted onto a common cooling plate that provides alignment features and acts as heat sink for front-end chips and silicon sensors. The cooling plate is mounted onto a stiff honeycomb cover plate that provides mechanical rigidity to the detector box. This cover plate integrates a patch panel to which the kapton tails of the front-end hybrids connect, and it contains feedthroughs for all cables and the cooling pipes. The design of the feedthroughs is greatly simplified by an additional insulation layer that separates the cover plate from the cold part of the box volume. The detector box slides into a light-tight enclosure that also provides thermal and electrical insulation.

Silicon ladders within a detection layer are pairwise staggered in z, as shown in Figure 5.3, such that silicon sensors on adjacent ladders overlap by 2.5 mm in x. The z distance between the silicon sensors on staggered ladders can be kept as small as 1.5 mm by swapping the orientation of adjacent ladders, i.e. the strip sides of the silicon sensors alternately face upstream, respectively downstream. The dimensions given in the figure refer to the width of the readout hybrid (45 mm), balcony (66 mm), silicon sensors (78 mm) and support shelf (80.8 mm).

The distance between the central planes of two consecutive detection layers is approximately 13 mm. The outer dimensions of the detector box are 578 mm wide $\times$ 385 mm high $\times$ 74 mm thick. The distance between detection layers and the overall thickness of the box are mainly determined by the design of the cooling plate. They may need to be adjusted

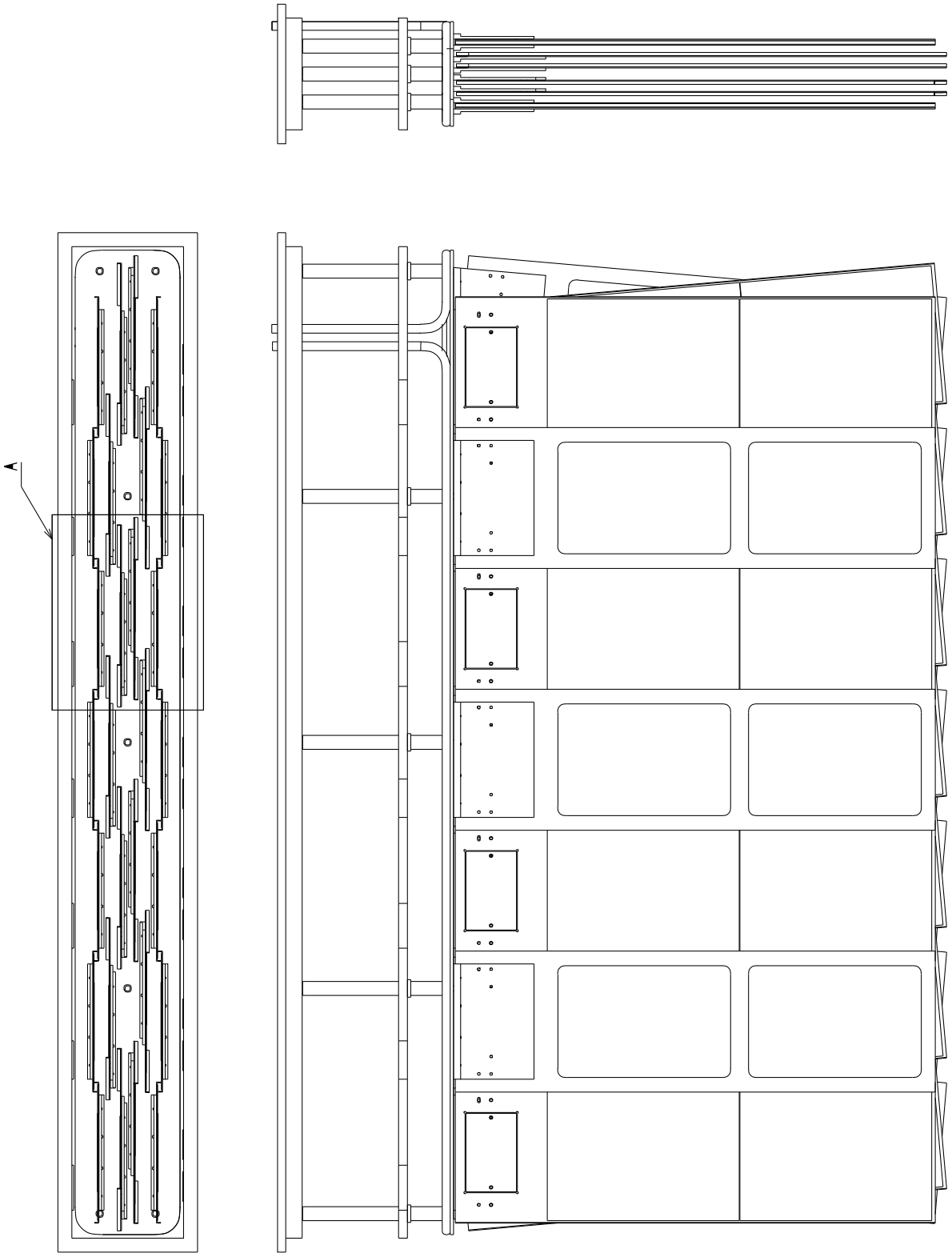

Figure 5.2: Technical drawing of detector box.

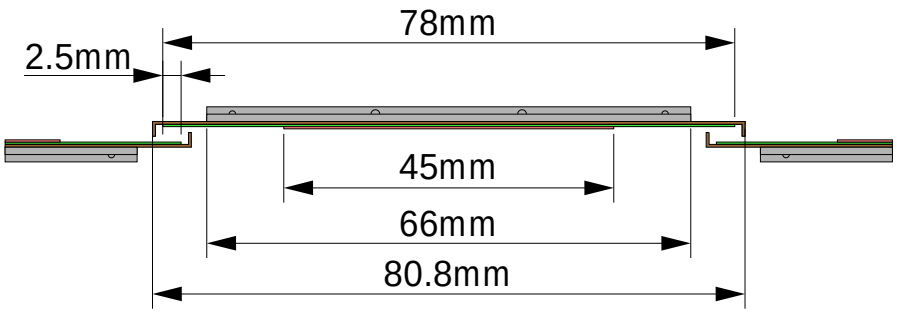

Figure 5.3: Detail of a detection layer, showing the overlap between adjacent silicon ladders. Adjacent ladders are staggered such that silicon sensors overlap by 2.5 mm.

slightly if the design of the cooling plate is revised, as discussed below.

The estimated total mass for one detector box is 1.5 kg, excluding external cables.

The detector boxes are mounted onto a support structure that connects to the outer frames of the tracking station. To simplify installation and maintenance of the detector boxes, the support structure for each station consists of two parts that can be retracted horizontally from the beam pipe.

5.3.1 Cooling Plate

In order to ensure the accurate positioning of the silicon ladders, the cooling plate must contain precisely machined alignment features, its surface flatness must be excellent and the overall bending of the plate under the load of the attached silicon ladders should not exceed 50 μm [57]. The thermal impedance of the plate has to be small in order to ensure efficient heat transfer from the silicon ladders to the coolant.

A realistic design of the cooling plate was shown in Figure 3.34. It includes all necessary alignment and fixation features for the 28 balconies, as well as the slits that allow routing the kapton tails from the front-end hybrids to the patch panel on the cover plate.

The plate is kept cold by an integrated aluminium cooling pipe with an outer diameter of 5 mm, in which liquid C_6F_{14} at -15°C is circulated in the turbulent regime. The cooling plate is mounted onto the cover plate on seven support rods. A finite element analysis has indicated that the overall bending of the plate can be expected to be smaller than 20 μm.

However, the prototype tests described in Section 3.4 have shown that the current design results in a rather large temperature drop across the plate. Modifications to the design are therefore being investigated with the aim to reduce thermal impedances. These investigations concentrate mainly on an improved routing of the cooling pipe in order to reduce the distance between cooling pipe and balconies.

Two material candidates for the cooling plate have been identified: a metal-matrix composite of magnesium-infiltrated carbon fibre and a Carbon-Carbon composite. The final choice of the material will be made after further studies of their respective mechanical and thermal properties.

5.3.2 Box Enclosure

The box enclosure has to be light-tight and must provide thermal and electrical insulation. The side walls of the box should be as thin as possible in order to minimise the distance between beam pipe and sensitive detector elements. The enclosure should be rigid enough to provide mechanical protection of the fragile silicon detectors during handling of the detector box.

The prototype box enclosure described in Section 3.4 fulfils all these requirements and the final box enclosure will be very similar.

It will be assembled from thin sheets of PIR foam that are bonded together using a special one-component PUR adhesive. Sheets of 6 mm thickness will be employed for the front and back faces of the box whereas 3 mm thick sheets will be used for the side walls facing the beam pipe. The sheets are clad on both sides with a 100 μm thick Kevlar tape and a 25 μm thin aluminium foil that improve mechanical stability and provide a vapour barrier and electrical insulation.

5.3.3 Detector Box Assembly

The modular design of the detector box provides for a simple and fast assembly procedure. The cooling plate is mounted onto the cover plate. Fully tested and debugged silicon ladders are then mounted onto the cooling plate and the kapton tails are connected to the patch panel. After the assembly of each detection layer, the position of all silicon sensors will be measured with respect to two "ruby ball" alignment references on the cooling plate. When all four detection layers have been assembled, the box enclosure is slid over the detectors and connected to the cover plate. The detector box is ready for testing.

5.3.4 Support Frame

The overall design of tracking station frames is currently undergoing a major revision. In the Outer Tracker TDR [2], a design was presented in which all tracking stations downstream of the magnet were mounted onto a common support structure. Instead, it is now foreseen that stations are individually suspended from separate support rails and can be retracted independently. This will greatly simplify access to the Inner Tracker detector boxes for installation and maintenance work.

The four detector boxes within a station will be mounted onto a light-weight support structure that is fixed to rails on the outer frames of the tracking station. For installation and maintenance, this support structure consists of two parts that can be retracted horizontally from the beam pipe. Inner Tracker and Outer Tracker detectors will be suspended from separate rails. This will permit independent movements for maintenance of Inner and Outer Trackers. A front view of a tracking station in closed position (for data taking) and open position (for installation and maintenance) is shown in Figure 5.4.

Frame mechanics will guarantee a reproducibility of positioning of better than 1 mm in x and y. Stops on the support rails will guarantee that the Inner Tracker boxes can never be moved against the beam pipe. In addition, access to the region close to the beam pipe will always be possible whilst the Inner Tracker is moved into data-taking position. It can therefore be ensured that the clearance to the beam pipe is always maintained.

Cables and support lines for the detector boxes will be preferably routed along the support structure to the top or bottom frame of the station, as this provides the shortest path across the sensitive region of the Outer Tracker. A possible location for the service boxes is indicated by the hatched rectangles in Figure 5.4. The detailed cable routing will take into account results from simulation studies in order to minimise the effect of material on tracking performance.

5.4 Level-0 Electronics

The term "Level-0 electronics" refers to the part of the read-out electronics that deals with the detector data up to the Level-0 trigger decision. In the case of the Inner Tracker, this is the Beetle front-end chip. Three Beetle chips are mounted onto a front-end hybrid to read out each silicon ladder.

5.4.1 Beetle Chip

The Beetle chip is a custom development for the LHCb Inner Tracker, VELO, pile-up veto and, possibly, RICH detectors. Its design history and R&D on the latest versions of the Beetle chip have been described in Section 3.2. Its

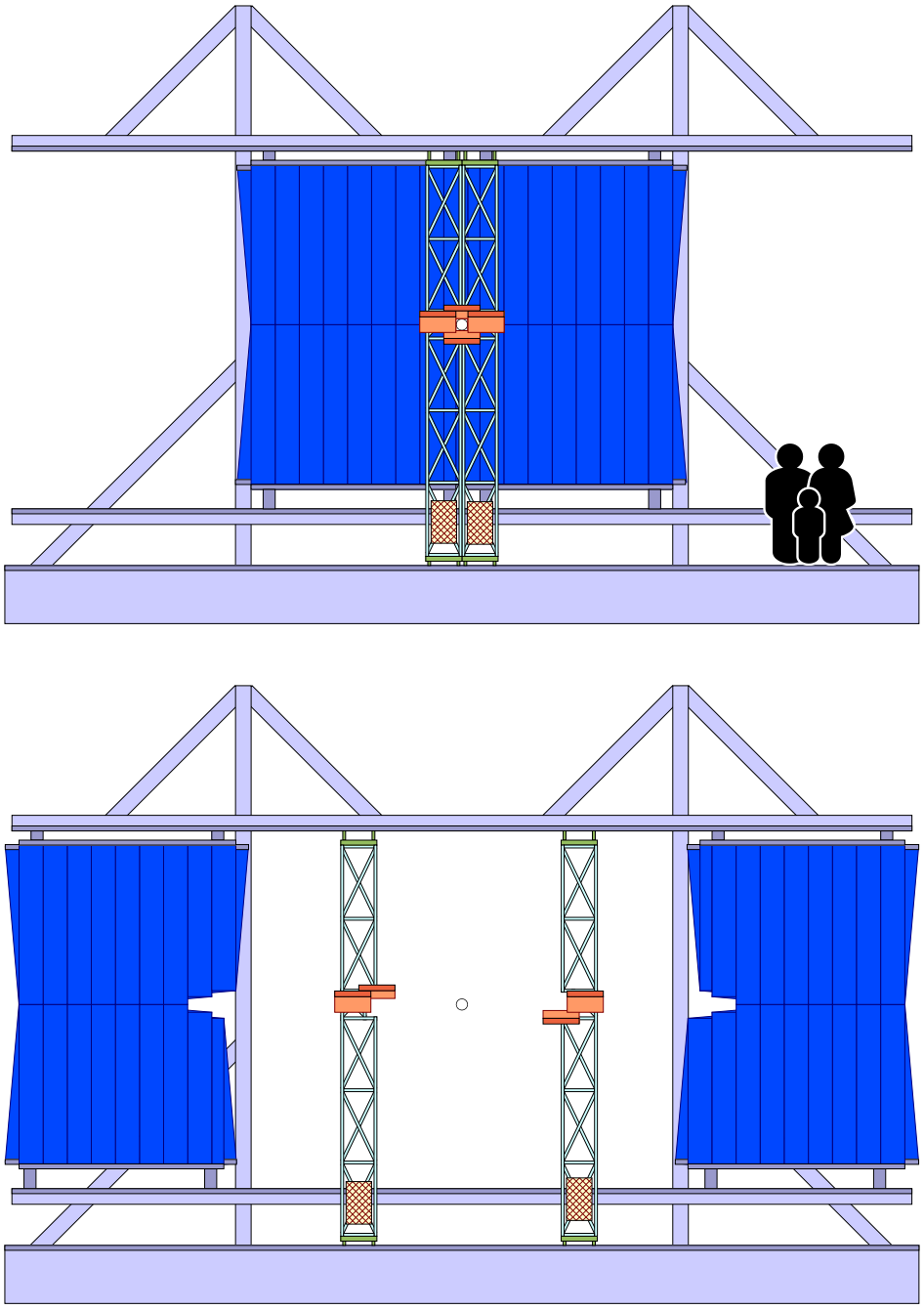

Figure 5.4: Sketch of station in closed (top) and open (bottom) position.

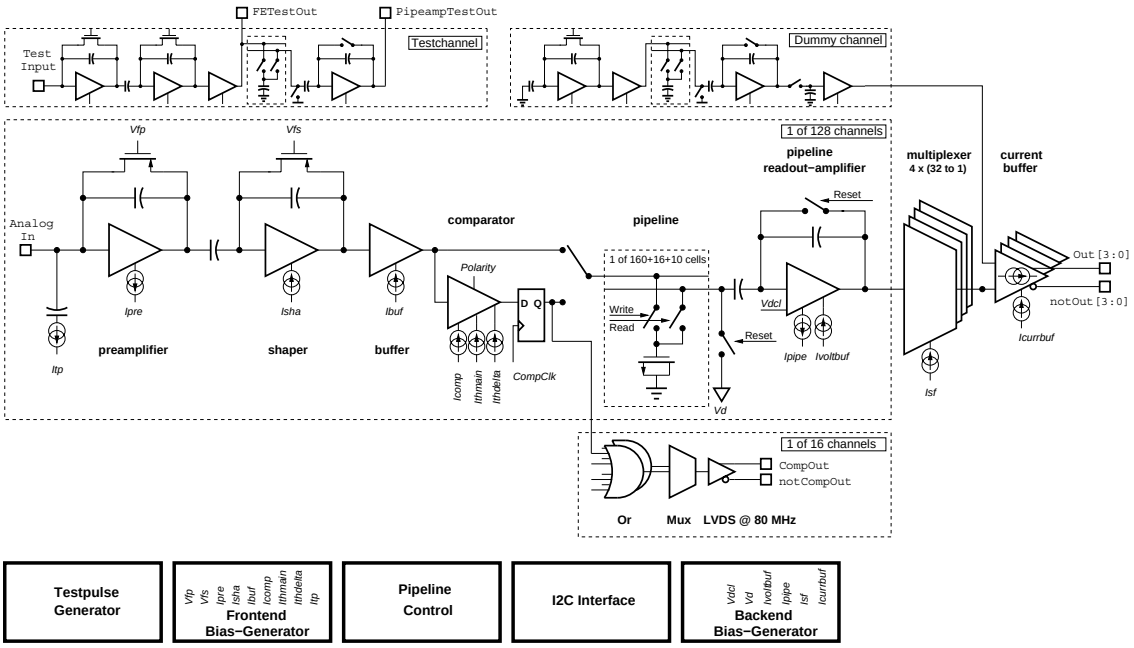

Figure 5.5: Block diagram of the Beetle chip.

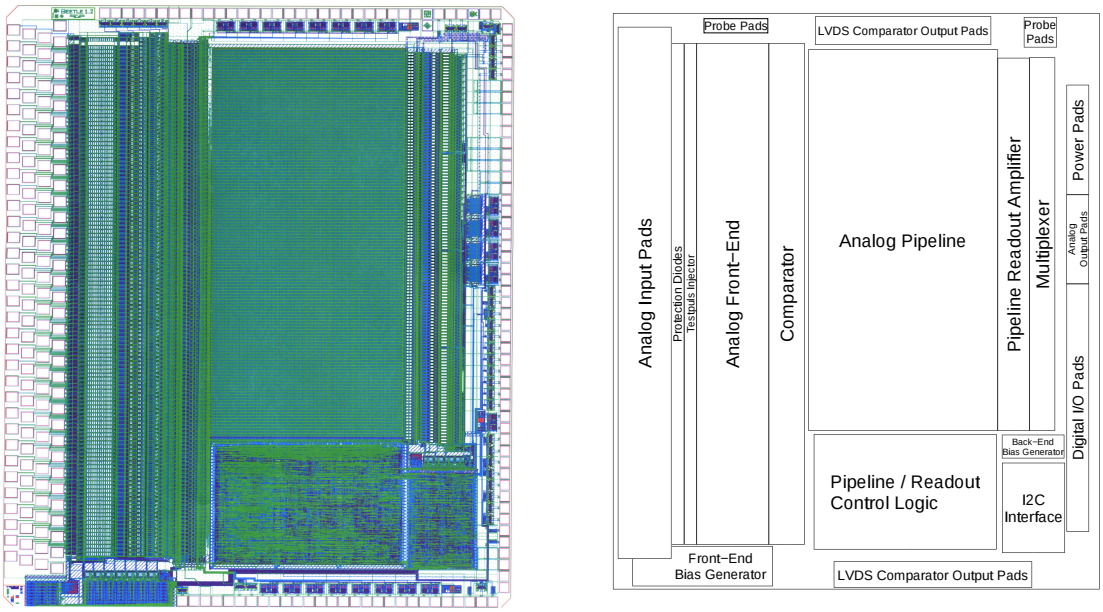

Figure 5.6: Beetle 1.2 layout and floor plan.

specifications are described in detail in [13] [1].

The chip is implemented in radiation-hard 0.25 μm CMOS technology and uses an SEU immune design for logic circuits and configuration registers. It follows the basic RD20 front-end electronics architecture [23]. A block diagram of the chip is shown in Figure 5.5, the layout and floor plan of the latest version of the chip, the Beetle 1.2, in Figure 5.6. The input pads have a pitch of 40.24 μm and the die size is 6.1 mm $\times$ 5.5 mm.

The Beetle integrates 128 read-out channels with low-noise charge sensitive preamplifiers and active CR-RC shapers. The shaping time of the front-end has been optimised to avoid large signal spill-over at the LHC bunch crossing frequency of 25 ns and to deal with the large input capacitances of the long Inner Tracker silicon ladders. Each channel incorporates a comparator that provides a binary signal. However, this feature of the chip is not used in the Inner Tracker. Instead, the output of the shaper is sampled with the LHC bunch-crossing frequency of 40 MHz into an analog pipeline with a programmable latency of up to 160 sampling intervals and a 16-cell deep derandomising buffer. The length of the pipeline is matched to the fixed latency of 4 μs of the LHCb Level-0 trigger.

Event data accepted by the Level-0 trigger are multiplexed with 40 MHz into four output ports. This design permits read out of a full data cycle within 900 ns and to accept trigger rates of up to 1 MHz with a dead time of less than 1%. The output of a dummy channel is subtracted from the analog data in order to compensate common-mode effects. Fully differential current drivers bring the serialised data off the chip.

A charge injector with adjustable pulse height is implemented for testing and calibration purposes. Bias settings and other operation parameters are controlled via a standard I^2C interface [60]. All digital control signals, except those for the I^2C ports, are routed via LVDS ports.

The overall power consumption of the Beetle has been measured to be 4 mW per channel, corresponding to approximately 0.5 W per chip.

[1] The output pad layout described in [13] refers to the Beetle 1.1. It has been modified for the latest version of the chip, the Beetle 1.2.

5.4.2 Front-End Hybrid

The front-end hybrid carries three Beetle chips to match the 384 read-out strips of the Inner Tracker silicon ladders. The technology and design of the hybrid will be very similar to the prototype hybrid described in Section 3.2.

Some modifications of the layout of traces are necessary since the output pad assignment on the Beetle chip has been changed from version 1.1 to version 1.2 of the chip. In addition, some of the discrete passive SMD components will be replaced by array-like versions in order to reduce the number of components and material budget.

5.4.3 TFC and ECS Interfaces

The Level-0 electronics interfaces to the trigger and fast control (TFC) system and to the experiment control system (ECS) are located in the service box on the outer frames of the tracking station. The readout related functionality of the service box is described in section 5.5 below. The TFC interface is provided by a TTCrx chip, the interface to the ECS by a SPECS slave unit. Both are LHCb standard solutions [43]. Integration into the TFC, ECS and data acquisition environment will be done in close collaboration with other LHCb groups.

5.5 Readout Link

Data from the Inner Tracker have to be transmitted over a distance of approximately 100 m from the detector boxes to the L1 electronics in the LHCb electronics hut. Considerations of system robustness and of data integrity at the high transmission rates required by LHCb have led to the decision to use digital optical links.

In addition, the development and commercialisation of highly integrated optical components over the past years has resulted in significant cost reductions and a wide availability of commercial digital optical components. In particular, the development of 12-fibre parallel optical links by several companies has led to several multi-source agreements and the definition of common standards. These developments were exploited to design a simple, modular and cost efficient digital optical readout link.

In order to minimise the number of components inside the acceptance of the experiment, digitisation of the data and electrical to optical conversion will not be performed directly on the detector box but in a so-called service box that is located on the outer frames of the tracking station. An additional advantage of this layout are significantly relaxed requirements on power consumption and radiation tolerance of the employed components.

Nevertheless, all components located in the service box have to be radiation qualified. Simulation studies of radiation levels in LHCb, described in Section 4.4, have shown that an ionizing dose of the order of 5 kRad and a fluence of hadrons above 20 MeV of $5 \times 10^{11}/\mathrm{cm}^2$ can be expected at the location of the outer station frames after ten years of operation at nominal luminosity. These values do not include safety factors.

5.5.1 Link Design

A block diagram of the readout link was shown in Figure 2.10.

At a Level-0 trigger accept rate of 1 MHz, each output port of the Beetle front-end chip transmits the multiplexed analog data from 32 readout strips at a rate of 40 MHz. The fully differential Beetle output signals will be directly transmitted via approximately 5 m long multichannel shielded fine-pitch twisted pair cables to the service box, where they will be digitised in an 8 bit FADC.

The Analog Devices AD9042 chip is a viable candidate for the FADC, since it has been radiation qualified for ionizing doses of up to 2 Mrad [61]. However, the AD9042 provides a resolution of 12 bit, out of which only 8 bit would be used. The power consumption of the chip is high and it is rather expensive. In view of the low radiation dose that is expected at the location of the service box, alternative FADC solutions are under investigation.

The 8 bit digitised data from four Beetle output ports will then be serialised in one CERN GOL [16] chip. The outputs from twelve GOLs, corresponding to the data from four silicon ladders, are fed into one parallel optical transmitter that contains twelve VCSEL laser diodes and interfaces directly to a commercial 12-fibre parallel optical cable.

Parallel optical transmitter modules are commercially available from several producers. These devices may turn out to be sensitive to SEU effects, since they contain an internal factory-programmed flash memory to store bias settings for the laser drivers. An irradiation test is planned for the spring of 2003. In the meantime, backup solutions are prepared using the internal GOL laser driving circuitry to directly drive either commercially available 12-VCSEL diode arrays or twelve single VCSEL diodes with single-fibre interfaces. In the latter case, a so-called breakout cable would be used to join twelve single fibres to a 12-fibre ribbon cable.

The data receiver is located on a mezzanine card on the Level-1 electronics board. A parallel optical receiver, similar to the transmitter, receives input from twelve fibres and performs the conversion from optical to electrical signals. A commercial Texas Instruments TLK2501 16:1 demultiplexer is used to deserialise each data stream to 16 bits at a clock speed of 80 MHz. The second stage of demultiplexing, from 16 bit at 80 MHz to 32 bit at 40 MHz, can be performed in the synchronisation FPGA on the Level-1 electronics board.

5.5.2 Service Box

Associated to each detector box is a service box that is located on the outer frames of the

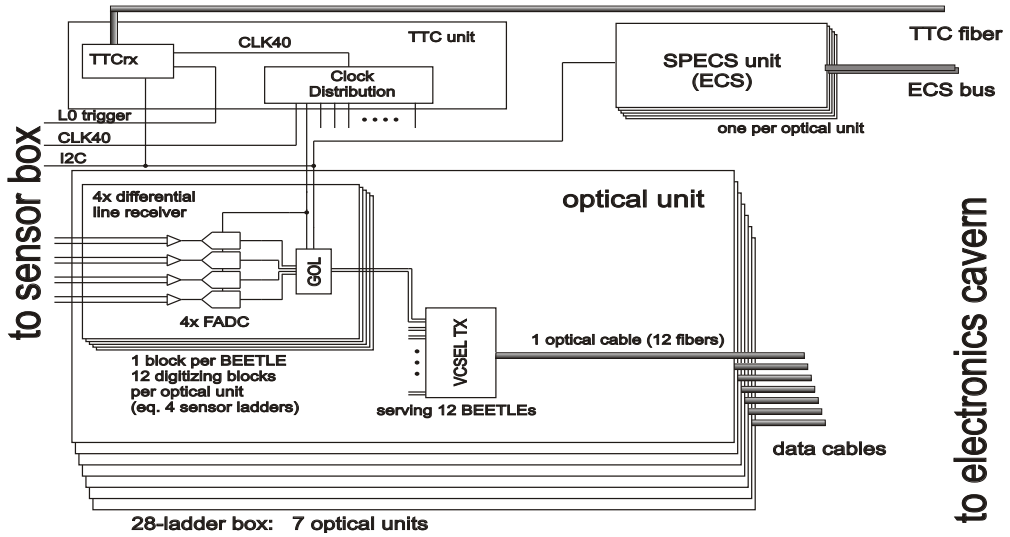

Figure 5.7: Block diagram of the readout related functionality of the service box.

tracking station, outside of the acceptance of the experiment.

The service box fulfils a multiple functionality. As described above, digitisation of data and electrical to optical conversion are performed here. In addition, the box contains the low-voltage and high-voltage power distribution for front-end electronics and silicon sensors. This second part of the functionality of the box will be described in Section 5.7. Finally, the interfaces to the timing and fast control system (TFC) and to the experiment control system (ECS) are located here.

A block diagram of the readout related functionality of the service box is shown in Figure 5.7. Each service box receives and transmits data from 28 silicon ladders and connects to seven 12-fibre optical cables. Digitisation, serialisation and optical transmission are implemented in seven identical optical blocks, each of which is associated to one 12-fibre optical cable. It consists of twelve digitising blocks and a VCSEL transmitter. Each digitising block consists of four differential receivers, four FADC chips and one GOL chip and processes the data from one Beetle chip.

The TFC interface uses a TTCrx chip to receive timing and control signals via optical fibre, and contains a clock distribution system for Beetle, FADC and GOL chips.

The ECS interface is provided by a SPECS slave unit [43]. It is connected via the ECS bus to the ECS master located in the control room, and provides standard I^2C interfaces to the GOL chips and Beetle front-end chips as well as interfaces to temperature monitors in the detector box.

The total power consumption of the readout link components is estimated to be 250 W if the AD9042 FADC chip is used. This value can be significantly lower for alternative FADC solutions.

In addition, a power dissipation of approximately 200 W can be expected from the linear low-voltage power regulators. The overall power dissipation per service box can thus be of the order of 450-500 W and water cooling is mandatory.

5.6 Level-1 Electronics

The functionality of the Level-1 electronics has been described in Section 3.6 and is similar to that of the Level-1 electronics for the VELO [14]. It will be implemented in a common digital readout board that is being developed for the Inner Tracker, the VELO and the Outer Tracker [62]. A draft layout of the board is shown in Figure 5.8. It consists of a common

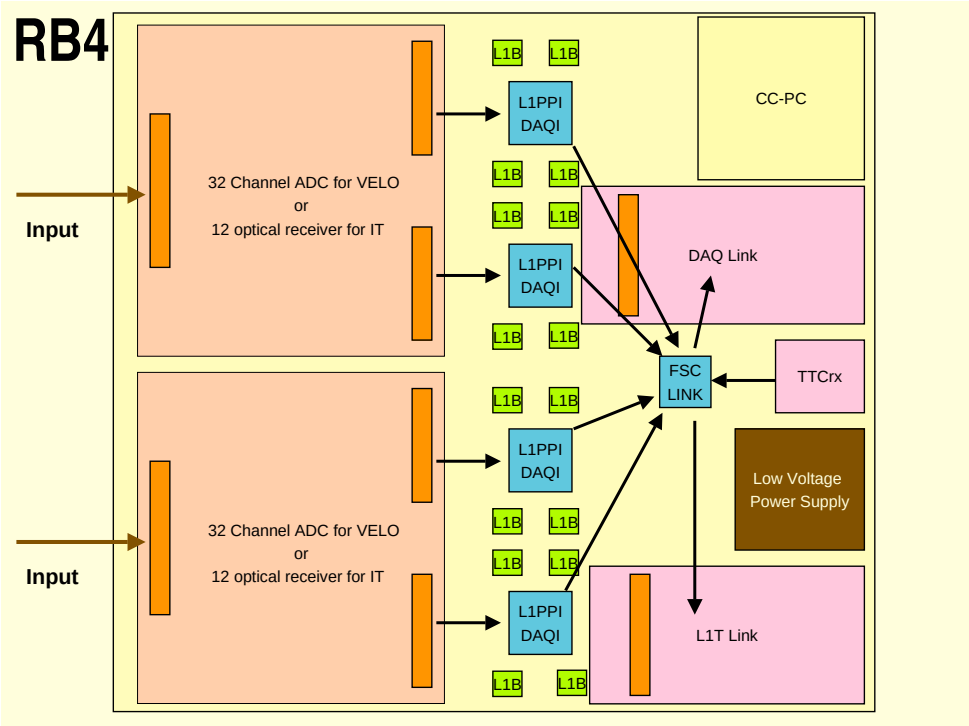

Figure 5.8: Layout of the Level-1 electronics board.

mother board that contains the standard functional parts of the LHCb Level-1 electronics, namely

- a sufficient amount of digital logic resources for data synchronisation and data processing for Level-1 trigger and data acquisition system,
- a Level-1 buffer and links to the trigger and data acquisition CPU farms and
- standard interfaces to the experiment control system (ECS) and the timing and fast-control system (TFC),

and accepts different input receiver cards for detector-specific data links. The receiver cards occupy approximately half the surface of the mother board, leaving sufficient space for the digital components.

For the Inner Tracker, the board will be equipped with two input data receiver cards, each of which receives data from twelve optical fibres, as described in Section 5.5. Each readout board, therefore, receives data from eight silicon ladders, 24 Beetle chips, or 3072 detector channels.

All digital logic will be implemented in FPGAs that will be configured according to the detector-specific application.

Synchronisation of the Level-0 and Level-1 electronics will be implemented in the same way as described in [63] for the VELO. From the point of view of data synchronisation, the optical link of the Inner Tracker and the electrical link foreseen for the VELO are equivalent, since both provide fixed data transmission latencies.

Algorithms for data preprocessing for the Level-1 trigger and for zero suppression for data acquisition will also be similar for Inner Tracker and VELO. They will be defined after further beam tests on final silicon sensors and readout chips.

The interface to the TFC system is provided by a TTCrx chip, the interface to the ECS by a Credit-Card PC (CC-PC). Both are LHCb standard solutions [43]. Integration into the TFC, ECS and data acquisition environment will be performed in close collaboration with

other LHCb groups.

5.7 Infrastructure

5.7.1 Cooling System

An efficient cooling of the detector boxes is mandatory in order to remove the heat dissipated by the front-end amplifiers and provide an adequate operating temperature for the silicon sensors. As was shown in Section 4.4, the ambient temperature inside the detector boxes should be kept below 5°C. The R&D program described in Section 3.4 has shown that at this temperature the cooling system has to remove a total heat load of approximately 75 W from each detector box. This corresponds to a total heat load of 900 W for the three stations T1-T3.

Liquid C_6F_{14} has been chosen as coolant for the Inner Tracker cooling system. The design considerations that have led to this choice are described in detail in [64]. C_6F_{14} is not flammable, non-irritating and practically non-toxic. Its compatibility with aluminium, plastics and elastomers has been demonstrated. Irradiation tests have been performed up to doses of 20 Mrad [65] and to neutron fluences of $3\times10^{13}\,\mathrm{cm}^{-2}$ [66]. C_6F_{14} is also the prefered choice for the cooling systems of the CMS silicon tracker and the Atlas TRT. Extensive experience with this coolant exists in the CERN cooling group, and support for the design of the final system will be available at CERN.

The layout of the cooling system is described in [64]. A schematics of the system is shown in Figure 5.9. It employs two cooling circuits, a primary circuit between the main chiller and a heat exchanger located in a cooling rack behind the shielding wall, and a secondary circuit that runs the liquid C_6F_{14} between the cooling rack and the detector boxes. The twelve detector boxes are operated in parallel mode. Inside the detector box, an aluminium cooling pipe with an outer diameter of 5 mm and a wall thickness of 0.25 mm will be employed. Calculations have shown that a volume flow of 150 l/h per detector box is adequate. At this flow, the temperature drop between detector box inlet and outlet will be less than 1°C and the pressure drop less than 1 bar.

Table 5.1: Design specifications for the cooling system.

total dissipated heat	900 W
total volume of C_6F_{14}	350 l
chiller power	5 kW
pump capacity	4 bar at 1800 l/h
temperature range	-40°C – 20°C
temperature accuracy	±0.1°C

Outside the detector box, insulated plastic hoses with an inner diameter of 10 mm will be used to transport the cooling liquid across the Outer Tracker. The flow in these pipes is also 150 l/h and a pressure drop of 0.5 bar is expected for 5 m long pipes.

The chiller will be located behind the LHCb shielding wall. Individual supply and return lines will be used for each Inner Tracker station. For a pipe diameter of 30 mm and a total mass flow of 600 l/h, a pressure drop of less than 0.5 bar will occur over the full length of the supply and return line. The total volume of the system is 350 l. The main design parameters and specifications of the system are summarised in Table 5.1.

A similar circuit will be used to flush detector boxes with a dry gas (N_2) in order to prevent condensation on the cold surfaces inside the box.

5.7.2 Power Distribution and Grounding Scheme

A schematics of the high-voltage and low-voltage distribution for an Inner Tracker detector box is shown in Figure 5.10. All power supplies will be located in the electronics barrack, at a distance of approximately 100 m from the detector boxes.

Low-voltage power supply and distribution for analog and digital power are kept separate throughout the system. One low voltage

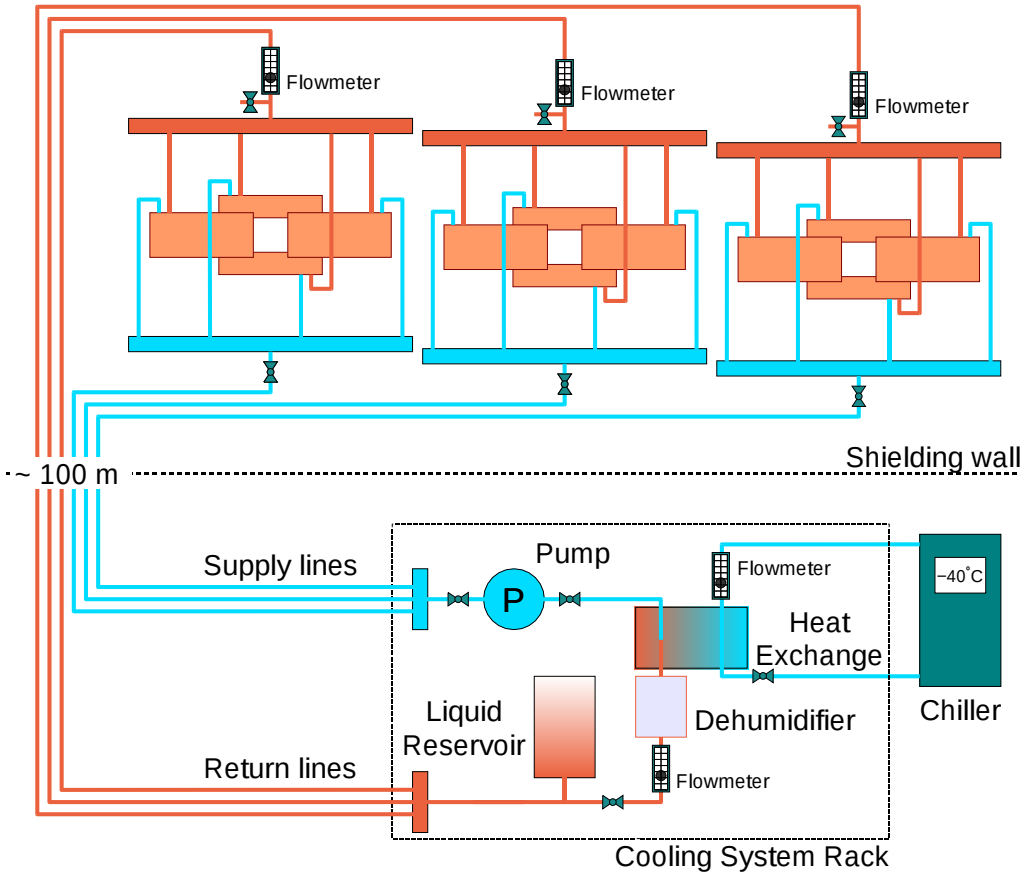

Figure 5.9: Schematic of the C_6F_{14} cooling system.

channel for analog and one low voltage channel for digital low voltage are foreseen for each detector box. More fine-grained power distribution takes place in the service box on the outer frames of the tracking station, where one programmable linear power regulator each is foreseen per ladder. This scheme permits to switch off individual detector ladders in case of their malfunctioning. Radiation qualified linear power regulators L4513 from ST Microelectronics will be employed.

The high-voltage system should provide bias voltages of up to 300 V and should be able to cope with leakage currents of up to approximately 4 mA per detector ladder. In the electronics barrack, one 15 mA high-voltage channel is foreseen per group of four ladders. This grouping will allow to adjust bias voltages according to the radiation received at different locations inside the detector box. The option is being studied to provide a ladder-by-ladder segmentation by solid-state (PhotoMOS) high-voltage switches in the service box. These would permit to switch off individual ladders in case of their malfunctioning. The susceptibility of these devices to Single Event Effects under irradiation has to be studied.

Investigations on the choice of cables, in particular for the part between the service box and the detector box where cables run over the sensitive surface of the Outer Tracker, are under way.

A sketch of the Inner Tracker grounding scheme is shown in Figure 5.11. The cooling plate is used to define the common ground for all silicon ladders in a detector box. All power supplies as well as the power distribution inside the service box are electrically floating. As described in section 3.4, the inside and the outside faces of the detector box enclosure are

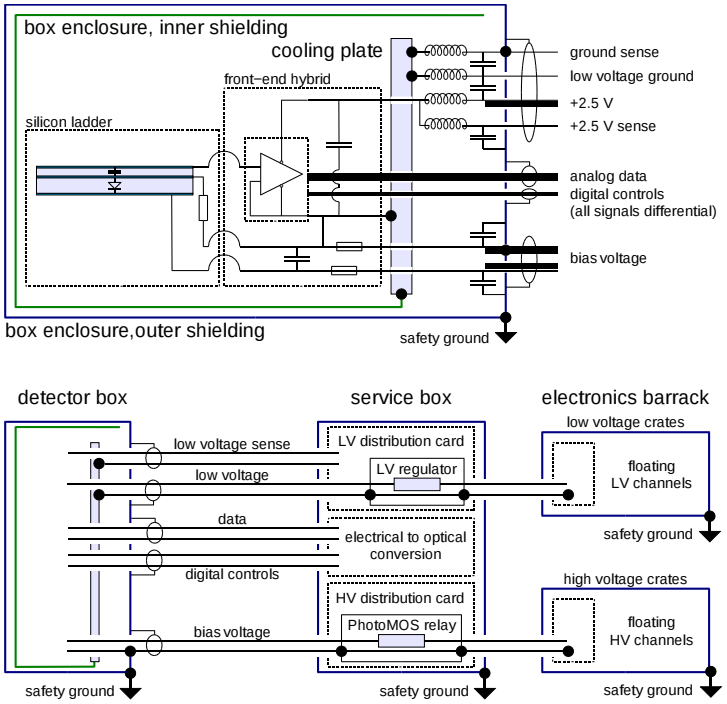

Figure 5.10: Schematics of high-voltage and low-voltage distribution.

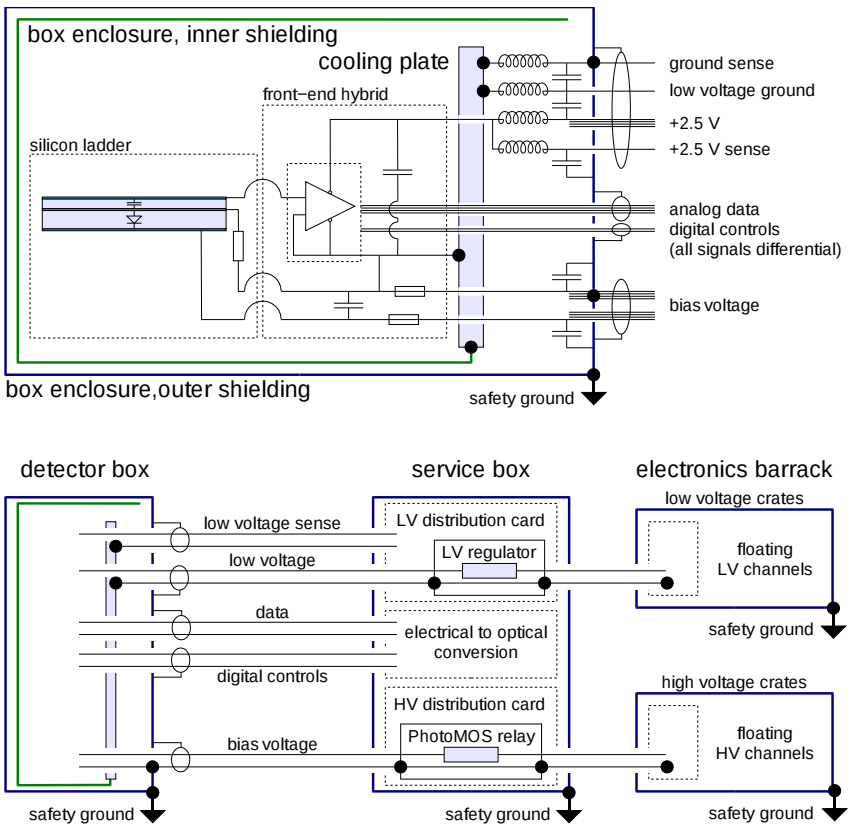

Figure 5.11: Grounding scheme.

each clad with a thin layer of aluminium. The inner layer is connected to detector ground, the outer layer is connected to safety ground. HV ground is connected to safety ground as required by safety regulations.

5.7.3 Alignment

A dedicated hardware alignment monitoring system is not foreseen for the Inner Tracker.

The design of the support frames will guarantee a positioning precision and reproducibility of better than 1 mm for the detector boxes, and an initial alignment will be provided by a survey after the installation of the detector boxes has been completed.

Precision alignment will be based on reconstructed tracks. The high particle rates in the region of the Inner Tracker allow to put stringent cuts on particle momenta in order to select samples of straight tracks in the low magnetic field region of stations T1-T3. Low-occupancy events can be selected in order to simplify pattern recognition.

The internal positioning precision of silicon sensors within a detector box is better than the spatial resolution of the detectors, such that for a first alignment step each detector box can be treated as one rigid unit. The task of aligning the Inner Tracker then consists in the determination of 72 alignment constants, three translations and three rotations for each of the twelve boxes. The relative alignment of detector boxes within a station can be determined using cross-over tracks.

In a second alignment step, the precise alignment of individual ladders within the detector box is determined using tracks that pass through the regions of overlap of neighbouring ladders within a detection layer. An additional handle for the relative alignment of individual ladders is provided by the different stereo views that lead to large regions of overlap between one ladder in one detection layer and two neighbouring ladders in a different detection layer.

Long-term variations of the alignment of the detector will also be monitored by the track reconstruction software.

5.7.4 Radiation Monitoring

The simulation studies described in Section 4.4 have shown that moderate radiation levels are expected in the area of the Inner Tracker. Detectors and front-end electronics will survive 10 years of LHCb operation at nominal luminosity even if reasonable safety factors are taken into account.

Nevertheless, the LHC presents a harsh radiation environment. An independent online monitoring of the actually received radiation dose is highly desirable in order to provide feedback to the machine, to protect equipment, and to adjust operating parameters in case observed radiation doses are higher than expected.

We plan to install in the region of the Inner Tracker stations a simple and robust radiation monitor system based upon metal-foil detectors. The system is described in detail in [67]. Similar detectors have been employed successfully for the steering of the multi-target wires in HERA-B and as beam profile monitors at a setup for radiation hardness studies at the Tandem Generator at Max Planck Institut für Kernphysik, Heidelberg. A prototype system was also operated successfully in an Inner Tracker test-beam at CERN.

The detector principle is simple: charged particles induce the emission of secondary electrons near the surface of a thin metal foil. Electron emission is further stimulated by two accelerating foils that are placed close to the detection foil and are kept at a relative voltage of typically 20-30 V. The resulting net charge loss is recorded by a charge integrator connected to the detection foil.

The layout of the detector is illustrated in Figure 5.12. It consists of five 25 μm thin aluminium foils that are mounted onto a lightweight support frame. The charge integrator is connected to the central foil. A possible implementation is shown in Figure 5.13. It consists of four detector ladders, each of which carries ten detection pads of 5 cm$\times$10 cm surface. A

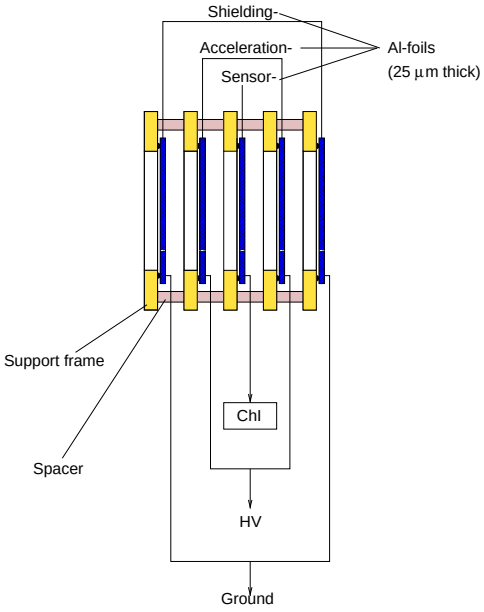

Figure 5.12: Sketch of radiation monitor.

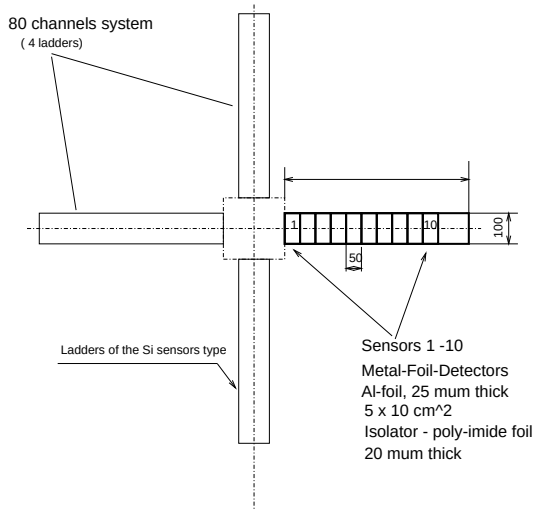

Figure 5.13: Sketch of radiation monitor.

more ambitious design that would cover the full surface of Inner Tracker boxes is described in [67].

The detector requires a minimum of infrastructure and a sensitivity down to particle rates of $5 \times 10^4\,\mathrm{s}^{-1}$ has been demonstrated in HERA-B. The overall radiation length of the detector, including support frames, is estimated at less than $0.2\%\,\mathrm{X}_0$.

5.8 Safety Aspects

In accordance with CERN's safety policy as described in the document SAPOC042, the Silicon Tracker project will follow the CERN safety codes which also allow the use of international construction codes for structural engineering as described in EUROCODE 3.

In the Initial Safety Discussion (ISD) with the CERN Technical Inspection and Safety Commission (TIS) the following risks and actions have been discussed:

1. The electrical circuits of the Inner Tracker will be subject to an electrical reception prior to operation (Code C1).

2. Electrical protection will be assured by the ECS/DSS that will be able to cut the power source when necessary.

3. Interventions on the circuits will require the primary power source to be switched off by means of the DSS.

4. Detector boxes will be cooled with C_6F_{14} and interlocks to the electronic equipment will be activated by over-temperature.

5. The cooling agent C_6F_{14} is a colourless, odourless, non-flammable and practically non-toxic liquid.

No risks other than electricity and material safety were identified during the Initial Safety Discussion.

Chapter 6

Project Organisation

This document describes the technical design of the Inner Tracker, which together with the TT stations forms the Silicon Tracker project. The following sections contain references to the TT station where appropriate and necessary to describe the size of the overall project.

6.1 Schedule

The project schedule is summarised in Table 6.1.

It is based upon the current LHC schedule that foresees first beams in April 2007, and covers the period from the submission of this document up to that date. It complies to the LHCb policy that all detector components should be installed and ready for common system commissioning at least 6 months prior to the first LHC operation.

6.1.1 Completion of Design and Prototyping

A realistic design of the Inner Tracker was described in Chapter 5. Some items, however, require further evaluation before the production can start. In particular, the following tasks will be addressed during the 12 months following the submission of this TDR:

- The characterisation of the Beetle 1.2 chip will be completed by the end of 2002. The chip will be tested on Inner Tracker silicon ladders in a cosmics setup starting in December 2002.
- The 5m analog part of the readout link, from the Beetle output to the FADC board will be designed and optimised. This work will start in December 2002 when Beetle 1.2 hybrids will be available.
- The radiation tolerance and SEU rate for the optical transmitters and for candidate FADC chips will be measured in spring 2003.
- The mechanical interface to the outer station frames will be designed. This work will be done in close collaboration with the Outer Tracker group and in consultation with the LHC vacuum group, which is designing the LHC vacuum pipe.
- The design of silicon ladders and detector box mechanics will continue to be scrutinised with a view to further optimisations of material budget.

An overview of the major R&D work specific to the TT station has been given in section 1.2.

6.1.2 Production

A detailed estimate of the time needed for production of the Inner Tracker has been made. It is based upon experience from previous large-scale silicon projects and takes into account acceptance tests of silicon sensors and assembly, testing and debugging of individual ladders and of complete detector boxes. It shows that the full set of Inner Tracker stations can be produced in one production site in 11 months.

Table 6.1: Project schedule.

The project schedule reserves 18 months for production.

The production of ladder supports will most probably be outsourced to industry. Contracts will be placed such that all components for all ladders will be available at the startup of ladder production.

Production, assembly and testing of front-end hybrids will run ahead of ladder production. Fully assembled and tested hybrids will be sent to the detector production site.

The construction of box mechanics is a relatively light task. It should follow the ladder production such that, after testing and debugging, ladders can be directly assembled into detector boxes.

Detector boxes will be completely assembled and tested at the production site, before being transported to CERN for installation.

6.1.3 Installation and Commissioning

The Inner Tracker stations are mounted onto a common support structure with the Outer Tracker and installation in IP8 has to be coordinated with the Outer Tracker group. The Inner Tracker detector boxes are compact objects and the actual installation will be very fast.

Each detector box constitutes a complete, standalone system. Readout electronics, high and low voltage systems and cooling will be available in time such that in-situ commissioning of individual detector boxes can start immediately upon their installation

The complete Inner Tracker system will be available for LHCb global commissioning in September 2006.

6.2 Milestones

Major milestones are summarised in Table 6.2.

Since the size of the TT sub-project is similar to that of the Inner Tracker, these milestones apply for the TT station as well as for the Inner Tracker.

6.3 Costs

Table 6.3 gives a detailed estimate of the costing for the Inner Tracker. The total cost amounts to 3.15 MCHF, including 15% spares on all components. The pricing of almost all items is based on preliminary quotes from industry or comparable recent purchases.

The cost of the TT station, as described in section 1.2, is estimated to be approximately 3 MCHF. The overall project cost of the Silicon Tracker will thus be of the order of 6.15 MCHF.

6.4 Division of Responsibilities

The following institutes are currently working on the Silicon Tracker project: Max Planck-Institut für Kernphysik Heidelberg, Institute for Nuclear Research of the National Academy of Science of Ukraine Kiev, IPHE Université de Lausanne, Budker Institute for Nuclear Physics Novosibirsk, Universidade de Santiago de Compostela, and Physik-Institut der Universität Zürich.

The sharing of responsibilities for the main project tasks is listed in Table 6.4. Specific software developments for data acquisition, controls and monitoring, as well as the interfaces to the experiment control system (ECS) are understood to be included under the respective tasks. The groups als participate in the development of track reconstruction software, within the framework of the LHCb Tracking Task Force.

Table 6.2: Milestones.

Milestone	Date
Project	
Final decision on production site(s)	06/2003
Engineering design finished	12/2003
First detector box in IP8, start of system commissioning	11/2005
Full system ready for integration into LHCb	09/2006
Silicon sensors	
Final order placed	03/2004
10% sensors delivered	09/2004
50% sensors delivered	01/2005
All sensors delivered	07/2005
L0 electronics	
BEETLE engineering run	03/2004
10% of hybrids assembled and tested	08/2004
BEETLE production run	12/2004
Readout link and service box	
Full prototype test of readout link	06/2003
L1 electronics	
Production of L1E boards started	03/2004
10% of L1E boards produced and tested	08/2004
50% of L1E boards produced and tested	04/2005
All L1E boards produced and tested	02/2006
Mechanics	
10% of ladder supports delivered	08/2004
Mechanics for first detector box ready	08/2004
Assembly	
Production sites ready	06/2004
Ladder assembly starts	09/2004
10% of ladders and first detector box assembled	01/2005
50% of ladders assembled	07/2005
All ladders and detector boxes assembled and tested	02/2006

Table 6.3: Inner Tracker costs, including 15% spares.

Item	Number of units	Cost (kCHF)
Silicon sensors	580	870
L0 electronics		320
Front-end chips	1160	
Hybrids	390	
Pitch adaptors	390	
Readout links	4640	560
L1 electronics		760
L1E boards	48	
Readout units	10	
Crates	6	
Mechanics		290
Ladder supports	390	
Balconies	390	
Cooling plate	12	
Insulation box	12	
Outer Tracker interfaces	6	
Infrastructure		350
High voltage		
Low voltage		
Cooling system		
Total		3150

Table 6.4: Sharing of responsibilities

Task	Institute(s)
Silicon sensors	Zürich
L0 electronics	MPI Heidelberg
BEETLE chip, hybrid	
Readout link	Zürich
digitisation, optical links	
L1 electronics	Lausanne
DAQ interface, L1 trigger interface	
Mechanics	
ladder supports	Lausanne
station mechanics	Zürich
Infrastructure	
HV, LV, monitoring	Santiago
radiation monitor	Kiev
Assembly sites	
TT production	Kiev, Zürich
T1-T3 production	Lausanne, Santiago
Installation and commissioning	all

Bibliography

[1] *LHCb technical proposal*, CERN/LHCC 98-4

[2] *LHCb Outer Tracker Technical Design Report*, CERN/LHCC 2001-024

[3] W. Hulsbergen, *Status of the HERA-B experiment*, Proc. Cracow Epiphany conference, Cracow, Poland, 2001

[4] J. P. Perroud and F. Ronga, *PSI run report of the Micromegas detector, March 28 – April 13 1999*, LHCb note 99-020

[5] B. Adeva et al., *Performance of Micro Wire Detector at a PSI test-beam*, LHCb note 99-021

[6] M. Ziegler et al., *A triple GEM detector with two-dimensional readout* LHCb note 2000-056

[7] O. Steinkamp, *A possible layout of an Inner Tracker silicon detector*, LHCb note 2000-109

[8] O.Steinkamp, *Layout of a Cross-Shaped Inner Tracker*, LHCb note 2001-114

[9] *LHCb RICH Technical Design Report*, CERN/LHCC 2000-037

[10] M. Benayoun et al., *Tracking, tracker layout and RICH performance*, LHCb note 2001-100

[11] H. Dijkstra et al., *The use of the TT1 tracking station in the level-1 trigger*, LHCb note 2002-045

[12] O. Steinkamp, *Layout and R&D for an all-silicon TT station* , LHCb note 2002-056

[13] N. v. Bakel et al., *The Beetle reference manual*, LHCb note 2001-046

[14] *LHCb Vertex Locator Technical Design Report*, CERN/LHCC 2001-011

[15] P. Koppenburg, *Effect of Pulse Overspill on the Level-1 Trigger*, LHCb note 2001-078

[16] P. Moreira et al., *A radiation tolerant gigabit serializer for LHC data transmission*, 7th Workshop on Electronics for LHC Experiments, CERN-LHCC 2001-034

[17] E. Barberis et al., IEEE Trans. Nucl. Sci. **41** (1994) 785

[18] S. Braibant et al., Nucl. Instr. and Meth. **A485** (2002) 343

[19] F. Lehner et al., *Description and characterization of Inner Tracker silicon prototype sensors*, LHCb note 2001-036

[20] C. Bauer et al., *Characterization of Inner Tracker silicon prototype sensors using a* ^{106}*Ru-source and a 1083 nm laser system*, LHCb note 2001-121

[21] M. Feuerstack et al., *Helix128 - an amplifier and readout chip for MSGCs and silicon microstrip detectors*, HD-ASIC-18-0696
W. Fallot-Burkhardt et al., *Helix - a readout chip for the HERA-B microstrip detectors*, 2nd Workshop on Electronics for LHC Experiments, Balatonfured, Hungary, 1996

[22] F. Lehner et al., *Description and evaluation of multi-geometry silicon proto-*

type sensors for the LHCb Inner Tracker, LHCb note 2002-038

[23] R. Brenner et al., Nucl. Instr. and Meth. **A339** (1994) 564

[24] U. Trunk et al., *Enhanced radiation hardness and faster front ends for the Beetle readout chip*, 7th Workshop on Electronics for LHC Experiments, Stockholm, Sweden, 2001

[25] S. Löchner et al., *Performance of the Beetle readout chip for LHCb*, 8th Workshop on Electronics for LHC Experiments, Colmar, France, 2002

[26] C. Bauer, *A prototype hybrid for Beetle 1.1*, LHCb note 2002-057

[27] C. Bauer et al., Nucl. Instr. and Meth. **A418** (1998) 65

[28] C. Bauer et al., *Test beam results on Inner Tracker silicon prototype sensors*, LHCb note 2001-135

[29] M. Agari et al., *Testbeam results on multi-geometry prototype sensors for the LHCb Inner Tracker*, LHCb note 2002-058

[30] H. Esbensen et al., Phys. Rev. **B18** (1978) 1039

[31] S. Hancock et al., Phys. Rev. **A28** (1983) 615

[32] F. Lehner et al., *Design, construction and thermal measurements on a detector box for the Inner Tracker of the LHCb experiment*, LHCb note 2002-059

[33] S. P. Sukhatme, *Heat Transfer*, Sangam Books Ltd., London

[34] R. J. Frei et al., *Thermal and mechanical studies of U-shaped carbon fibre support for the LHCb Inner Tracker detector's ladder*, LHCb note 2002-060

[35] K. Bösiger et al., *The LHCb Inner Tracker cooling balcony and plate: design and material selection studies*, LHCb note 2002-061

[36] J. Klett et al., *High-thermal-conductivity, mesophase-pitch derived graphitic foams*, Composites in Manufacturing, Vol.**14** no.4, 1999

[37] *Review of particle physics*, Europ. Phys. Journ. **C15**, 2000

[38] A. Vollhardt, *The LHCb Inner Tracker data readout system*, LHCb note 2002-062

[39] Y. Ermoline, *Vertex detector electronics: ODE pre-prototype*, LHCb note 2001-057

[40] A. Bay et al., *Tests on the L1-electronics board prototype RB2*, LHCb note 2002-033

[41] A. Bay et al., *LHCb VELO off detector electronics, preprocessor and interface to the Level-1 trigger*, LHCb note 2001-043

[42] A. Bay et al., *Vertex detector electronics: RB3 specification*, LHCb note 2001-050

[43] *LHCb Online System Technical Design Report*, CERN/LHCC 2001-040

[44] T. Sjöstrand, Comp. Phys. Comm. **82** (1994) 74

[45] P. Bartalini et al., *Tuning of multiple interactions generated by PYTHIA*, LHCb note 1999-028

[46] http://www.lns.cornell.edu/public/CLEO/soft/QQ

[47] *GEANT Detector Description and Simulation Tool*, CERN Program Library Long Writeup W5013 (1994)

[48] R. Hierk, M. Merk and M. Needham, *Outer Tracker occupancies and detector optimisation*, LHCB note 2001-093

[49] R. van der Eijk et al., *Performance of the LHCb OO track fitting software*, LHCb note 2000-086

[50] A. Fasso et al., *FLUKA: Status and prospective for hadronic applications*, Proc. Monte Carlo 2000 conference, Lisbon, Portugal, 2000

[51] A. Polouektov et al., *First results from LHCb Inner Tracker performance studies using new digitization software*, LHCb note 2001-118

[52] M. Needham, *Inner and outer tracker occupancy studies in the light LHCb detector*, LHCb note 2002-032

[53] M. Needham, *Momentum resolution studies for the Inner Tracker TDR*, LHCb note 2002-043

[54] L. Shekhtman, *Radiation background at the region of Inner Tracker stations*, LHCb note 2002-063

[55] A. Vasilescu and G. Lindstroem, *Displacement damage in silicon, online compilation* http://sesam.desy.de/ gunnar/Sidfuncs.html

[56] H. Spieler, IEEE Trans. Nucl. Sci. **NS-32** (1985) 419

[57] F. Lehner and O. Steinkamp, *Alignment tolerances for the Inner Tracker*, LHCb note 2002-064

[58] B. Carron et al., *Assembly procedure for the silicon Inner Tracker*, LHCb note 2002-065

[59] P. Allport et al., Nucl. Inst. and Meth. **A466** (2001) 376

[60] *The I^2C bus and how to use it*, Philips Semiconductors 1995

[61] P. Denes et al., Nucl. Inst. and Meth. **A417** (1998) 371

[62] A. Bay et al., *Common Level-1 board*, LHCb note 2002-052

[63] Y. Ermoline, Nucl. Instr. and Meth. **A461** (2001) 456

[64] F. Lehner and M. Stodulski, *The liquid cooling system of the LHCb Inner Tracker: design constraints and considerations* , LHCb note 2002-066

[65] M. Atae et al., *Radiation hardness studies of cooling fluids, epoxies and capacitors for CMS pixel system*

[66] V. Vacek et al., *Perfluorcarbons and their use in cooling systems for semiconductor particle detectors*

[67] V. Pugatch et al., *Radiation monitoring system for the LHCb Inner Tracker*, LHCb note 2002-067